TITANIUM DIOXIDE-BASED CARBON MONOXIDE GAS SENSORS: EFFECTS OF CRYSTALLINITY AND CHEMISTRY ON SENSITIVITY

By

ZACHARY MARK SEELEY

A dissertation submitted in partial fulfillment of
the requirements for the degree of

DOCTOR OF PHILOSOPHY

WASHINGTON STATE UNIVERSITY
Materials Science Program

DECEMBER 2009

To the Faculty of Washington State University:

The members of the Committee appointed to examine the dissertation of ZACHARY MARK SEELEY find it satisfactory and recommend that it be accepted.

_____

Susmita Bose, Ph.D., Chair

_____

Amit Bandyopadhyay, Ph.D.

_____

Jeanne L. McHale, Ph.D.

ACKNOWLEDGMENT

Financial support for this project was provided by the National Science Foundation and the Office of Naval Research.

I wish to foremost acknowledge my parents Mark and Eileen Seeley and my brothers Matt and Lane. 25+ years of schooling doesn't compare to what I have learned from you guys.

I would like to further acknowledge my advisor Dr. Susmita Bose as she continually expected me to achieve my best. I would also like to thank the other committee members Dr. Amit Bandyopadhyay and Dr. Jeanne McHale for productive conversation and suggestions.

I would like to express thanks to Robert Lentz for helping establish that data acquisition program, and the U of Idaho glass shop for preparing my complicated sample holder. Young-Jin Choi got the balls rolling on this sensor project saving me from having to start from scratch. Hongsoo Choi and Sheldon Bernard were a big help teaching me the sol-gel spin-coating methods. Mangal Roy and Subhadip Bodhak performed many hours on the brain torturing FE-SEM. Candy Mercado was very kind in providing UV-VIS and photoluminescence data and analysis. Dr. Vamsi and Dr. Shash were a big help in many ways (mostly signing paychecks) throughout the process. Felix Espana helped out through two bike builds, nerves prior to races, and countless journeys to Pizza Perfection.

Finally, and most deserving of my gratitude, my wifey Carole-Anne has enhanced my life immeasurably over the last 5 years. We can now enjoy a new chapter in our lives as we start a family together. Ashlyn, this work is dedicated to you.

TITANIUM DIOXIDE-BASED CARBON MONOXIDE GAS SENSORS: EFFECTS OF CRYSTALLINITY AND CHEMISTRY ON SENSITIVITY

Abstract

by Zachary Mark Seeley, Ph.D.
Washington State University
December 2009

Chair: Susmita Bose

Among metal-oxide gas sensors which change electrical resistive properties upon exposure to target gasses, titanium dioxide (TiO_2) has received attention for its sensitivity and stability during high temperature (>500°C) operation. However, due to the sensing mechanism sensitivity, selectivity, and stability remain as critical deficiencies to be resolved before these sensors reach commercial use. In this study, TiO_2 thick films of approximately 30µm and thin films of approximately 1µm thick were fabricated to asses the influence of their material properties on gas sensing mechanism. Increased calcination temperature of TiO_2 thick films led to grain growth, reduction in specific surface area, and particle-particle necking. These properties are known to degrade sensitivity; however the measured carbon monoxide (CO) gas response improved with increasing calcination temperature up to 800°C. It was concluded that the sensing improvement was due to increased crystallinity within the films. Sensing properties of TiO_2 thin films of were also dependent on crystallization, however; due to the smaller volume of material, they reached optimized crystallization at lower temperatures of 650°C, compared to 800°C for thick films.

Incorporation of tungsten (W) and nickel (Ni) ions into the films created donor and acceptor defect sites, respectively, within the electronic band gap of TiO_2. The additional n-type

defects in W-doped TiO_2 improved n-type CO response, while p-type defects in Ni-doped TiO_2 converted the gas response to p-type. Chemistry of thin films had a more significant impact on the electrical properties and gas response than did microstructure or crystallinity. Doped films could be calcined at higher temperatures and yet remain highly sensitive to CO.

Thin films with p-n bi-layer structure were fabricated to determine the influence of a p-n junction on gas sensing properties. No effect of the junction was observed and the sensing response neared the average of the layers; however, electrical and gas response studies revealed that the majority of the conductivity and gas-surface reactions took place on the outer layer of the film. Further research is necessary to understand the influence of p-n junctions on the gas sensing behavior.

TABLE OF CONTENTS

Page

LIST OF TABLES

LIST OF FIGURES

Dedication

This dissertation is dedicated to my Ashlyn Grace

CHAPTER ONE

INTRODUCTION

1.1 Need for Harsh Environment Gas Sensors

Our world is changing (things are heating up). Never before has man-made climate change been recognized internationally as such a high priority. Over the past century, the average global temperature has risen by 0.8°C and, with current trends, an additional increase of up to 4°C is predicted over the next hundred years. This type of temperature change could potentially lead to disastrous conditions such as a 35m increase in sea level and elimination of 60% of the planet's species [Hansen '06]. Drastic measures are needed just to slow, much less reverse, this exponential trend.

The cause of global warming is commonly known as the greenhouse effect. Greenhouse gasses (GHGs) caught in the atmosphere absorb and re-emit some of earth's infrared black body radiation, trapping heat between the surface and troposphere. While this process is critical for life on our planet, it remains in a delicate equilibrium. Slight man-made increase in GHGs will increase the earth's temperature, which will in turn decrease the reflective ice sheet area and cause a further increase in GHG emission. This positive feedback loop is responsible for the exponential increase in global temperature which is threatening our planet [Rahmstrof '07, Hansen '05].

The most prominent GHGs are water vapor, carbon dioxide (CO_2), methane (CH_4), nitrogen oxides (NO_x), ozone (O_3), and fluorinated carbon gasses. In 2005, the United Nations Framework Convention on Climate Change established the Koyoto Protocol, which outlined these gasses as the prime concern with regards to global warming and established a goal to

reduce GHG emissions to sustainable concentrations. Of these critical gasses, CO_2 is the largest contributor to global warming, as shown in Figure 1.1. Fossil fuel combustion and industrial processes are the leading sources of CO_2 pollutants [Raupach '07]. Therefore, the largest contributor to global warming is the CO_2 exhaust from combustion engines and industrial processes. These two sources are currently the most heavily targeted by the United States government to reduce emissions to pre-1990 levels by the year 2020 as part of the Clean Air Act.

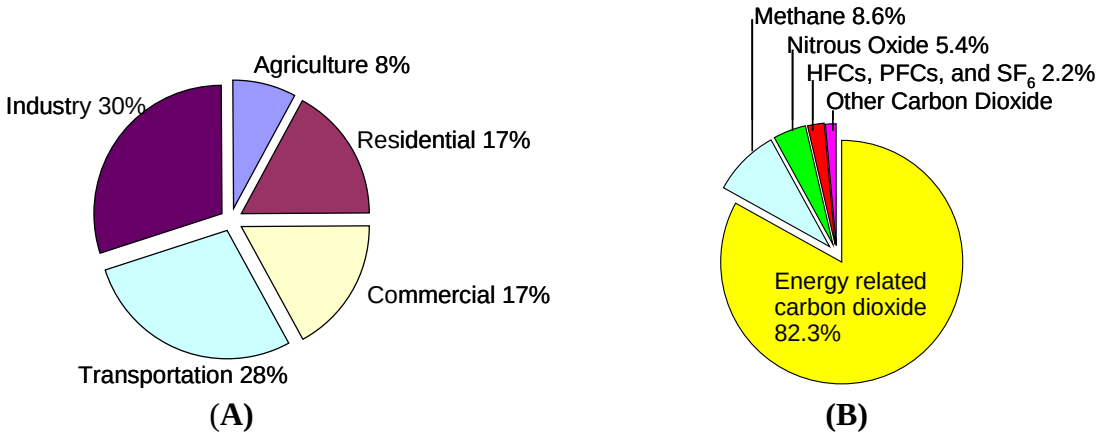

Figure 1.1. (A) Greenhouse gas emissions by sector, source: US EPA Inventory of Greenhouse Gas Emissions and Sinks, 2006, and (B) Greenhouse gas emissions by gas, source: Energy Information Administration, *Emissions of Greenhouse Gasses in the United States 2006* (Washington, DC. Nov 2007).

One step toward reducing GHG emissions from the exhausts of combustion engines and industrial processes is gas detection and monitoring, which can enable more efficient reactions and result in lower pollution. Monitoring the exhaust compositions enables feedback control systems for chemical processes, automatic operation of gas related facilities, alarming systems, and adjustments to be made in the process which promote higher efficiencies [Yamazoe '05]. To maximize process efficiency, real time composition measurements are needed, which require sensors able to operate near the reaction site directly in the exhaust flow. This environment typically consists of high temperatures and the potential to contain harsh and corrosive gasses. Development of sensors which can operate stably for extended periods of time under these

circumstances presents a significant challenge. Furthermore, maintaining high sensitivity and selectivity to trace amounts of target gas is difficult when the sensor is operated under these conditions. Various applications such as petrochemical, oil, steelmaking, power generation, refineries, paper, and glass industries [Akbar '06], including the aerospace industry [Hunter '02], can benefit from the development of high operating temperature, harsh environment gas sensors.

1.2 Available Gas Sensors and Applications

There are several main categories of available gas sensors including electrochemical, infrared, solid electrolyte, and semiconductor. Electrochemical sensors work by oxidizing or reducing a target gas on a catalytic electrode and measuring the resulting current. These sensors are sensitive to low concentrations; however, they are mostly limited to electrochemically active target gasses and can sometimes show a lack of selectivity. Infrared sensors work by passing a beam of infrared radiation through a gas sample and detecting which wavelengths are adsorbed by the sample. Adsorption bands are then matched with known gasses. These sensors can provide very detailed information on the composition of a mixed gas environment; however, the setup is rather complex and costly compared to other types of sensors. These two types of sensors, electrochemical and infrared, are very useful for determining detailed information about a gas mixture but one major limitation they have is operation temperature; they are limited to detecting gasses near room temperature. Therefore, any gas which is at an elevated temperature must be cooled before it can be analyzed, causing a significant delay from real time measurements.

Solid electrolyte and semiconductor sensors are among the few sensors which are operable at high temperatures. Solid electrolyte sensors work by conducting ions through a solid

ceramic material such as yttria stabilized zirconia (YSZ). A voltage is generated across the sensor based on concentration differences between the sample and reference gases. These sensors are very stable at high temperatures, but are limited to a few specific chemical species and can be poisoned by the presence of humidity or other gasses. Lastly, metal-oxide semiconductor (MOS) gas sensors work through surface reactions with target gases (described in more detail in the next section). This reaction changes the electronic properties in the semiconductor, and the target species is detected by a change in current, resistance, or voltage of the sensor. Depending on the sensor material and target gas, MOS sensors can be very stable at high operating temperatures and can be optimized for many target gasses; however, as only one signal is produced by the sensor, selectivity in a mixed gas environment remains a major obstacle.

Each category of gas sensor has specific advantages and disadvantages, allowing use only in specific applications. This work focuses on MOS sensors in particular, which have the advantages of cheap and simple fabrication, fast response time, stability in almost any environment containing harsh or corrosive gasses, and most importantly the ability to be operated at elevated temperatures. These advantages make MOS sensors most applicable in measuring the composition of a high temperature exhaust gas flow in-situ where they can give real time feedback. However, increasingly strict regulations on exhaust pollution put forth by the Environmental Protection Agency (EPA) is continuously requiring improvements to be made in the sensors' sensitivity and selectivity. Improved scientific understanding of the sensing mechanism is needed to design sensors which can meet these demands.

1.3 Metal-oxide Semiconductor Gas Sensors

Metal-oxide semiconductor (MOS) gas sensors, sometimes called 'chemoresistors,' were originally developed in 1962 by Taguchi and Seiyama using zinc oxide (ZnO) as their example MOS material [Taguchi '62, Seiyama '62]. Although the gaseous interaction with an oxide was already known to alter the electronic properties of the semiconductor, they discovered that at high temperatures (~450°C) the adsorption and desorption reactions took place very rapidly and applied this phenomenon toward the application of gas detection.

Many transition metal oxides, such as tin dioxide (SnO_2), titanium dioxide (TiO_2), tungsten oxide (WO_3), indium oxide (In_2O_3), nickel oxide (NiO), copper oxide (CuO), and others, have been found to show electronic property changes similar to the findings of the ZnO Taguchi sensor when exposed to various gas environments [Meixner '96, Bogdanov '99, Banno '95]. These transition metal oxides posses the advantageous ability to form oxygen vacancies in the lattice, which contribute to the electronic semiconducting properties of the material. TiO_2, for instance, is known to exist in the non-stoichiometric form TiO_{2-X}. In the temperature range below 1000° and "near-atmospheric" oxygen pressures, it has been found that oxygen vacancies are the predominant defect [Kofstad '72]. The oxygen vacancies result in an extra negative charge on the titanium atoms (Ti′) as described by Equation 1.

$$2TiO_2 \rightarrow 2Ti' + 3O_o^{x} + Vo^{\cdot\cdot} + \tfrac{1}{2}O_2\,(g) \qquad (1)$$

Because titanium is a multivalent ion, it is somewhat stable accepting this negative charge and remaining as a Ti^{3+} donor state. However, depending on the thermal activation energy available, some of these donor Ti′ ions will convert back to the stable Ti^{4+} state by ionizing an electron (e′) into the conduction band as described by Equation. 2, resulting in the common n-type conductivity of TiO_2.

$$Ti' \rightarrow Ti + e' \quad (2)$$

As the oxygen concentration in the surrounding atmosphere changes, oxygen ions will diffuse into or out of the oxide, effectively reducing or increasing, respectively, the oxygen vacancy concentration, and therefore the conductivity, in the material. This analysis describes bulk conductivity only, and has been used to describe the conductivity (σ) as a function of oxygen partial pressure (Po_2) simplified to Equation 3.

$$\sigma = 2^{½} q \mu_n [Po_2]^{-1/6} \exp[(E_a)/kT] \quad (3)$$

where (q) is the electronic carriers charge, (μ_n) is their mobility, and (E_a) is the activation energy required to ionize the loosely bound electron from the Ti^{3+} donor state into the conduction band [Mandelis '93]. This discovery has lead to the use of TiO_2 and other metal oxides in the application of bulk oxygen sensors in the automotive industry [Moos '05].

Bulk conductivity sensors can provide useful information on the oxygen content; however, this mechanism relies on the relatively slow time- and temperature-dependent diffusion of oxygen ions through the bulk material. More recently, new surface sensitive gas sensing mechanisms have been proposed, which offer much faster kinetics and potentially allows the detection of numerous gas species. These sensing mechanisms involve the target gas species directly interacting with the surface of the metal-oxide. Negatively charged oxygen vacancies near the surface of the metal oxide have been shown to behave as adsorption sites for gas species [Menetrey '03]. During the adsorption reaction, the negative charge transfers from the vacancy to the adsorbate, effectively trapping the electron associated with the vacancy and not allowing it to take part in electronic conduction. Most environments of interest contain oxygen, and therefore the adsorption of oxygen onto the surfaces of these MOS sensors has been studied in detail. It has been found that the type of oxygen adsorbed on the surface is dependent on the

operating temperature [Park '03]. At temperatures below approximately 200°C, it appears to be molecular oxygen that adsorbs as O_2^-. Above this temperature there is enough thermal energy to decompose the oxygen molecule on the surface and a more stable O^- adsorbate exists. At even higher temperatures above approximately 450°C, enough energy becomes available to ionize and trap a second electron from the oxygen vacancy producing O^{2-} ions present on the MOS surface.

The presence of these adsorbed species on the surface of the MOS has been used to explain a surface-sensitive mechanism by which environmental gas compositions change the electrical resistance of the MOS sensor. The adsorbed species trap electrons in the adsorption bond and do not allow them to participate in the material's electronic conduction. This leads to the formation of a depletion layer on the MOS surface, which has low conductivity compared with the bulk. For conduction to take place through the material, electrons need to pass from one particle to the next, which means it will necessarily need to pass through the depletion layer on the particle's surface. Therefore the size of the depletion layer will act as a conduction barrier and control the material's conductivity. Introduction of strong reducing (e.g. CO) or oxidizing (e.g. nitrogen dioxide) gasses into the environment will decrease or increase, respectively, the number of adsorbed oxygen species on the surface of the MOS, changing the depletion layer width [Stetter '78]. CO, for instance, reacts with the adsorbed oxygen to form CO_2, releasing the trapped electron back into the MOS as described in Figure 1.2A. These gasses are measured by a change in the materials resistance, as seen in Figure 1.2B.

This is an elegant method for detecting gasses at elevated temperatures; however selectivity becomes a challenge when there are many different oxidizing and/or reducing gasses present in a mixed gas environment and only one signal (resistance) is measured. From this mechanism it has been found that the sensitivity and selectivity of a specific MOS toward a

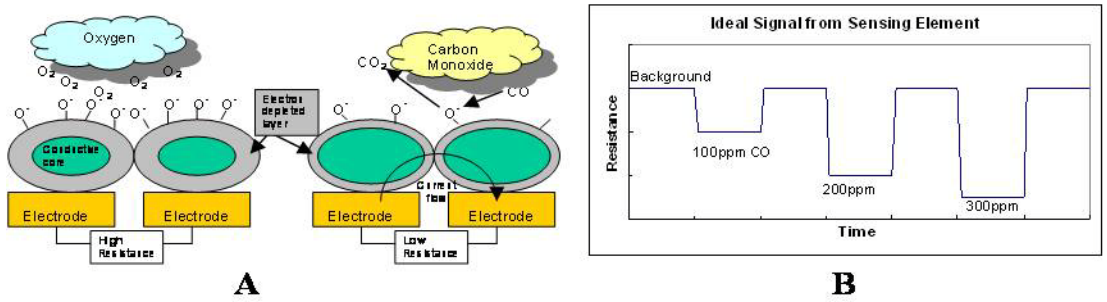

Figure 1.2. (A) Schematic of the gas sensing response mechanism for an n-type metal-oxide. High resistance in presence of oxygen and low resistance in presence of reducing gas. (B) Ideal resistance signal from a sensing test with change in gas environment concentration. Figure redrawn from: Sheikh A Akbar and Prabir K. Dutta, "Ceramic Sensors for Industrial Applications," NSF Center for Industrial Sensors and Measurements (CISM).

specific target gas will be influenced by the operating temperature [Sahm '06], reducing or oxidizing potential of the target gas [Huusko '93], type of oxygen ions adsorbed on the surface and strength of the adsorption bond [Park '03], availability of electrons near the surface of the MOS [Yamazoe '79], surface area exposed to the gas environment [Rothschild '04], microstructure and electrical properties of the MOS [Yamazoe '91], and design of the sensing element [Korotcenkov '07]. Therefore many parameters must be closely studied and optimized before an MOS sensor with high sensitivity, selectivity, and stability can be obtained.

Currently, commercially available MOS sensors are in the form of bulk or thick film ceramic materials, which offer advantages of low manufacturing cost, long lifetime, and reasonable gas sensitivity [Akbar '06]. Recently, the improvement of microelectromechanical system (MEMS) fabrication techniques has expanded the knowledge of thin film deposition and characterization. Thin film gas sensors have shown large increases in response over that of their thick film counterparts [Zakrzewska '04]. This has enabled sensitivities to increase and detection limits to be as low as parts per billion or less [Comini '00]. Thin films also enable a smaller sized sensor to be fabricated, which can operate on less power consumption and in small sensor arrays.

Thin films, however, are inherently less stable at high temperatures, resulting in the need for improved material properties in thin film sensing applications [Akbar '06].

1.4 Introduction to TiO_2 as a Gas Sensor

Crude titanium dioxide (TiO_2) ore is naturally found in abundance and mined for various applications. One of TiO_2's most valuable properties is its unusually high refractive index of nearly 2.7. This property makes TiO_2 a valuable white pigment because it efficiently reflects light. Approximately 4 million tons of TiO_2 white pigment are consumed annually worldwide for uses in many everyday products such as paint, makeup, coatings, plastics, paper, ink, food, medicine pills, toothpaste, and sunscreen. Apart from traditional uses, TiO_2 has been found to possess useful properties, which makes it useful in several advanced applications as a photocatalyst to clean waste water, in dye sensitized solar cells, as a bioactive implant, and as a gas sensor.

TiO_2 exists as eleven different crystallographic modifications; however, the two most commonly studied are anatase and rutile, which are both tetragonal in structure. The basic unit cell structures of these two phases and relevant data are shown in Figure 1.3 and Table 1.1. Anatase is metastable, which irreversibly converts to the more stable rutile upon heating. In the structure, each titanium atom is coordinated to six oxygen atoms and each oxygen atom is coordinated to three titanium atoms. The structure can be visualized to be made up of slightly distorted TiO_6 octahedra, each sharing oxygen atoms at corners and along edges so that each oxygen is shared by three octahedra.

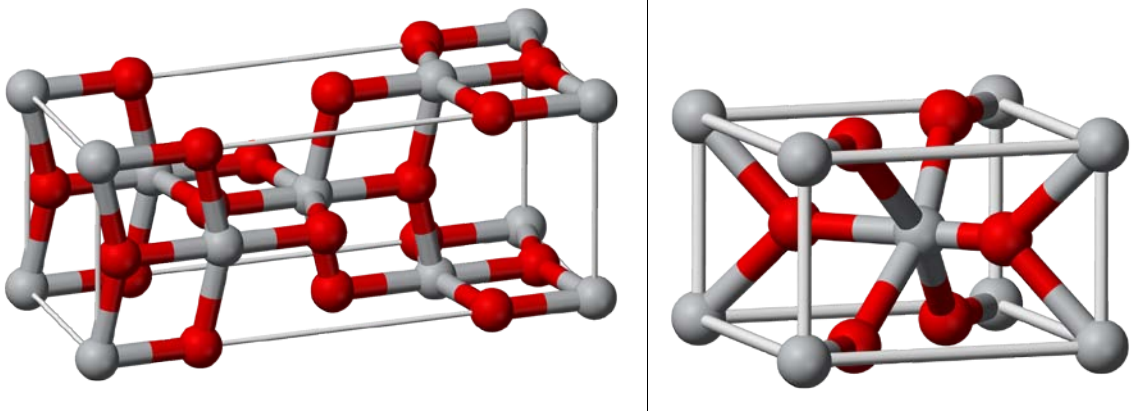

(A) (B)

Figure 1.3. Unit cell of TiO_2 anatase (A) and rutile (B). Grey balls = Ti atoms and red balls = O atoms. Source: wikipedia.

It has been shown that the anatase-to-rutile phase transformation is often accompanied by significant grain and particle growth due to higher atomic mobilities and bond breakage [Ruiz '04, Hu '03, Ding '98]. Anatase also has a larger indirect band gap of Eg = 3.2eV, compared to the direct band gap for rutile (Eg = 3.0eV). These changes in size and structure lead to significant differences in the electronic properties of the two phases [Knauth '99, Savage '01]. Due to the nature of the band gaps, anatase consistently shows n-type conduction while rutile sometimes shows p-type conduction. It has been hypothesized that common trivalent metal ion impurities in TiO_2 result in the formation of titanium interstitials in the lattice, which are then oxidized during the anatase-to-rutile phase transformation, leading to the observed p-type conduction [Savage '01]. For these reasons, anatase is considered more reactive than rutile, and is the desired phase for applications in catalysts and sensors [Hitchman '02, Sclafani '90].

Table 1.1. TiO_2 crystal structure data [Mo '95].

Phase	Anatase	Rutile
Crystal structure	Tetragonal	Tetragonal
Lattice constants (Å)	a = 3.784, c = 9.515	a = 4.585, c = 2.953
Density (g/cm^3)	3.895	4.274
Ti – O bond length (Å)	1.937 1.965	1.949 1.980
Band Gap (eV)	3.2 (indirect)	3.0 (Direct)

MOS gas sensors, such as tin dioxide (SnO_2), have received much attention for their stable operation at elevated temperatures. SnO_2 in particular is currently being used commercially to sense gasses from automobile exhaust during emissions testing, which takes place between 200-400°C [Gopel '95]. Above this temperature range, sensitivity drops off quickly and the material's microstructure becomes unstable. More recently, titanium dioxide (TiO_2) has been shown to display a similar sensing mechanism as SnO_2 and is being studied as a material that remains stable to higher temperatures, and has the potential to be a material of choice for sensing carbon monoxide (CO) with low cross sensitivity toward methane (CH_4) at temperatures between 400-700°C [Savage '01]. However, stability, sensitivity, and selectivity toward a particular gas of interest remain a challenge at these high temperatures due to gas interaction and instabilities in the material itself. Similar to SnO_2, various metal ion dopants and metal catalysts have been added to TiO_2 in attempts to alter the reaction between the sensor and specific gasses in the environment [Korotcenkov '05, Wisitsoraat '09, Teleki '08 Alessandri '07]. However, most of these attempts are aimed at lower operating temperatures in order to reduce operating costs for low temperature sensing applications, and only a few of them are aimed at improving the sensing characteristics at higher temperatures where the stability of TiO_2 can be utilized [Dutta '05]. Highly studied SnO_2-based sensors have been optimized to show high gas sensitivity and selectivity based on different material properties such as grain structure, chemistry, metal additives and dopants, and operation conditions. Provided sufficient background research on the material properties, this implies that TiO_2 has the potential to have similar sensitivity and selectivity to SnO_2 and can provide sensor arrays which can operate at higher temperatures.

Significant research on TiO_2 sensing has begun at The Ohio State University's Center for Industrial Sensors and Measurements (CISM). Groups lead by S. Akbar and P. Dutta have focused on optimizing the sensitivity and selectivity of TiO_2 thick and thin film sensors toward various target gasses for use in high operating temperature applications, as well as understanding several of the key fundamentals by which the TiO_2 gas sensing mechanism functions [Trimboli '06, Akbar '06]. Research there has lead to innovative new materials which are sure to play roles in future commercial sensors.

1.5 Effect of TiO_2 Crystallinity on Gas Sensing Mechanism

As described earlier, the gas sensing mechanism of TiO_2 relies on both bulk and surface conductivity. TiO_2 with perfect stoichiometry and crystal lattice would be void of any mobile charge carriers. The semiconductivity properties only arise due to defects such as oxygen vacancies in the crystal structure, which inherently occur in real materials. Therefore, the types and concentrations of these defects will play an important role in the gas sensing mechanism. In order to describe their effects, defects are broken into two categories: bulk and surface.

Bulk defects control the bulk conductivity of the TiO_2. The three common types of intrinsic defects are oxygen vacancies, titanium interstitials, and titanium vacancies. These defects are imperfections in the crystal lattice which result in charge nonequilibrium and thus create electronic defect sites within the band gap between the valance band (Ev) and conduction band (Ec), as shown in Figure 1.4. As described earlier, oxygen vacancies are the most prevalent intrinsic defect present in TiO_2. Because oxygen vacancies are associated with a loosely bound electron, they lie near the top of the band gap. With thermal excitation of approximately 1.18 eV in rutile TiO_2, these electrons can be excited into the conduction band and take part in

conduction. For this reason they are considered to be "donor" states because they can donate an electron to the conduction band. This process leads to the n-type electronic conduction behavior commonly observed in TiO_2. The other defects are still present in TiO_2, but at lower concentrations. Titanium vacancies results in unfilled bonds. Electrons from the valence band can then be thermally excited into this defect state. These defects are known as "acceptor" states because they can accept an electron from the valence band, leaving behind a "hole" which contributes to the p-type conductivity. Because these defects occur in a smaller concentration, they are considered the minority charge carriers.

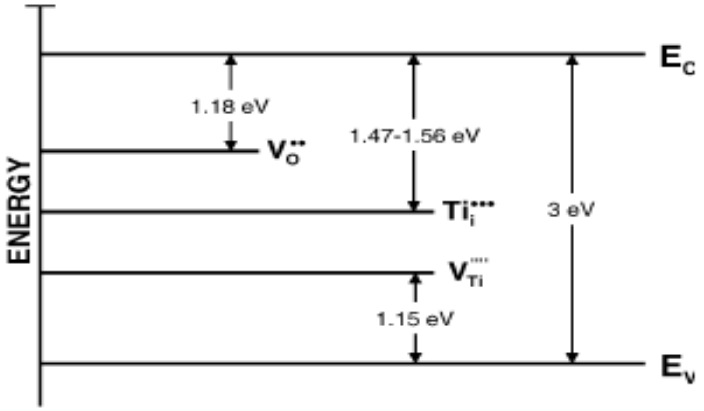

Figure 1.4. Electronic defect sites within the band gap of rutile TiO_2. $V_O^{\cdot\cdot}$ represents oxygen vacancies, V_{Ti}'''' represents titanium vacancies, and $Ti_i^{\cdot\cdot\cdot\cdot}$ represents titanium interstitials. Figure taken from [Nowotny '08].

Change in bulk conductivity with a change in oxygen partial pressure in the environment has been applied in bulk conductivity oxygen sensors. However, with the onset of nanotechnology and large increases in surface area, new surface-sensitive gas sensors are being fabricated. Because this surface-sensitive gas sensing mechanism does not rely on diffusion of oxygen, these sensors can be tuned to be sensitive toward many different oxidizing and reducing gasses. This surface sensing mechanism is, however, still centered around defects in the TiO_2. The surface-sensitive gas sensing mechanism relies on chemical species being adsorbed and desorbed from the TiO_2 surface. It has been shown that the predominant adsorption site for these

species is at a surface oxygen vacancy, as shown in Figure 1.5. In fact it was stated that no adsorption would occur on a stiochiometric TiO_2 surface [Linsebigler '95]. Therefore, surface defects play a crucial role in the gas sensing mechanism of TiO_2. Various types of these surface oxygen vacancies are shown in Figure 1.5. This trend of surface stoichiometry influencing the gas adsorption on the surface has been found to directly affect the gas sensing properties of MOS sensors [Brinzari '01, Vlachos '96, Gaggiotti '94]. Specifically, it was found that annealing an SnO_2 thin film improved the crystallinity which promoted better oxygen adsorption on the surface and lead to an improved gas sensitivity [Serrini '97]. Because TiO_2 possesses the same sensing mechanism as SnO_2, it is hypothesized that similar improvements in the crystallinity of TiO_2 can be used to improve the gas sensitivity.

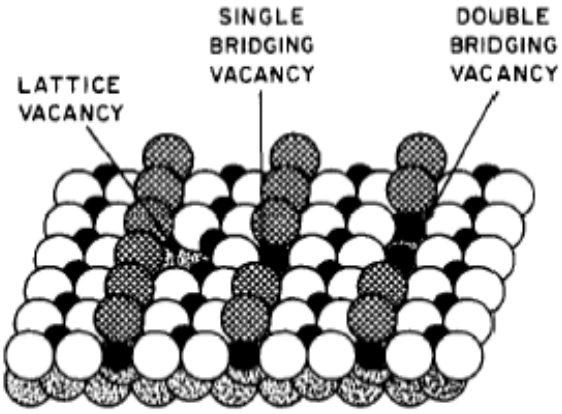

Figure 1.5. Various types of surface defects on TiO_2. Lattice and bridging oxygen vacancies are shown. Figure taken from [Linsebigler '95].

This process of annealing can be used to improve the crystallinity and therefore sensitivity of these types of gas sensors; however, it will most often also lead to grain growth, reduction in surface area, and possibly even phase change, hurting the gas sensitivity. These two competing factors will ultimately control the total number of adsorption sites on the surface of the material and thus the gas sensitivity. Reaching a compromise between these two factors, by

controlling processing conditions for each sensor material, can lead to optimum conditions, providing the highest gas sensitivity.

1.6 Effect of TiO_2 Chemistry on Gas Sensing Mechanism

In the previous section, changing the stoichiometry in the both the bulk and surface of MOS gas sensors was explained to have significant effects on the sensing performance by introducing intrinsic point defects. Another method of introducing defects into a crystal lattice is through extrinsic doping. Introducing an atom other than titanium or oxygen will change the chemistry of the compound and will have significant effects on the material properties. Incorporation of impurity ions in MOS sensors has proven to be a very effective method for improving many of the sensing characteristics by altering the defect concentrations, stabilizing crystalline phases, and catalyzing gas-surface reactions. Table 1.2 lists an examples of the key literature findings of several dopants in TiO_2 which have been used to improve the gas sensing properties.

As stated earlier in section 1.4, the anatase phase of TiO_2 is considered more reactive and sensitive than rutile, and is therefore more desireable for gas sensors. However, during the crystallization process at high temperatures, it is possible to form rutile which is the more thermodynamically stable phase. The use of dopants as anatase phase stabalizers is one method that has proven effective to overcome this problem. Groups lead by S. Akbar and P. Dutta at The Ohio State University's Center for Industrial Sensors and Measurements (CISM) found that addition of lanthanum oxide in TiO_2 thick films stabilized the anatase phase to promote better sensing properties [Dutta '99]. They also found that incorporation of lanthanum in TiO_2 results in more adsorbed oxygen and better CO sensitivity. Similar results were found for dopants of

Table 1.2. Literature survey of dopants used to enhance TiO_2 gas sensing.

Dopant	Film type/ deposition	Target Gasses	Operating Temp (°C)	Findings	Reference
Nb	thin/ sputtering	NO_2	600	Nb lowered resistance	Yamada '00
Nb	thin/ sol-gel	CO Ethanol	300	Nb→improved CO response, degraded ethanol response	Ruiz '03
Cr, Nb	thin/ sputtering	O_2, H_2	623-723	Cr→fast diffusion of O vacancies Nb→slow diffusion of Ti interstitials	Zakrzewska '04
Cr, Nb, Sn	thin/ sputtering	H_2	575-775	Acceptor→fast response Donor→lower operating temp.	Zakrzewska '97
Cr	thin/ sputtering	CO, ethanol	300	Cr→decrease resistance, sensative to ethanol	Alessandri '07
Cr	thin/ sol-gel	NO_2	400	Cr→p-type response	Li '02
Cr	thin/ sol-gel	CO, NO_2	250-500	Cr→anatase stabalization, p-type	Ruiz '03
Nb, Cu	Thick/ Doc blade	CO, ethanol	400	Cu→improved selectivity to CO	Teleki '08
Mo	thin/ sol-gel	CO NO_2	300-400	Mo→lower operating temp	Galatsis '01
W, Mo	thin/ e-beam	NO_2 CO acetone ethylene	200	W→lowers resistance, improves NO_2 acetone, ethylene respones,. Mo→improves response to CO	Wisitsoraat '05
W	thin/ sol-gel	Ethanol methanol	300-500	Ethanol selectivity	Garzella '03
W	thick/ brush coat	CO, H_2, H_2S, LPG	100-350	High H_2 response	Chaudhari '06
Ni	thin/ e-beam	acetone Ethanol CO	200-500	10%Ni needed to form p-type respone	Wisitsoraat '09
Pt	thin/ sol-gel	H_2	330-720	High H_2 response	Epifani '08
Ce	thin/ sol-gel	O_2	250-470	Ce→lower resistance and higher response	Trinchi '03
Cu, La	thick/ screen printing	CO	600	La→stabalized anatase Cu→CO selectivity	Dutta '99 Savage '01
Ga	thin/ sol-gel	CO, NO_2	200-500	Gas response imrpoved	Mohammadi '07
Y, Al	thick/ screen printing	CO, H_2	400-600	Al→H_2 selectivity Y→CO selectivity	Birkefeld '92
Au,Ag, Pt, Pd, Nb, V	Thick/ Screen printing	CO	400-550	Au/Pd stabalized anatase phase Au→improved gas response	Ruiz '05

niobium and tungsten [Anakunprasert '05, Garsella '03]. We have previously reported that aluminum doped TiO_2 required higher crystallization temperatures than pure TiO_2 to achieve a high gas sensitivity, implying that the addition of aluminum slowed the crystallization process in TiO_2 [Choi '07]. Other dopants such as copper and cromium have been shown to promote the anatase-to-rutile transformation at lower temperatures [Dutta '99, Zakrzewska '97]. These dopant effects on phase and crystallinity of TiO_2 will then influence the gas sensing properties as described in section 1.5.

A second, more significant effect that dopants can have on the sensing properties of TiO_2 is through the creation of charged defect sites. Just as an oxygen vacancy leads to the formation of conduction electrons, a substitution defect from an atom with different valence from the host atom can also lead to mobile charges able to contribute to the electronic conductivity of the material [Ferroni '00]. Depending on the valence of the dopant atom compared with the valence of the host atom, the defect will either be a donor or accpetor site. For simplicity, substitution of only the cation will be discussed here as it is the most common. Also, because this work focuses on tungsten and nickel as the donor and accpetor dopants respectively, these will be the examples used to explain extrinsic defects.

Tungsten substitution in the place of titanium in the TiO_2 lattice will result in donor defects [Komornicki '04]. Tungsten can have multivalency between W^{4+} and W^{6+} with W^{6+} being the most stable. If a W^{6+} replaces a Ti^{4+} in the TiO_2 lattice, there will be en excess of two extra positive charges denoted ($W^{6+}_{Ti4+}{}^{\cdot\cdot}$**).** Therefore, by charge conservation, there will be two extra electrons that are unable to participate in the W-O bonding and are therefore weakly bound to the defect site, as shown in Equation 4. These electrons can then be thermally excited into the

conduction band and participate in n-type electronic conduction, much like the oxygen vacancy defects described earlier.

$$TiO_2 \xrightarrow{W} W_{Ti^{4+}}^{6+\bullet\bullet} + 2O_O^X + 2e^- \quad (4)$$

Nickel substitution in the place of titanium in the TiO_2 lattice will conversely result in the formation of acceptor defects. Nickel is also a multivalent ion between Ni^{2+} and Ni^{4+} with Ni^{2+} being the most stable. If Ni^{2+} replaces a Ti^{4+} in the TiO_2 lattice, it will not have enough valence electrons to satisfy all the Ni-O bonds and will therefore have two open 'holes' ($h^{\cdot}$) where it can easily accept an extra electron from the valence band, as shown in Equation 5. Electrons that are excited from the valence band into the acceptor site leave behind a 'hole' in the valence band that can then contribute to p-type electronic conduction.

$$TiO_2 \xrightarrow{Ni} Ni_{Ti^{4+}}^{2+\prime\prime} + 2O_O^X + 2h^{\bullet} \quad (5)$$

Similar reactions can be written for other extrinsic dopants in TiO_2. Depending on the nature of the dopant, the defect site will either be a donor site near the conduction band, or an acceptor site near the valence band. Figure 1.6 gives an energy band diagram showing the defect

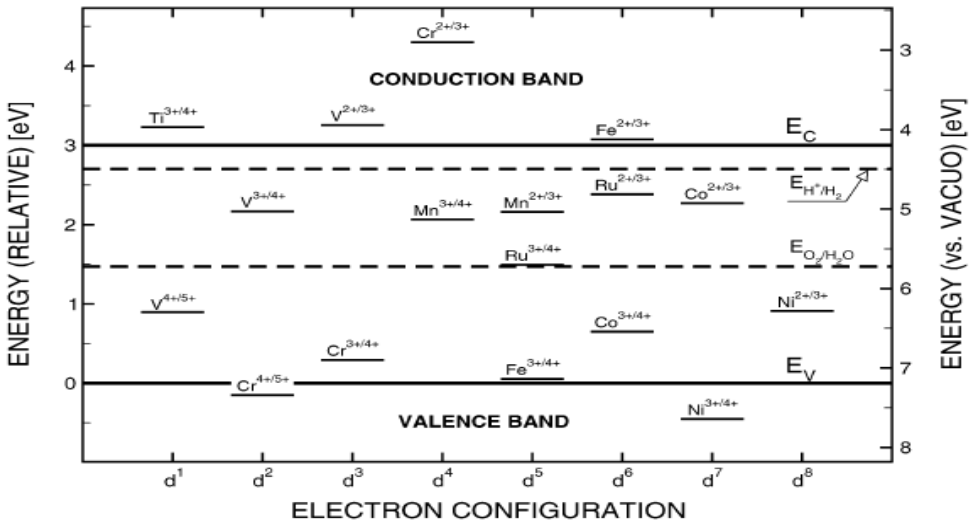

Figure 1.6. Band diagram of rtuile TiO_2 showing energy levels of different dopant ions, according to [Nowotny '08]

site positions of several different dopants. The example of nickel substitution given above results in an acceptor site, and as expected, can be seen to lie within 1 eV of the valence band.

Incorporation of these extrinsic donor and acceptor defects in MOS gas sensor materials has been extensively studied, and results show that dopants can significantly enhance the sensing properties. However, each dopant appears to have a unique effect on the different MOS materials, and with a seemingly endless combination of MOS material, fabrication methods, processing conditions, dopants, target gasses, and sensing parameters, there are still many stones left unturned when optimizing a sensor for a specific application. In this research, we chose to focus our attention on tungsten and nickel as two dopants which have opposite affects, but are both promising candidates for improving the gas sensing properties of TiO_2.

Tungsten was chosen specifically for this study as a dopant in TiO_2 gas sensors for several reasons. The ionic radii of tungsten (74.0 pm) and titanium (74.5 pm) [Barsoum '03] are comparible in size, and it has been shown that some tungsten is soluble in the TiO_2 lattice [Komornicki '04]. Tungsten oxide is already known to be a MOS sensor material that is operable at high temperatures and is sensitive to oxidizing and reducing gasses [Siciliano '08, Stankova '05]. Tungsten also shows multivalency between +4 and +6, indicating that it could enhance the oxidation/reduction reactions on the sensor surface [Stankova '05]. In addition, tungsten has previously been shown to stabilize the anatase phase in TiO_2 [Ramis '92, Yang '02], however its effect on the sensing properties of TiO_2 has not received significant attention. Tungsten was chosen here as an n-type dopant in TiO_2 which should act as a donor impurity to donate electrons to the conduction band.

Nickel was chosen as the second dopant for similar reasons as tungsten, but to have an opposite effect. The ionic radius of nickel is 83 pm [Barsoum '03], which is slightly larger than

titanium, but close enough to expect possible atomic substitutions in the TiO_2 lattice. Nickel oxide is yet another MOS material used for gas sensors which is operable at high temperatures [Luyo '09, Brilis '07]; however, it shows a rather unusual p-type sensing response which is different from the more standard MOS sensors such as SnO_2, TiO_2, or WO_3. This p-type behavior has been shown to originate from nickel vacancies and oxygen intersitials [Yang '05]. Nickel doping in TiO_2 photocatalysts was shown to improve the catalytic activity by decreasing the particle size and improving the hydrophilicity of the surface [Sharma '06]. Recently, A. Wisitsoraat et al. showed that addition of 10 wt.% NiO in TiO_2 thin film gas sensors was able to convert the sensing response to a p-type majority [Wisitsoraat '09]. Nickel was chosen here as a p-type dopant in TiO_2, which should act as an acceptor impurity creating 'holes' in the valence band, contributing to p-type conduction in TiO_2. Because of its unusual behavior, p-type conduction sensing response has the potential to introduce new ways to achieve gas selectivity in MOS sensors.

1.7 Thin Film MOS Gas Sensors

Originally, TiO_2 has been studied as a high temperature bulk conduction sensor where the conductivity is a function of the oxygen partial pressure [Park '03]. More recently, it was discovered that thick films of TiO_2 had similar surface reactions and sensing mechanism as SnO_2, but could be operated at higher temperatures [Dutta '99]. Thick films (thicker than a few μm) have similar stability to bulk materials, but more surface area-to-volume ratio, giving better sensitivities. The majority of the work in the recent past has focused on thick film materials [Akbar '06]. As stated earlier, the improvement of MEMS fabrication techniques, and knowledge of thin film (less than one μm) deposition and characterization has become more

advanced, and this technology has been successfully implemented in the field of MOS gas sensors to improve the performance. Due to the small dimensions in one direction, the surface area-to-volume ratio increases, changing the fundamental behavior of the material. The surface is much more reactive than the bulk, showing a more sensitive response to trace amounts of target gas.

Thin film geometry, which provides an increase in sensor reactivity and valuable improvements to many response properties, also imposes a major limitation on the sensors' versatility. The higher surface energy provides more driving force for the annealing process to happen during operation, which can include severe grain growth, phase change, film cracking, and reaction with the substrate material. This has lead to TiO_2 thin film sensors that show degraded sensitivity and selectivity at operating temperatures above 300°C [Al-Homoudi '06, Sadek '09, Mardare '08].

These results have highlighted the need for thin films with improved stability that can maintain good sensitivity and selectivity during operation at temperatures above 500°C [Akbar '06]. By utilizing stable crystal structures and incorporation of specific metal dopants into the TiO_2 structure, we believe the sensitivity, selectivity, and stability during operation at high temperatures can be improved. With better material stability, the high sensitivities of thin film sensors can be utilized while not limiting the sensors' operating temperature.

1.8 n-p Junction Composite MOS Gas Sensors

MOS sensor gas detection is based on change in electronic conductivity through a film. A change in gas environment causes a change in carrier concentration by altering the depletion layer thickness on the surface of the MOS. Composite material gas sensors made of an n-type

MOS in contact with a p-type MOS have shown the possibility to improve both sensitivity and selectivity through the incorporation of a p-n junction. Incorporation of a p-n junction will provide a second type of depletion layer (space charge region) caused by the recombination of electrons and holes, as shown in Figure 1.7, which may be useful in enhancing the gas response.

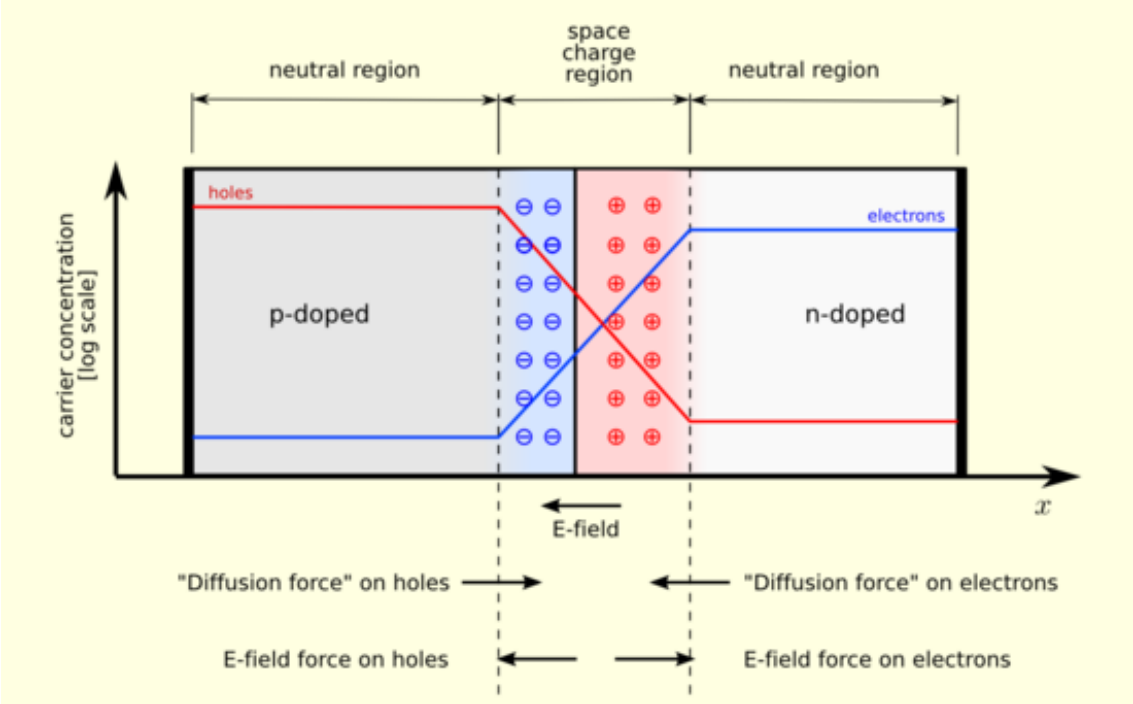

Figure 1.7. Diagram of a standard p-n junction showing the carrier concentrations, space charge region, electric fields present. Taken from www.wikipedia.com

Often these sensors have utilized a p-n heterojunction between two oxides with different major carrier concentrations, such as p-type copper oxide (CuO) and n-type tin dioxide (SnO_2) or zinc oxide (ZnO) [Katti '03, Dandeneau '09]. p-n homojunctions consisting of a single oxide with different major charge carriers are more difficult to create but have the advantage of similar material properties across the junction [Hazra '06, Stamataki '08]. In addition to the effects of a p-n junction depletion region, thick film n-p composite TiO_2 sensors have also been shown to improve selectivity by controlling the percolation paths for both electrons and holes within the film [Savage '01]. Table 1.3 gives lists the literature studies involving n-p junctions.

Table 1.3. Literature survey of the p-n junction materials used in MOS gas sensors.

Material(s) Used	Operating Temp. (°C)	Critical Findings	Reference
ZnO homojunction	300-400	Sensitive to H_2 Slow response Poor interface	Hazra '06
NiO homojunction	25-125	H_2 response	Stamataki '08
n-SnO_2 p-CuO	140-260	Sensitivity to H_2S	Katti '03
n-ZnO p-CuO	200	Sensitive to H_2 when CuO on top.	Dandeneau '09
Ni-doped CuO Ga-doped ZnO	400	Sensitive to H_2 Doping improved response time and sensitivity	Aygun '05
(Li,Na,Ca,Sr,Ni)-doped CuO ZnO	400	Sensitive to H_2, Ni-doped CuO best sensitivity	Aygun '05 (#2)
CuO/ZnO	100-325	CO selectivity	Nakamura '86
CuO/ZnO	250	Junction facilitates oxidation of CO	Nakamura '90
CuO/ZnO	300	Quenching CuO improved sensitivity	Nakamura '98
ZnO/La_2CuO_4	400	Higher sensitivity than CuO/ZnO	Traversa '04
$SmCoO_x/MO_x$ (M=Fe,Zn,In,Sn)	100-500	$SmCoO_3/Fe_2O_3$ had best response to ethanol	Mochinaga '98

In this work we are focused on the effects of TiO_2-based homojunctions on the gas sensing properties of thin films. In n-type TiO_2, the presence of a reducing gas provides extra electrons, lowering the resistance. In p-type material, the reducing gas also provides electrons, which annihilate holes (the major carrier) and increase the resistance. The voltage (V_o) and width (W_o) of a p-n junction depletion layer is dependent on the carrier concentration in both the n- and p-type materials as described in Equations (6) and (7).

$$V_o = (kT/e)\ln[N_A N_D/n_i^2] \quad (6)$$

$$W_o = [\{2\varepsilon(N_A+N_D)V_o\}/eN_A N_D]^{0.5} \quad (7)$$

where N_A is the acceptor carrier concentration (holes), N_D is the donor carrier concentration (electrons), and n_i is the total intrinsic carrier concentration. It is hypothesized here that the action of a reducing gas reacting with the p-n junction will cause N_A to decreases slightly and N_D to increase, resulting in an overall decrease in V_o. This decrease in V_o will then result in a narrowing of the depletion region W_o and a shift toward the p-type material due to the change in carrier concentration, as shown in Figure 1.8. These two results will cause a similar effect to a forward bias and increase the conductivity across the junction. These effects engineered in a TiO_2 gas sensor can be utilized to make the resistance in air higher and the resistance in reducing atmosphere lower, resulting in an overall larger response.

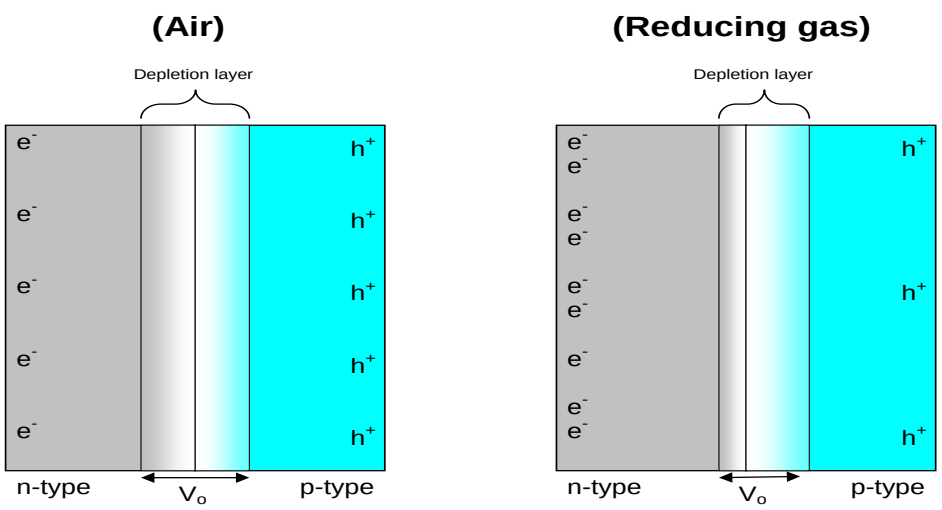

Figure 1.8. Schematic of a TiO_2 p-n junction in the presence of air (oxidizing) and CO reducing gas.

1.9 Objectives and Research Plan

This introduction has outlined the need for gas sensors which can operate in high temperature harsh environments, and the potential for TiO_2-based MOS sensors to fit specific applications of measuring carbon monoxide under these circumstances. It has also been shown that the sensing mechanism is not completely understood, and TiO_2 sensors need further research

to determine specific material properties which can be engineered to overcome a few of the specific deficiencies such as selectivity and stability. Specifically, the need for improving these material properties in thin film sensor modifications has been expressed. By studying the effects of several key TiO_2 material properties on the sensing performance, we hope to gain better scientific understanding of the sensing mechanism and how the material can be engineered to better fit specific applications.

The objective of this research is to study the effects of crystallinity and chemistry of TiO_2 gas sensors on the sensing performance in order to gain understanding of the sensing mechanism and influential material properties. Both crystallinity and chemistry will influence several of the key material properties of TiO_2 films involved in gas detection. Altering the chemistry of the films can also have a direct effect on the crystallinity, and therefore it is important to distinguish between these two effects. Figure 1.9 gives a visual diagram of the research plan, describing specific material properties of interest and operating conditions for gas sensing measurements. This research has been focused on three different areas:

1) Crystallinity of TiO_2 films: TiO_2 crystallinity in both thick and thin films has been controlled by the film heat treatment temperatures between 600 and 900°C to study the effect on gas sensing properties toward reducing gasses carbon monoxide (CO) and methane (CH_4) at high operating temperatures between 400 and 700°C.

2) Chemistry of TiO_2 films: The effect of chemical composition on gas sensing properties of both thick and thin films was studied by introducing the choice dopants nickel and tungsten during synthesis.

3) TiO_2-based p-n homojunction films: In an extension of the study on chemical doping of TiO_2 thin films, bilayer films composed of n-type W-doped TiO_2 and p-type Ni-doped TiO_2 have been fabricated to study the effect of p-n homojunctions on the gas sensing properties.

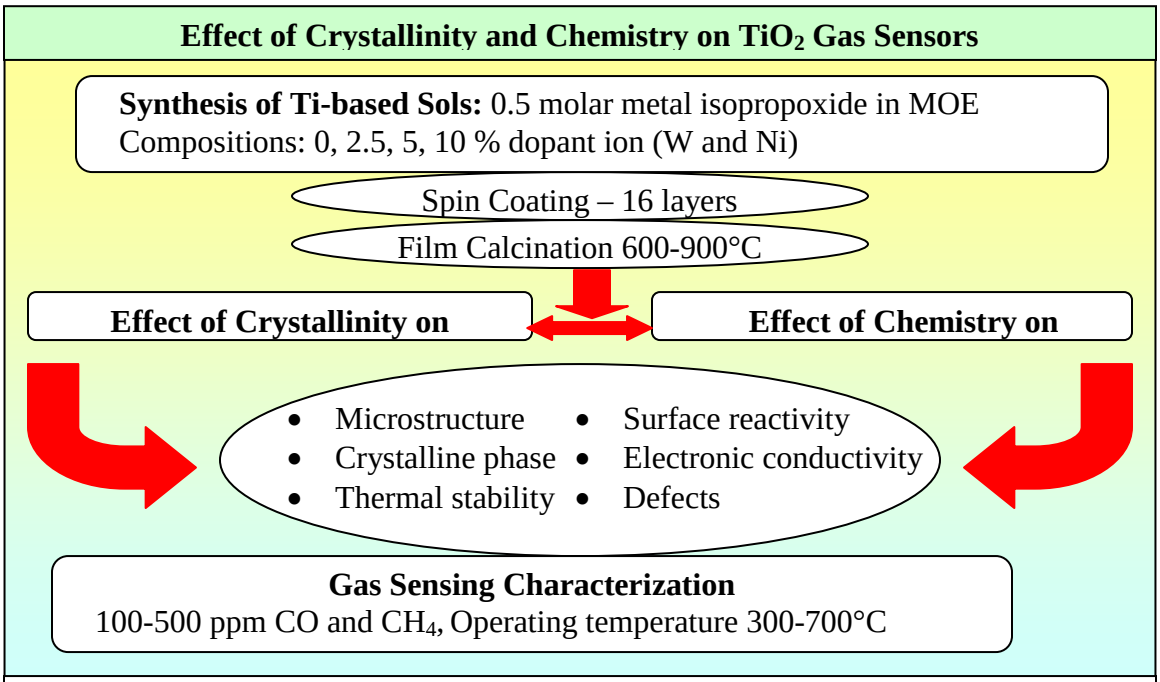

Figure 1.9. Schematic for studying the effect of crystallinity and chemistry on the sensing behavior of TiO_2 thin films.

CHAPTER TWO

EXPERIMENTAL

2.1 Citrate-Nitrate TiO_2 Nano-Powder Synthesis

In order to investigate the role of TiO_2 crystallinity in thick film gas sensors, we chose to synthesize our own TiO_2 nano-powder via the citrate-nitrate auto-combustion method which is a modified version of the Pechini method [Pechini '67]. The Pechini process is one of many sol-gel techniques available, in which a chelated complex is formed between a mixture of cations and carboxylic acid groups such as citric acid, as shown in Figure 2.1. The cations are then uniformly dispersed throughout a gel structure. During heating, the chelated complex is calcined leaving behind the metal cations which are subsequently oxidized and crystalized. This method produces high purity nano-powder with close control over the chemistry and crystallinity of the synthesized product. Chemistry is controlled by the starting ingredients while crystallinity is controlled by the final calcinations and heat treatment process. We have previously performed an in-depth study on several of the synthesis parameters associated with this process and had success fabricating thick film gas sensors from the synthesized TiO_2 powder [Choi '04, Choi '07, Seeley '09].

The starting titanium source was commercial TiO_2 powder (Dupont, Ti Pure R-900, Wilmington, DE). In a plastic beaker 50 g of commercial TiO_2 powder was kept for 1 day in 250 ml hydrofluoric acid (HF) (J. T. Baker, Assay, 48-50%, Phillipsburg, NJ) to prepare the TiF_4 solution. After 1 day the solution was filtered using 11 µm filter paper (Whatman No 1). Ammonium hydroxide (NH_4OH, J. T. baker, Assay 28-30%) was added drop-wise to the filtered liquid for complete precipitation between pH 10 and 11. The precipitate was then washed 6

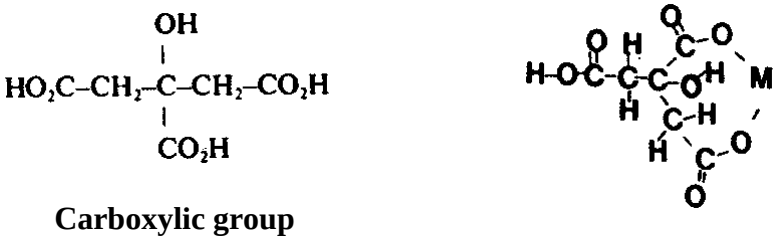

Figure 2.1. Structure of Citric Acid (A) and Chelated Citric Acid (B).

times with distilled water to remove any remaining reagents. The precipitate was then dissolved in nitric acid solution containing 25% water and 75% concentrated nitric acid (HNO_3, Fisher, Assay 69.5%) at 80°C with continuous stirring via a magnetic stir bar. A clear and homogeneous Ti^{4+} solution was obtained. To determine the concentration of Ti ions, 10 ml of this solution was removed and mixed with ammonium hydroxide until complete precipitation. This precipitate was then filtered with ashless filter paper and then calcined at 800°C for 2 hours. The weight of this calcined product was then used to calculate the Ti concentration in the original solution. For example calculations please see [Choi '04]. The solution was adjusted to 0.5 molar Ti and 10 molar HNO_3 by addition of water and nitric acid. Citric acid was then added to this Ti nitric solution with a citrate-to-nitrate ratio of 1.0. The solution was stirred constantly and heated on the hot plate to 100°C until it became completely clear. The solution eventually began to boil and evaporate. After several hours of concentration the solution began to turn yellow and eventually started to bubble. At this point the stir bar was removed and the heat was increased to 300°C. The solution began to char and became completely dry and black. This black char was ground in a mortar and pestle until a fine powder was obtained. This powder was then calcined in an alumina crucible in a muffle furnace for 1 h at temperatures of 400, 500, 600,

700, 800, 900, or 1000°C to obtain the final TiO_2 nano-powder. A flow chart and pictures of this citrate-nitrate auto-combustion method is shown in Figure 2.2.

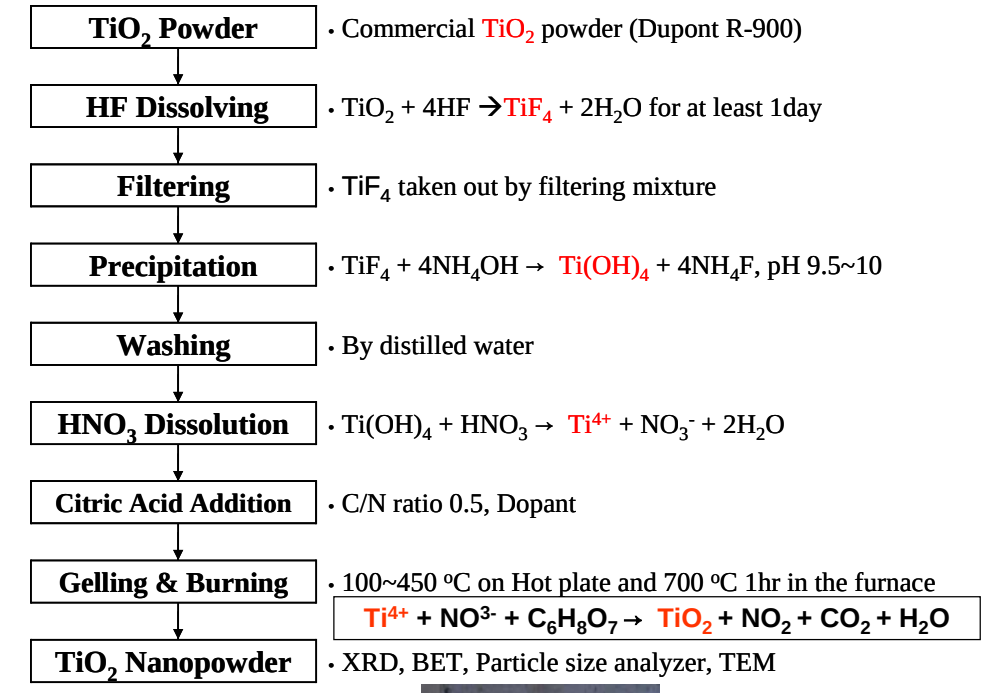

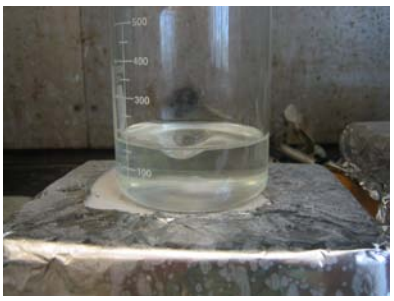

Ti Citrate-Nitrate Solution

Heating

Precalcined powder

Figure 2.2. Flow chart and pictures of TiO_2 nano-powder synthesis using citrate-nitrate auto-combustion method.

2.2 Nano-Powder Characterization

TiO_2 nanopowder was characterized for phase analysis using X-ray diffraction (XRD) (Siemens D500 Kristalloflex, Madison WI) with a Cu-Kα radiation source and settings of 30 mA and 35 kV. Crystallite size (D) was calculated using the full width at half maxima (FWHM) (β) of the anatase (101) and rutile (110) peaks using the Scherrer equation (8) [Cullity '78].

$$D = K\lambda/\beta\cos\theta \quad (8)$$

Where (K) is the shape factor estimated to be 0.9, (λ) is the wavelength of the x-ray source (1.54Å), and θ is the angle of maximum peak intensity. From this data a qualitative comparison of crystallite size was made for powder calcined at different temperatures.

Transmission electron micrographs (TEM) were taken on a Jeol JEM 120 electron microscope to determine the particle size. Nanopowder was dispersed in an aqueous solution, ultrasonicated for 30 min., pipetted onto a copper grid, and dried for 30 min. before analysis.

Specific average surface area was measured using a five point BET surface area analyzer (Tristar 3000, Micromeritics, GA) with N_2 adsorption. Samples were degassed under flowing nitrogen at 300°C for at least 3 hr or until no condensation appeared in the sample tube. A theoretical particle size was calculated from the surface area assuming spherical non-porous particles and an anatase density of 3.9 g/cm^3.

Differential scanning calorimetry (DSC, Netzsch STA 409 PC, Germany) was assessed from 400 to 1300°C at a heating rate of 2°/min to assess the amorphous content of the powder which remained after calcination at various temperatures.

2.3 Thick Film Element Fabrication and Sensing Measurements

For organization and clarity purposes, this section is divided into three subsections: substrate preparation, slurry and film processing, and film characterization (including material and gas sensing properties). Thick film processing is described and pictured in Figure 2.3.

2.3.1 Preparation of the alumina substrate

In order to measure the electrical resistance of a film at high temperature, a non-conductive substrate with high stability was needed. The Center for Micro and Nano Processing

at Case Western Reserve University specializes in making substrates for this type of research. The substrate used was item #102 in their catalog. Alumina substrate provides low conductivity and stability at high temperatures. In order to measure the film resistance, gold electrodes have been screen printed onto the substrate in an interdigitated pattern as shown in Figure 2.3. 3 inch long silver wires (Alfa Aesar, 0.25mm dia. 99.9%) were attached to the substrate. First, wires were mechanically attached by wraping through and around the provided holes in the alumina substrate and then they were electrically connected by placing a small bead of platinum paste (Engelhard, A4731) covering where the wire and gold electrode overlapped. This paste was allowed to dry at room temperature overnight and then was allowed to cure and sinter at 900°C for 1 hr. This made a strong mechanical and electrical connection between the gold electrode and silver wire.

2.3.2 Powder slurry and thick film processing

Thick film sensing elements, shown in Figure 2.3, were created by depositing slurry composed of calcined TiO_2 nanopowder and α-Terpineol (Alfa Aesar, 95%) on the prepared substrates. α-Terpineol was chosen as a medium with relatively high viscosity to produce a stable powder suspension. 100 mg nano-powder was added to 1ml α-Terpineol and stirred thoroughly. This solution was then ultrasonicated for 15 min and stirred again before application. Two drops of this homogeneous slurry was deposited from a plastic transfer pipette onto the electroded alumina substrate and the slurry was spread to cover the entire substrate evenly. This slurry was allowed to dry at room temperature for 24 hr and then sintered between 700 and 900°C for 1 hr in a muffle furnace to create the final sintered thick film sensing element. This sintering process was performed in the same muffle furnace as the powder calcination; however, the term sintering refers to the formation of the film with interconnected particles.

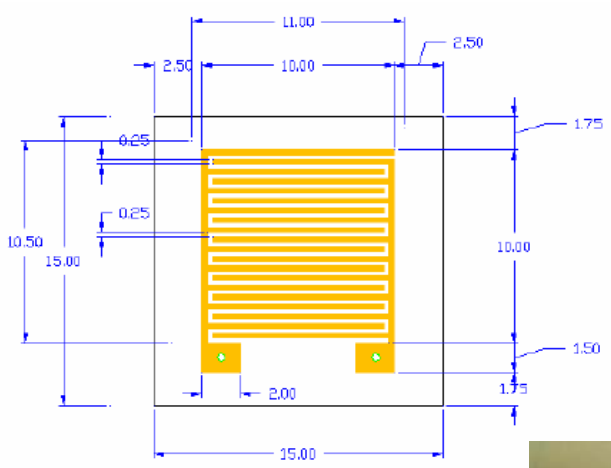

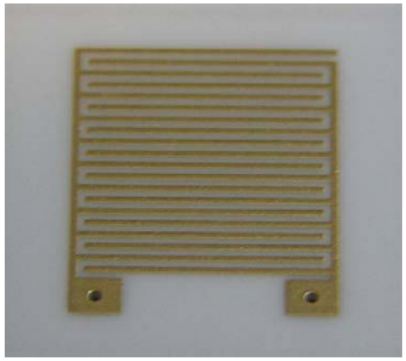

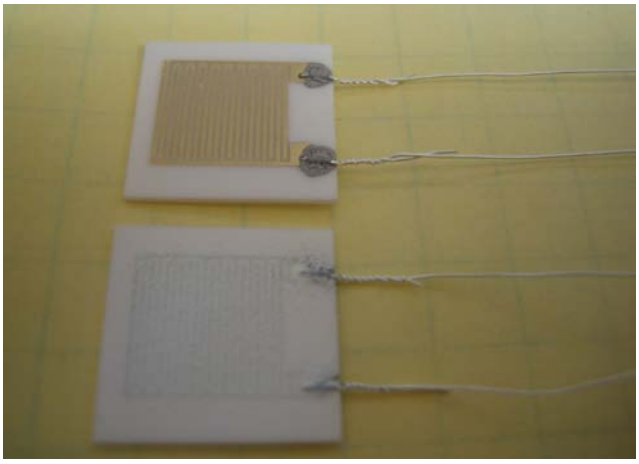

Thick Film Processing Procedure

1. Create a slurry with (0.1g) calcined powder and (1ml) α-terpineol.
2. Ultrasonicate 30 minutes.
3. Paste 2 drops slurry on alumina substrate with gold electrodes.
4. Let dry 24 hours.
5. Sinter the film (700 or 800°C).
6. Place in controlled environment furnace at 600°C - 10%O_2/N_2.
7. Let resistance stabilize for 24 hr.
8. Oxygen and carbon monoxide test.

Figure 2.3. Schematic diagram and photo of sensing element substrate obtained from Case Western Reserve University's Center for Micro and Nano Processing item #102. Dimensions are labeled in mm. Blank substrate after silver wires attached and substrate with thick TiO_2 film. Thick film processing procedure.

2.3.3 Thick film characterization

Microstructure of the films top surface was characterized using a field emission scanning electron microscope (FE-SEM; FEI, SIRION, OR) with an operating voltage of 5kV. To characterize the gas sensing properties the thick film sensing elements were held by a quartz sample holder equipped with silver wires and placed in a 30 mm inner diameter quartz tube running through a tube furnace at 600°C. Starting gas reagents were cylinders of dry high purity air, nitrogen, 1000 ppm CO in nitrogen, and 1000 ppm CH_4 in nitrogen. Gas composition flowing through the quartz tube was controlled using ball flow-meters and was kept at a constant

gas flow rate at 150cc/min. Each ball flow meter had been previously calibrated using an Agilent digital flow meter as shown in Figure 2.4. Using the electrodes on the substrate, two probe electrical resistances of the thick film samples were measured using a Keithley SourceMeter 2400 and data was automatically collected on a computer using Excel. A schematic diagram of the gas sensing set-up is shown in Figure 2.5. The baseline gas composition was kept constant at 10% O_2 balanced by 90% N_2. Film resistance was allowed to stabilize at 600°C with the baseline gas composition flowing for 24 hr prior to the start of the sensing measurements. For the sensing measurements, film resistance was measured as a function of oxygen content (2 to 10%) first, and then carbon monoxide concentration (0 to 500ppm) in a nitrogen stream containing a constant 10% O_2 as shown in Figure 2.6. Sensing operating temperature was kept constant for all thick films at 600°C. Powder calcination and element sintering temperatures are denoted by calcination temperature first followed by sintering temperature (e.g. calcination at 800°C and sintering at 700°C is denoted as "C800-S700"). Triplicates of each film were fabricated and tested in the sensing chamber in order to verify

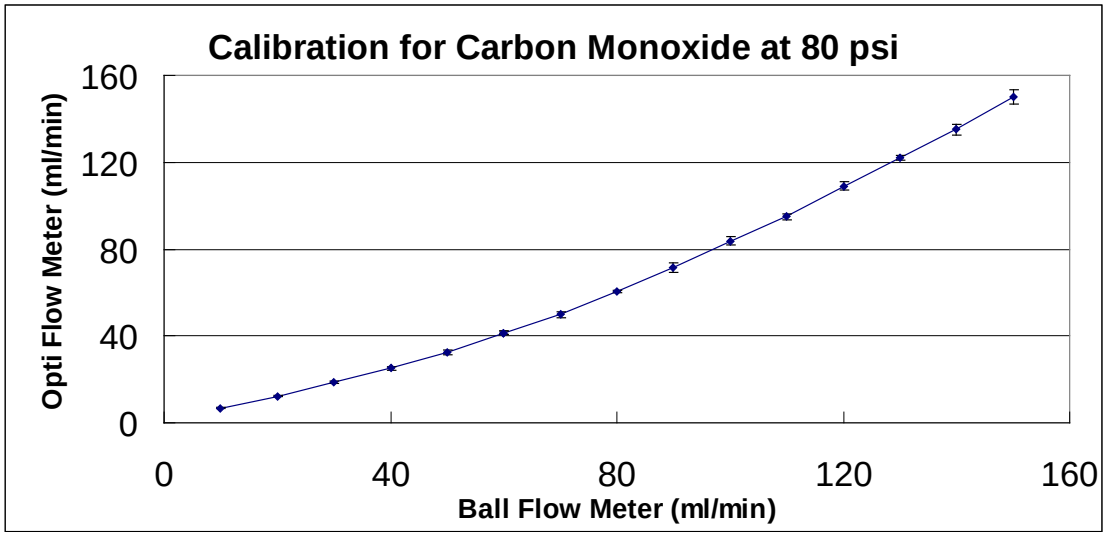

Figure 2.4. Example of ball flow meter calibration for carbon monoxide using the Opti-flow digital flow meter. Similar calibrations were made for other gasses and ball flow meters.

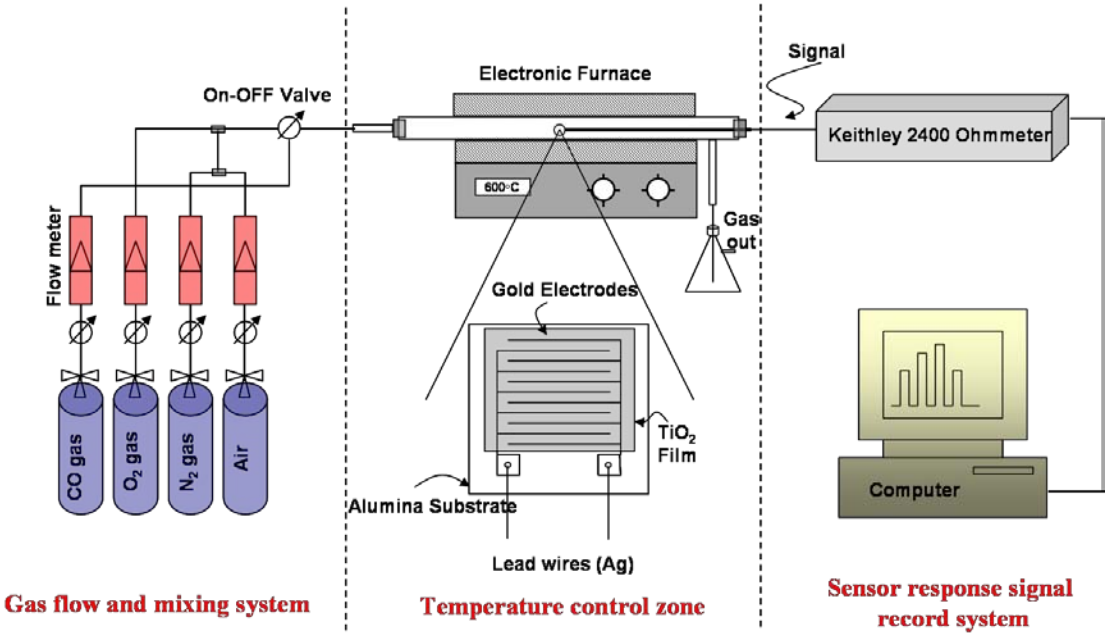

Figure 2.5. Schematic diagram of the gas sensing set-up; including the gas mixing zone, temperature control zone, and signal recording zone. Set-up originally designed by Young-Jin Choi and later modified to accommodate two films simultaneously by Zachary Seeley.

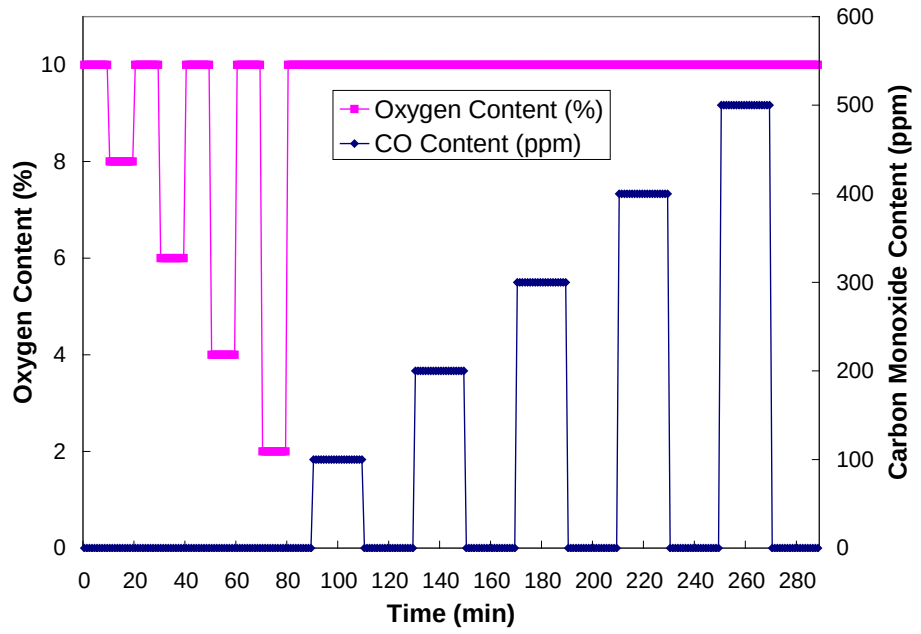

Figure 2.6. Sensing test gas concentrations and durations for measuring oxygen and carbon monoxide gas response. Oxygen durations were 10 minutes and CO durations were 20 minutes to allow full response.

results and gain knowledge of reproducibility. Standard deviations of these results are reported in the form of error bars to show differences between samples. Gas response is defined here as the ratio of the film resistance in the presence of the target gas (Rg) to the film resistance in the background gas (Ro) as shown in equation 9.

$$Gas\,\mathrm{Re}\,sponse = \frac{Rg}{Ro} \tag{9}$$

2.4 Tungsten-Doped TiO_2 Nano-Powder and Thick Film Processing

In order to characterize the effect of tungsten-doping on the properties of TiO_2 nano-powder and thick film sensing elements, commercial tungsten oxide (WO_3) nano-powder (NanoAmor, 99%, 50 nm APS) was added to commercial TiO_2 nano-powder (Alfa Aesar, 99 %, 10 nm APS, surface area 100 m^2/g). Powder ratio's of 0, 1, and 5 wt. % WO_3 (denoted 0W, 1W, and 5W respectively) were wet milled in ethanol together for 24 hours using yttria stabilized zirconia milling media. Slurry consisted of 5 g nano-powder, 20 ml ethanol, and 50 g YSZ balls in a 60 ml bottle. Slurry was dried and milled further to obtain the homogeneous mixture of nano-powder. Powder was calcined in a muffle furnace at 800, 900, 950, 1000, and 1050°C for 1 hour in air environment. XRD, BET, and DSC analysis was preformed on the powder as described earlier. Thick films were also fabricated from the calcined nano-powder, sintered at 800°C for 1 hr, and tested for gas sensing as described earlier.

2.5 Sol-Gel Spin Coating Thin Film Fabrication

Previously, we have successfully used sol-gel processing to create thin films of lead zirconate titanate on silicon wafers [Myers '02, Akasheh '04]. We have used a modified version

of the same processing technique to create thin films of TiO_2 for sensing applications on silicon wafers and the prepared alumina substrates.

Titanium-based metal-organic sols were created by dissolving titanium (IV) isopropoxide ($Ti[OCH(CH_3)_2]_4$ 97 % min., Alfa Aesar) in 2-methoxyethanol ($CH_3OCH_2CH_2OH$ 99.3+ %, Alfa Aesar) in an argon atmosphere. Ionic concentration of titanium was kept at 0.5 M. The solution was stirred and refluxed in an oil bath at 120°C for 6 h under constant argon flow to ensure homogeneity. Thermogravimetric analysis and differential scanning calorimetry (TGA and DSC, NETZSCH STA 409 PC, Germany) were performed on the precursor solution to determine calcination and crystallization temperatures at a heating rate of 5°/min to 1500°C.

Thin film fabrication was performed on two different substrates. A silicon wafer (100) was used as a smooth substrate to measure film thickness and an alumina substrate with interdigitated gold electrodes was used to measure film resistance for gas sensing properties. Film deposition was accomplished via spin coating the precursor solution onto the substrates. A photo resist spin coater with a vacuum chuck was used at 3000 rpm for 30 s. After each layer was applied the film was dried on a hot plate at 400°C for 10 min. The hot plate was then turned off and let to cool for 10 min. before the next layer was applied. After every 4^{th} layer the film was calcined between 600-900°C for 10 min. TiO_2 thin films were created with 8, 16, and 20 layers to determine the optimal thickness, however 16 layers was kept as the standard for most films. A flow chart and diagram of the Ti sol preparation and spin coating method is shown in Figure 2.7.

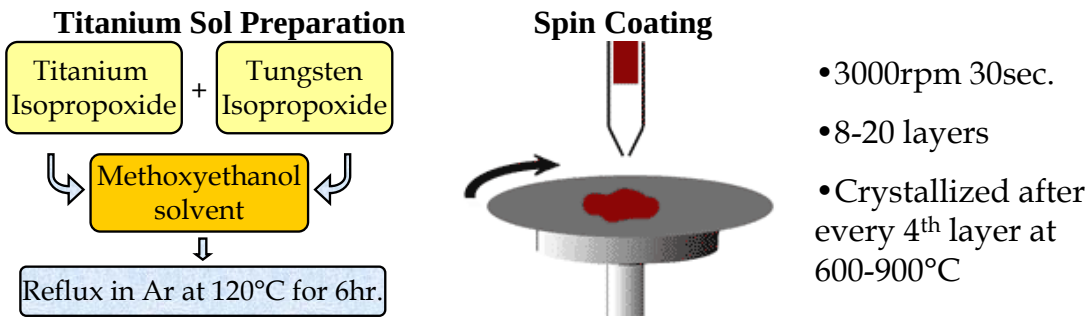

Figure 2.7. Flow chart and diagram of the Ti sol preparation and spin coating method for depositing thin films.

The films on alumina substrates were characterized for phase analysis and crystallite size using XRD. Approximate film thickness was measured by cross sectioning the substrates and film for analysis under FE-SEM. Film microstructure and grain size were also determined from FE-SEM images of the top surface.

Selected thin films (Pure 600°C, 800°C, 900°C, 10%W700°C, and 10%Ni900°C) were characterized in Dr. Jeanne McHales lab for ultraviolet visible (UV-VIS) light absorbance in air using a Shimadzu UV-2501 spectrometer with source wavelength of 300 to 800 nm and photoluminescence (PL) using an excitation wavelength of 350 nm as described in [Knorr '08]. Films were deposited on quartz substrates with the same processing procedure as the sensing films with 12 layers.

In order to measure temperature dependant resistance and gas sensing responses, films were placed in the same sensing measurement set-up described earlier. Operating temperature in the tube furnace was held controlled to various temperatures between 300 and 700°C and the resistance was allowed to stabilize for 24 h at each temperature before sensing measurements began. Baseline resistance was recorded before any gas response measurements were made. Gas response of the films was determined by changing the gas flow composition while measuring the dynamic film resistance.

Oxygen response was measured by reducing the oxygen content to 2 % balanced by nitrogen. Carbon monoxide and methane responses were measured by separately introducing 100 and 500 ppm of each target gas into the background flow of 10 % oxygen balanced by nitrogen as shown in Figure 2.8. Longer response (30 min) and recovery (60 min) times were allowed during the sensing tests due to a larger response of the thin films leading to slower response times. Duplicates of each film were fabricated and tested in the sensing chamber in order to verify results and gain knowledge of reproducibility. Standard deviations of these results are reported in the form of error bars to show differences between samples. Calculation of selectivity toward CO with respect to CH_4 is defined here as the ratio of responses to 500 ppm of each target gas shown in equation 10.

$$COSelectivity = \frac{CO^{500}}{CH_4{}^{500}} \tag{10}$$

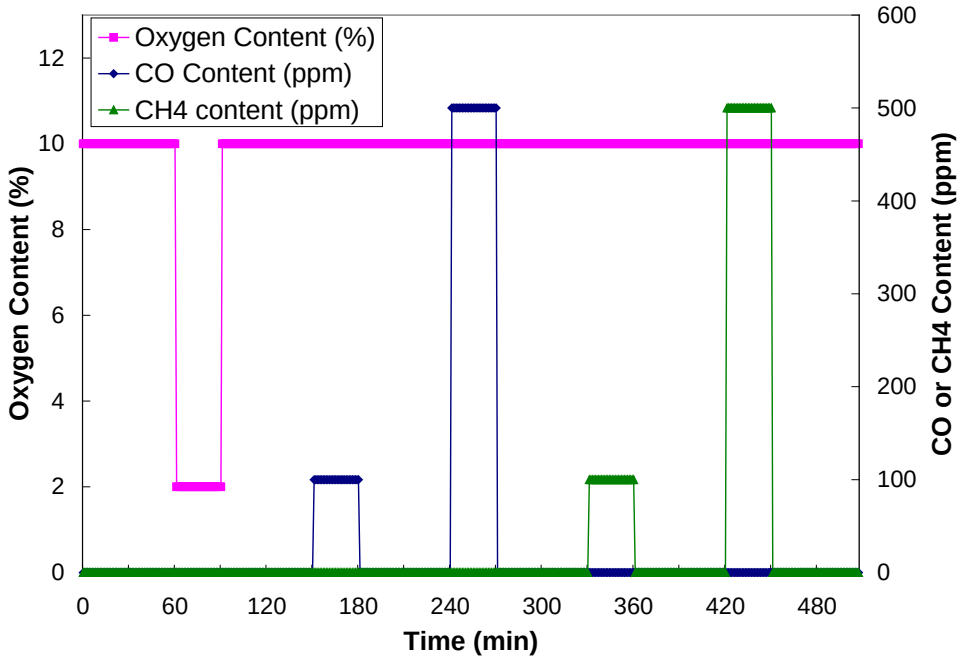

Figure 2.8. Sensing test gas concentrations and durations for measuring oxygen, carbon monoxide, and methane gas response. Target gasses were introduced to the sample for 30 minutes each followed by a 60 minute recovery with baseline gas composition.

2.6 Fabrication of Tungsten- and Nickel-Doped TiO_2 Thin Films

Tungsten- and nickel-doped TiO_2 thin films were fabricated and characterized using the same procedure as the pure TiO_2 thin films described earlier, with the slight alteration of including a tungsten and nickel source in the precursor solution. Tungsten (VI) isopropoxide ($W[OCH(CH_3)_2]_6$, Alfa Aesar), and nickel (II) methoxyethoxide ($Ni(OCH_2CH_2OCH_3)_2$, Alfa Aesar) were used as the dopant ionic sources. Sols were created with metal ion compositions of 0, 2.5, 5, 10 at.% W, and 10 at.% Ni balanced by Ti.

Example Calculations for making Ti sol with 5 at.%W and Metal Molarity of 0.5
Ti molarity in final solution (0.95)(0.5) = 0.475 mol/L
W molarity in final solution (0.05)(0.5) = 0.025 mol/L

Ti-isopropoxide molecular wt. = 284.22, density = 0.955 g/ml
W-isoporpoxide molecular wt. = 538.416, solution = 5 %w/v in isoproponal

Volume of Ti-isopropoxide for 100 ml total solution:
(284.22 g/mol)(0.475 mol/L)(0.1 L) = 13.5g /(0.955 g/ml) = **14.14 ml**

Volume of W-isopropoxide for 100 ml total solution:
(538.416 g/mol)(0.025 mol/L)(0.1 L) = 1.346 g /(0.05 g/ml) = **26.9 ml**

Volume of MOE for 100 ml total solution:
(100 ml) – (14.14 ml) – (26.9 ml) = **58.96 ml**

2.7 Fabrication of n-p Composite Thin Films

In order to characterize the influence of p-n homojunctions on the electrical and gas sensing properties of TiO_2 thin films, bilayer films of n-type W-doped TiO_2 and p-type Ni-doped TiO_2 were fabricated and characterized. For all the films dopant concentrations were kept constant at 10 at.% relative to Ti and all films contained 16 spin-coated layers total. Several variations of the n-p composite films were created and a schematic is shown in Figure 2.8:

1) 8 layers of Ni-doped TiO_2 calcined at 900°C followed by 8 layers of W-doped TiO_2 calcined at 700°C. This film is denoted '**Ni900W700**.'
2) 8layers of W-doped TiO_2 calcined at 900°C followed by 8 layers of Ni-doped TiO_2 calcined at 900°C, denoted '**W900Ni900**.'
3) To verify the effect of Ni, 8 layers pure TiO_2 calcined at 700°C followed by 8 layers of W-doped TiO2 calcined at 700°C, denoted '**P700W700**.' Note: This film is not an n-p composite but used to verify the effect of nickel as the bottom layer.
4) To verify the effect of W on the bottom layer, 8 layers pure TiO_2 calcined at 700°C followed by 8 layers of Ni-doped TiO_2 calcined at 900°C, denoted '**P700Ni900**'.
5) 14 layers of Ni-doped TiO_2 calcined at 900°C followed by 2 layers of W-doped TiO_2 calcined at 700°C, denoted '**Ni14W2**'.

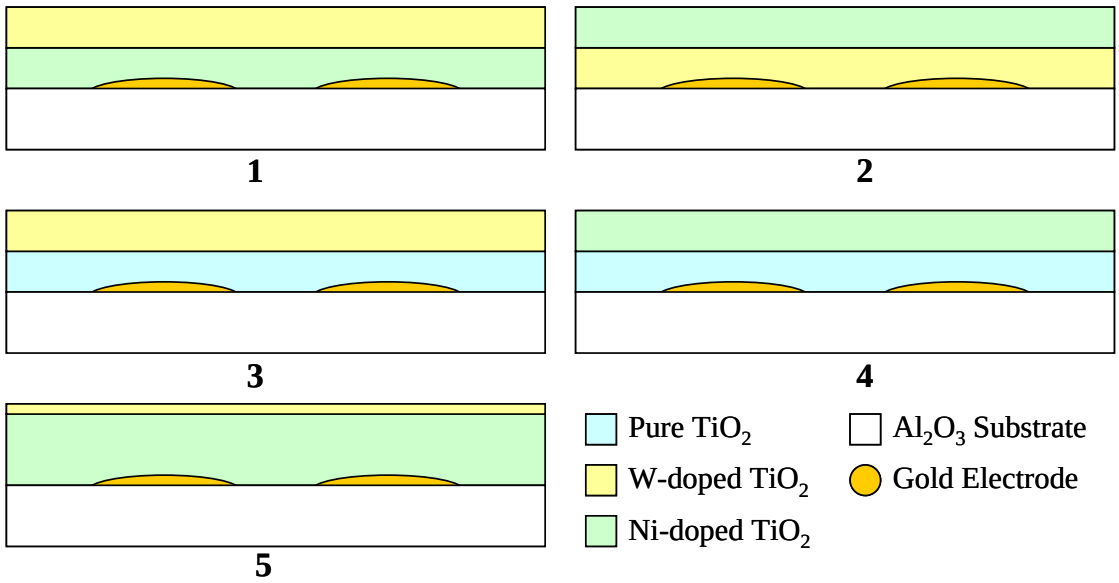

Figure 2.9. Schematic of the n-p composite thin films. Cross-sections of the films are diagramed showing the composition, order, and relative thickness of the bilayers.

To determine the elemental distributions and extent of diffusion of nickel and tungsten ions from one layer to the other, the Ni900W700 film was cross-sectioned and analyzed under FE-SEM equipped with a "Gensis EDAX" energy-dispersive spectrometer (EDS).

CHAPTER THREE

RESULTS

3.1 TiO_2 Thick Film Crystallinity

In order to investigate the role of TiO_2 crystallinity in thick film gas sensors we chose to synthesize our own TiO_2 nano-powder via the citrate-nitrate auto-combustion method. This method allowed us to control the crystallinity of the resulting TiO_2 nano-powder via the calcination temperature. To obtain TiO_2 nano-powder with tailored crystallinity, powder was calcined at 400, 500, 600,700,800, 900, and 1000°C for 1 hr.

Figure 3.1 shows the color of the calcined powder. The powder calcined at 400°C appears completely black in color signifying a significant amount of carbon present in the sample. By 500°C, the majority of the carbon has been calcined and the powder has turned to light grey color. At 600°C, only a slight hint of grey color is detectible, and by 700°C the powder is completely white, signifying calcination is complete. Complete calcination is necessary for crystallized TiO_2, and thermal stability during the sensing test at 600°C operation is desired, therefore we kept 700°C as our minimum calcination temperature for further studies.

Figure 3.2 and Table 3.1 show the XRD patterns and calculated crystallite sizes for TiO_2 powder calcined at 700, 800, 900, and 1000°C. JCPDS files 73-1764 and 87-0710 were used to identify anatase and rutile peaks, respectively. Nearly pure anatase phase was present up to 900°C. At 1000°C, anatase-to-rutile phase transformation had started and less than 20% anatase phase remained in the powder. Previous studies have concluded that rutile phase shows p-type sensing behavior [Savage ‘01], therefore, calcination temperatures were kept at or below 900°C in order to maintain pure anatase phase.

Figure 3.1. Photograph of the calcined TiO_2 nano-powder showing the color varying from black to white.

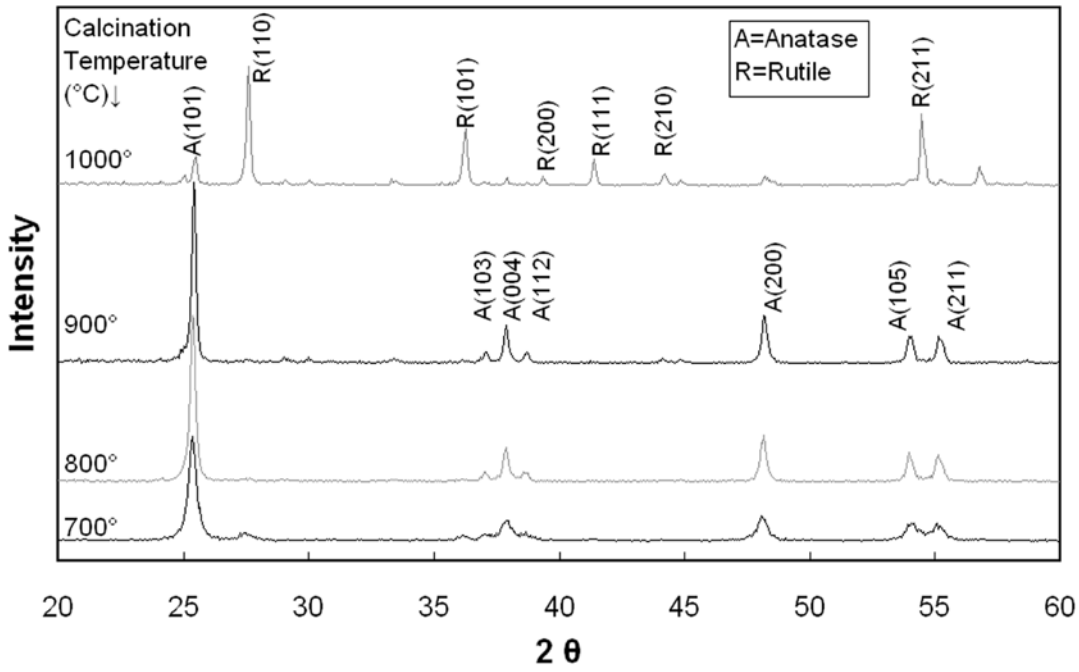

Figure 3.2. X-ray diffraction patterns for TiO_2 powder calcined at 700, 800, 900, and 1000°C for 1 hr.

Figure 3.3 shows TEM micrographs of TiO_2 powder calcined at 700, 800, and 900°C.

The increase in particle size with calcination temperature can easily be seen. Average particle

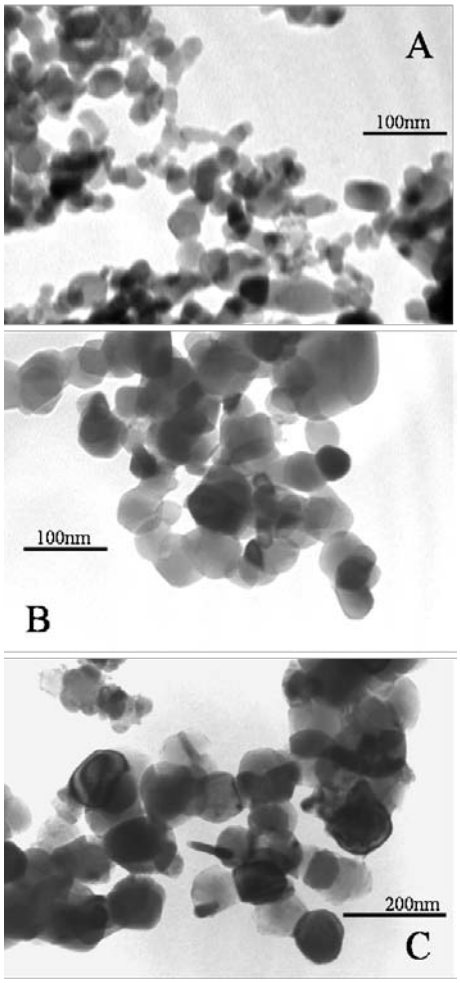

Figure 3.3. TEM micrographs of TiO_2 powder calcined at 700°C (A), 800°C (B), and 900°C (C).

size for powder calcined at 700°C was 21nm, 800°C averaged to 58nm, and 900°C averaged to 106nm respectively. These values are sumarized in Table 3.1.

Figure 3.4 shows the BET specific average surface area values for powder calcined between 500 and 900°C. Increase in calcination temperature caused the particle size to increase, which corresponded to a decrease in specific surface area. BET values were used to calculate an estimate of particle size, assuming spherical, non-porous particles and an anatase density of 3.9 g/cm^3; results are summarized in Table 3.1.

A summary of crystallite (from XRD) and particle size (from TEM and BET) as a function of calcination temperature is given in Figure 3.5 and Table 3.1. Crystallites are refering to an individual crystal grain, and particles are refering to the individual pieces that make up the ceramic powder. Particles are usually made up of more than one crystallite. Therefore, estimates of particle size and crystallite size were calculated using BET surface area and XRD studies, respectively. These two methods represent theoretical upper and lower limits, respectively, for the actual average particle size. TEM particle size lies within these two limits. These results confirm that even though anatase phase was stable below 900°C, crystallite and particle size both increased with increasing calcination temperature.

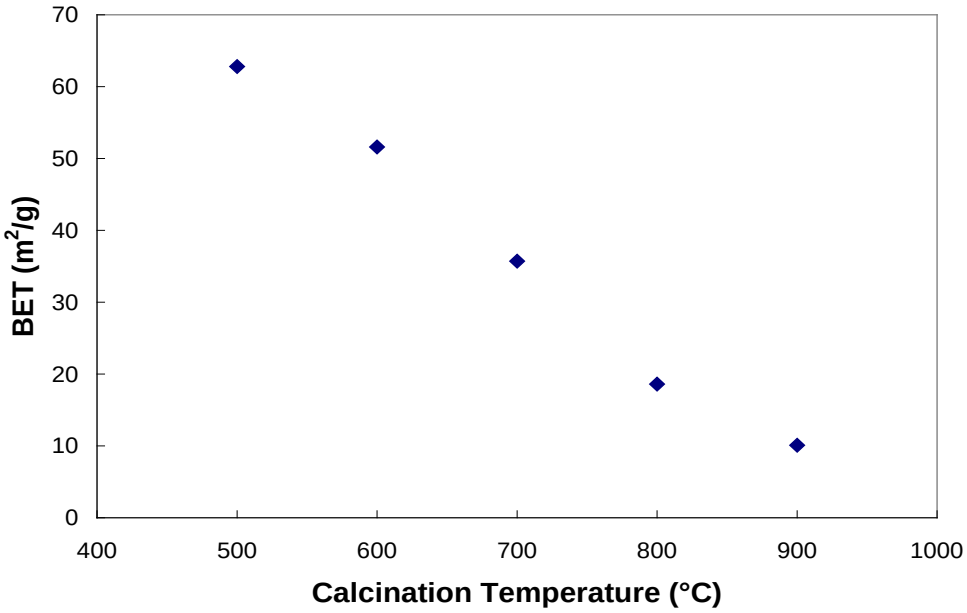

Figure 3.4. BET specific average surface area values for TiO_2 powder calcined at various temperatures for 1 hr.

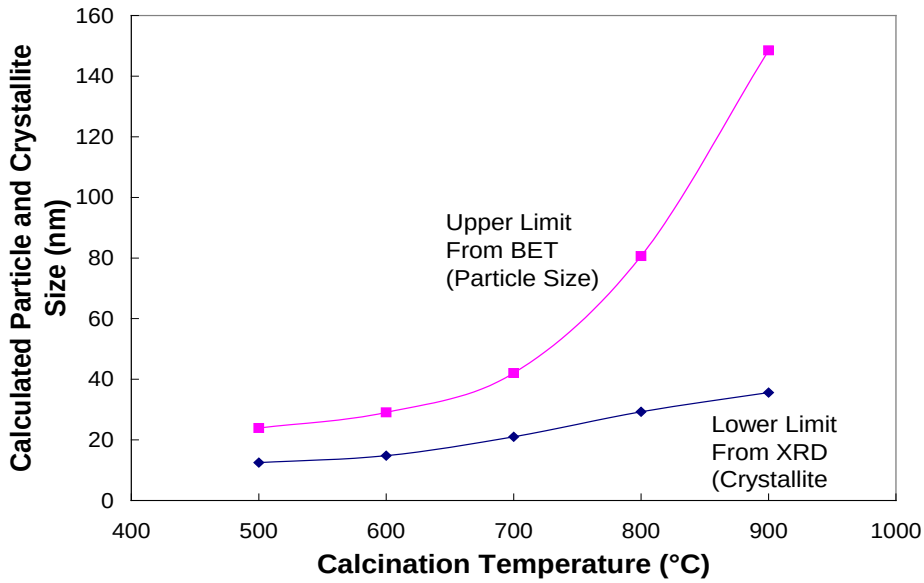

Figure 3.5. Calculated crystallite (from XRD) and particle size (from BET) as a function of calcination temperature.

Figure 3.6 displays the DSC profiles for powder calcined at 700, 800, and 900°C. The exothermic peak around 1100°C which all three profiles contain is attributed to the anatase-to-rutile transformation, and the exothermic shoulder around 900°C is caused by the amorphous to

Table 3.1. Crystallite size, BET surface area, and particle size for TiO_2 powder calcined at 700, 800, 900, and 1000°C for 1 hr.

Calcination Temperature (°C)	Crystallite Size calculated from XRD (nm)	BET Specific Average Surface Area (m^2/g)	Particle Size estimated from BET (nm)	Particle Size Calculated from TEM (nm)
700	21.0	35.7 ±0.9	42.0 ±1	21 ± 6
800	29.3	18.6 ±0.4	80.6 ±2	58 ± 28
900	35.6	10.1 ±0.2	148.5 ±3	106 ± 21
1000	39.5	3.9 ±0.1	384.6 ±10	-

crystalline anatase phase transformation [Yoganarasimhan '62, Stojanovic '00]. Peak areas of this anatase formation shoulder were found by estimating where the shoulder began and ended relative to the exothermic background, then using Origin software to calculate the area below the curve and above a linear interpolation of the baseline (see insert in Figure 3.6). The stored energy values found from the peak area of this shoulder at 900°C diminished with increasing calcination temperature from 11.2 μV/mg at 700°C to 7.1 μV/mg at 800°C, and almost nonexistant (1.5 μV/mg) for 900°C calcined powder. This calculation was performed to show

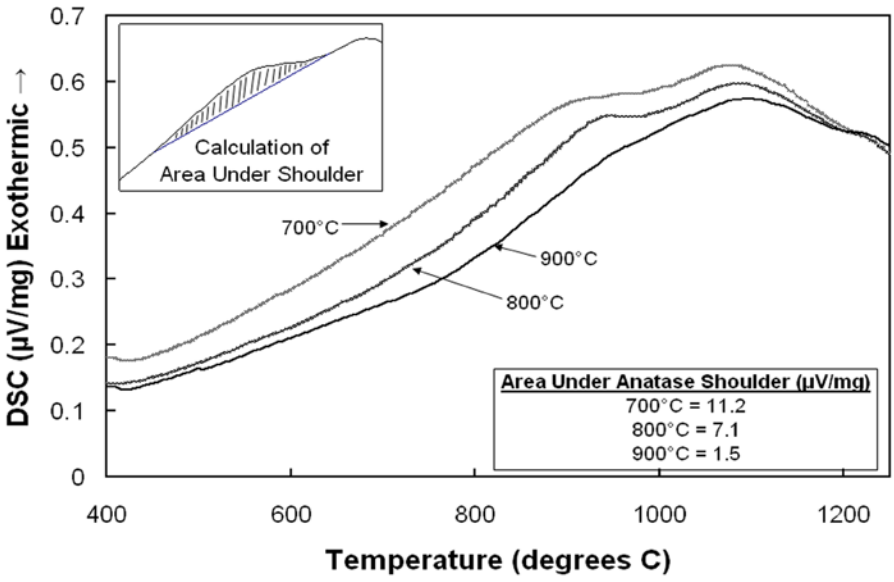

Figure 3.6. Differential scanning calorimetry profiles for TiO_2 powder calcined at 700, 800, and 900°C for 1 hr.

that the area of this peak shoulder decreased with increasing calcination temperature. This diminishing exothermic energy suggested that there was less amorphous content in the 900°C calcined powder than that in the 700°C calcined powder. This result supports the intuitive idea that crystallinity of the powder increased with increasing calcination temperature, which created a higher degree of atomic order in the TiO_2 nanoparticles.

From analysis of the nano-powder calcined between 700 and 900°C, it is clear that, while no rutile had formed, between these temperatures the anatase phase was crystalizing from the amorphous phase and leading to larger crystallites and particles and lower surface area.

Figure 3.7 shows the microstructure of the sintered thick film sensing elements. Films were calcined at 700 or 800°C and then sintered at 700 or 800°C. Both calcination temperature as well as sintering temperature can be seen to have the same effect on the resulting particle size. The film calcined and sintered both at 800°C showed the largest particle size (130nm) while the film calcined and sintered both at 700°C showed the smallest particle size (50nm). A Student's t-test on particle size yielded a p-value less than 0.01, suggesting a statistical difference in particle size between the films. Comparing the films both calcined at 800°C, the film sintered at 800°C showed a noticibly larger particle size than the film sintered at 700°C. This result suggests that particle size continued to grow during the sintering step and the amount of growth was dependent on the temperature. Increased sintering temperature also had an effect on the microstructure of the film; increasing both pore size and degree of connectivity between particles.

Thick film resistances at 600°C in the baseline gas composition of 10 $\%O_2$ balanced by nitrogen ranged from 3.7 to 5.3 MΩ and did not significantly correlate with film processing parameters. Thick film response to CO concentration while operating at 600°C is shown in Figure 3.8. Response (R_g/R_o) was defined as the ratio of resistances with (R_g) and without (R_o)

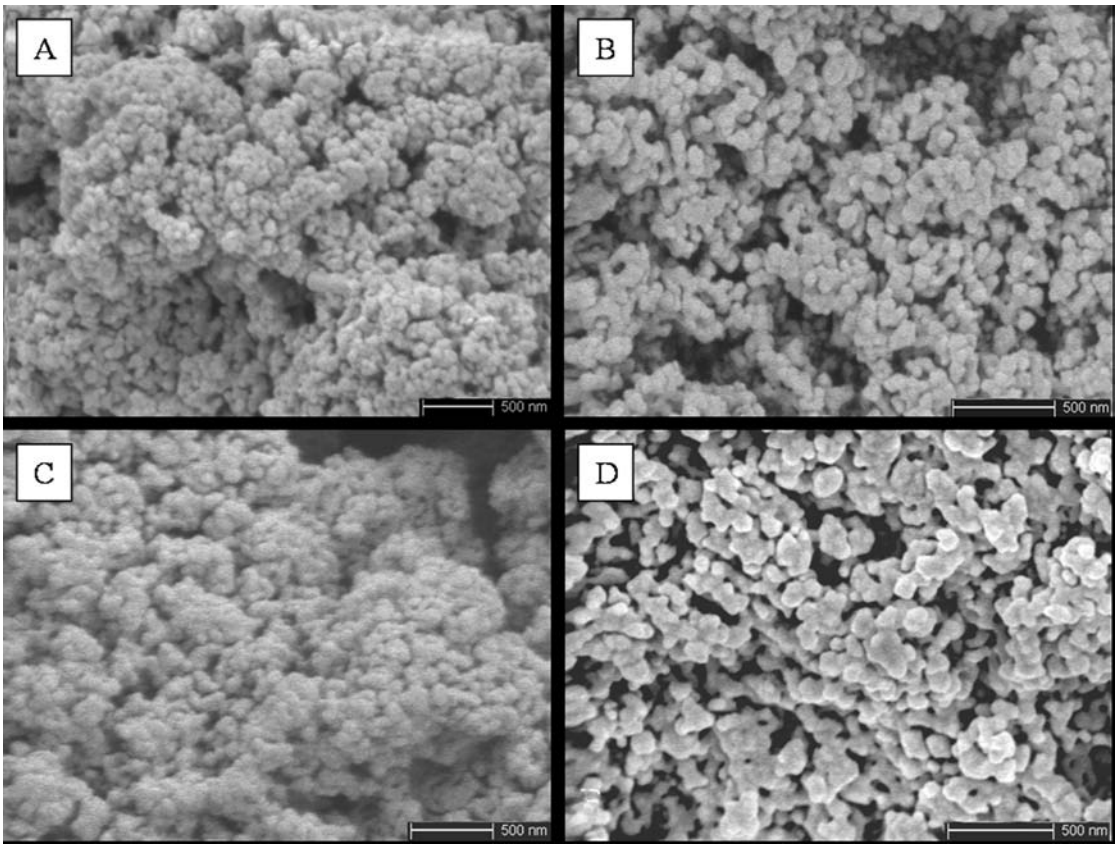

Figure 3.7. FE-SEM micrographs of the sintered TiO_2 thick film sensing elements calcined (C) and sintered (S) at 700 or 800°C. e.g. sample C700-S800 was calcined at 700°C and sintered at 800°C. (A) Film C700-S700, (B) C800-S700, (C) C700-S800, and (D) C800-S800. Scale bars are 500nm.

the presence of the target gas carbon monoxide with a constant 10 $\%O_2$ ballanced by nitrogen carrier gas. Powder calcination and element sintering temperatures are shown for each profile in which calcination temperature is reported first followed by sintering temperature (e.g. calcination at 800°C and sintering at 700°C is shown as "C800-S700"). The time taken for the sensors to respond to 90% of their maximum value was between 20 to 30 seconds regardless of processing conditions. Similarly, the 90% recovery times for all samples were between 70 to 150 seconds. The C800-S800 films showed the best response with a value of 0.74 at 500ppm CO, which is comparable to other reported values in similar conditions [Akbar '06]. Interestingly, C700-S700 film with the highest surface area showed the lowest response, which was not intuitive. A closer

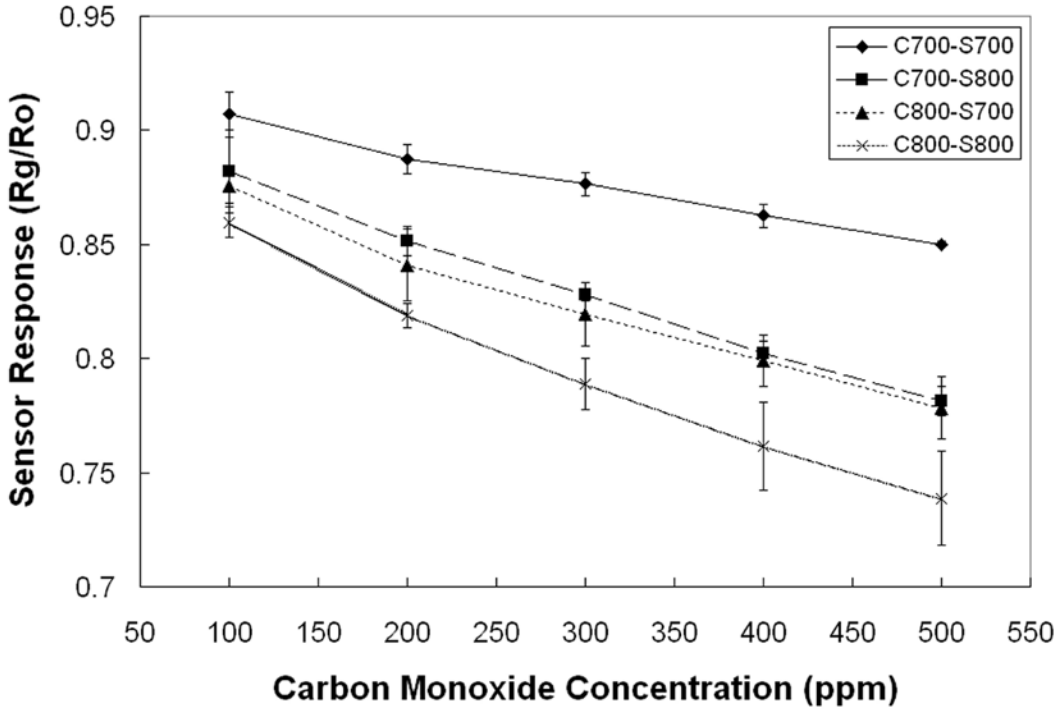

Figure 3.8. Sensing response to carbon monoxide for TiO_2 thick films calcined (C) and sintered (S) at 700 or 800°C. e.g. sample C700-S800 was calcined at 700°C and sintered at 800°C. Response was measured in a constant background gas of 10%O_2 balanced by nitrogen with a constant operating temperature of 600°C.

look at the data clearly shows that it is not just the surface area of the powder, but the crystallinity of the material, which plays a key role determining the sensitivity towards gas sensing. Sensor elements made with 900°C calcined powder and sintered at 900°C showed degredation in response, with a value of 0.89 at 500ppm carbon monoxide. This data is not incorporated in the results for simplicity of Figure 3.8.

A significant improvement in response was seen from film C700-S700 to film C800-S700, which shows that the higher calcination temperature improved the sensing response. A similar comparison between films C700-S800 and C800-S800 shows agreement with this conclusion. Higher sintering temperature was also seen to improve sensing response by comparing films C700-S700 with C700-S800, and C800-S700 with C800-S800. Heat treatment

temperatures at 900°C caused the response to degrade, possibly due to significant particle growth and surface area reduction. From this data it is obvious that 800°C was found to be the optimum temperature for both calcination and sintering of synthesized TiO_2 carbon monoxide gas sensors.

3.2 TiO_2 Thick Film Chemistry

Engineering the chemical composition of TiO_2 sensors has proven to be a useful method to improve many of the sensing properties such as sensitivity, selectivity, and stability. We have previously found the addition of aluminum (Al) and yttrium (Y) to TiO_2 have significant impact on the crystallization and electrical properties of TiO_2 thick films [Choi '07, Seeley '09]. To further investigate the effects of altering the TiO_2 chemistry, we chose to study the addition of tungsten (W) on the sensing properties of our thick films sensing elements.

Tungsten oxide (WO_3) nano-powder was added to commercial TiO_2 nano-powder in amounts of 0, 1, and 5 wt.%. Powder was then heat-treated at temperatures of 900, 950, and 1000°C. Sample abbreviations are given with tungsten amount followed by the calcination temperature, i.e. the 1%WO_3 sample heated to 950°C is denoted as "1W950." Figure 3.9 shows the XRD patterns of pure and W-doped TiO_2 calcined between 900 and 1000°C for 1 h. Analysis of pure and W-doped TiO_2 nano-powder revealed that anatase phase (JCPDS# 73-1764) was the only crystalline phase present in all compositions up to 900°C. A comparison of the anatase peak height revealed that the amount of anatase diminishes with increasing tungsten content. This result suggested that addition of tungsten retards anatase formation in TiO_2 at 900°C. FWHM values for the anatase (101) peak for samples calcined at 900°C were measured to be: 0.22° for pure TiO_2, 0.235° for 1W, and 0.281° for the 5W sample. Using the Scherrer equation [Cullity '78], these values corresponded to crystallite sizes of 37, 34, and 29nm,

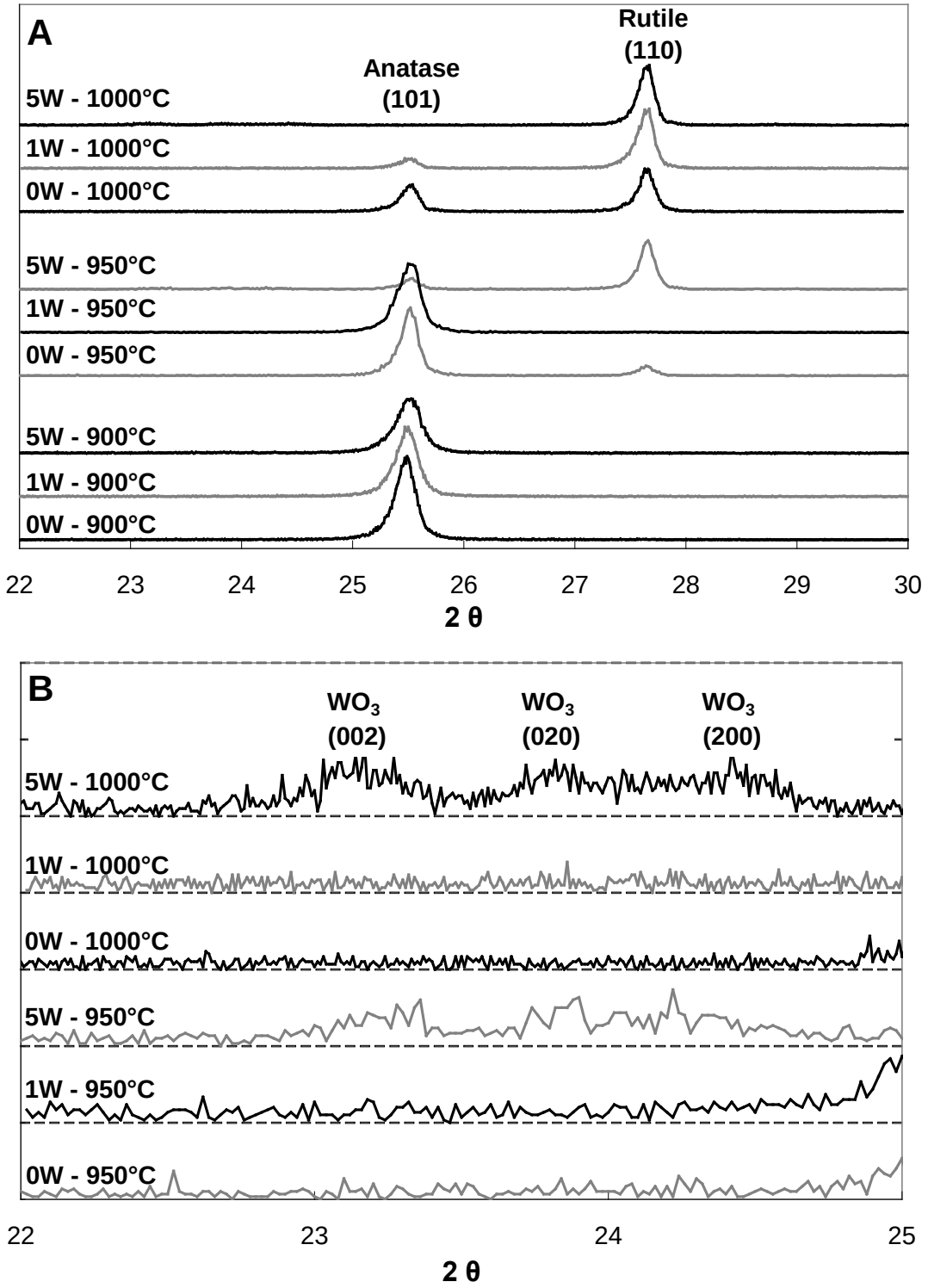

Figure 3.9. X-ray diffraction patterns for pure and W-doped TiO_2 powder calcined between 900 and 1000°C. (A) Scan over angles containing both 100% anatase peak and 100% rutile peak, and (B) close up of the 100% WO_3 peaks.

respectively; further indicating that addition of tungsten inhibits anatase crystallite formation.

Differential scanning calorimetry (DSC) patterns for pure and W-doped TiO_2 powder calcined at 800°C are shown in Figure 3.10. Each profile contains two overlapping exothermic peaks: the first attributed to the crystallization from amorphous to anatase phase, and the second at higher temperature is due to the anatase-to-rutile phase transformation [Yoganarasimhan '62, Stojanovic '00, Xie '02]. The two aforementioned peaks are deconvoluted by fitting two gaussian curves, as shown in Figure 3.10. In order to present the onset temperature of these phase transformations [Bandyopadhyay '95], the first derivitave was used to determine the inflection point of each gaussian curve. These values indicate the point of maximum increase in exothermic energy given off by the sample and represent the temperature at which phase transformation was starting. Table 3.2 summarizes the peak areas for crystallization energy and inflection point temperatures. The anatase crystallization peak areas and intensities increase with increasing tungsten concentration. This signifies that, with addition of tungsten, more

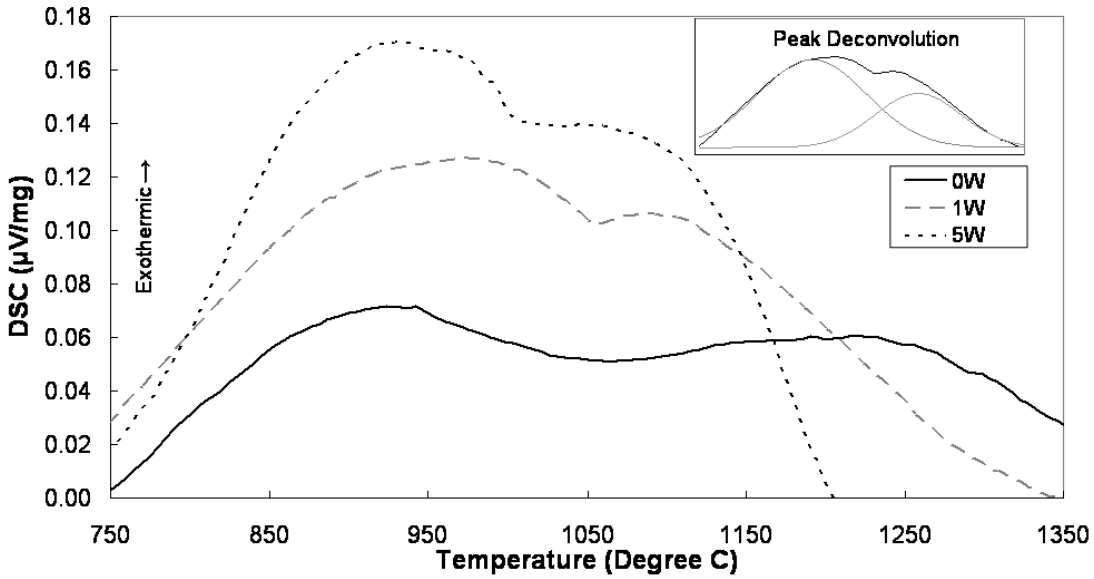

Figure 3.10. DSC on pure and W-doped TiO_2 powder calcined at 800°C.

amorphous material is present in the powder after calcination at 800°C. This amorphous material then crystallizes during the DSC scan with an exothermic release of energy [Xie '02]. The anatase crystallization inflection point temperature for the 0W and 1W samples was observed at a lower temperature of 819°C compared to the 5W sample at 837°C. This result revealed that there is a slight delay in anatase crystallization in the 5W sample during heating.

Table 3.2. DSC peak area and inflection of anatase and rutile formation peaks for pure and W-doped TiO_2 powder calcined at 800°C.

Composition	**Pure TiO_2**	**TiO_2-1%WO_3**	**TiO_2-5%WO_3**
Amorphous to Anatase Crystallization Peak Area (μV°C/mg)	18	45	46
Amorphous to Anatase Crystallization Peak Inflection (°C)	819	819	837
Anatase to Rutile Phase Transformation Peak Area (μV°C/mg)	26	17	23
Anatase to Rutile Phase Transformation Peak Inflection (°C)	1057	1049	1038

Powder calcined at 800°C showed specific surface area values of 28, 31, and 39 m^2/g for 0, 1, and 5% WO_3 in TiO_2, respectively. At these lower temperatures, tungsten delayed anatase phase formation, leading to smaller crystallite and particle sizes. In agreement with XRD and DSC results, we conclude that the presence of tungsten delayed the crystallization process at temperatures below 900°C.

During calcination at 950°C rutile phase (JCPDS# 87-0710) started to form in the pure TiO_2, however no rutile phase was found in the 1W sample, indicating that this small amount of tungsten helped in stabilizing the anatase phase. However, the 5W sample calcined at 950°C contained a significant amount of rutile phase along with slight emergence of WO_3 monoclinic crystalline phase (JCPDS# 72-0677) as seen in Figure 3.9B. These results suggest that under the current solids state reaction conditions, 5 wt. % WO_3 is not able to completely dissolve into the TiO_2 lattice, leaving behind the secondary monoclinic phase. This result is in agreement with S.

Komorinicki et al. [Komornicki '04] who reported the solubility limit of WO_3 in TiO_2 to be 0.4 mol % (1.15 wt. %) after which the monoclinic phase starts to emerge.

Powder calcined at 950°C showed BET surface area values of 8, 11 and 6 m^2/g for 0, 1 and 5% WO_3, respectively. At this intermediate temperature, 1% WO_3 is effective at stabilizing the anatase phase and hindering grain growth, however 5% WO_3 promotes rutile phase formation and larger particles lowering the surface area. These results agree with XRD analysis.

XRD patterns for powder calcined at 1000°C showed rutile as the majority phase of each composition. A reduction in the anatase peak height relative to the rutile peak height was observed with increasing tungsten content. At this temperature, 1 % WO_3 was no longer able to stabilize the anatase phase. The 5W sample showed complete TiO_2 phase transformation from anatase-to-rutile, along with more defined WO_3 monoclinic peaks further indicating that this secondary phase supports rutile formation. Calcination at 1050°C resulted in 100% rutile phase in all powder compositions.

From the DSC scan in Figure 3.10, anatase-to-rutile phase transformation peak inflection points are seen to shift to significantly lower temperatures with increasing tungsten concentration, as summarized in Table 3.2. Again, this result is consistent with XRD data suggesting that, at 1000°C, rutile is more likely to form in TiO_2 samples with higher tungsten concentration.

From the XRD, BET, and DSC analysis of the heat-treated W-doped TiO_2 nano-powder, it is clear that 1 wt.% WO_3 is able to inhibit anatase and rutile crystallization up to 950°C, while 5 wt.% WO_3 actually promotes crystallization of these two phases at lower temperatures compared with pure TiO_2. We found these results on crystallization to have a similar correlation with the gas sensing properties as described earlier for pure TiO_2 crystallization; however here, it

is the tungsten content which is controlling the crystallinity of the TiO_2 rather than only the calcination temperature.

Baseline resistance in the background gas environment before introducing carbon monoxide ranges from 1 to 7 MΩ depending on the calcination temperature and tungsten concentration. Similar to previous studies, baseline resistance of pure TiO_2 films are higher than W-doped TiO_2 films calcined at the same temperature [Wisitoraat '05]. Lower resistance with addition of tungsten is explained by the additional electrons generated by substitutional defects according to equation (11):

$$TiO_2 \rightarrow W^{6+}_{Ti4+}{}^{\cdot\cdot} + 2O_O{}^{x} + 2e^{-} \qquad (11)$$

We have previously reported that crystallization in TiO_2 sensors can significantly alter the gas sensing performance [Seeley '09]. Addition of tungsten into TiO_2 alters the anatase crystallization process and the anatase-to-rutile phase transformation temperature. Change in the degree of crystallization caused by addition of tungsten influences the sensing response toward carbon monoxide (CO). Gas response toward 500 ppm CO for pure and W-doped TiO_2 thick

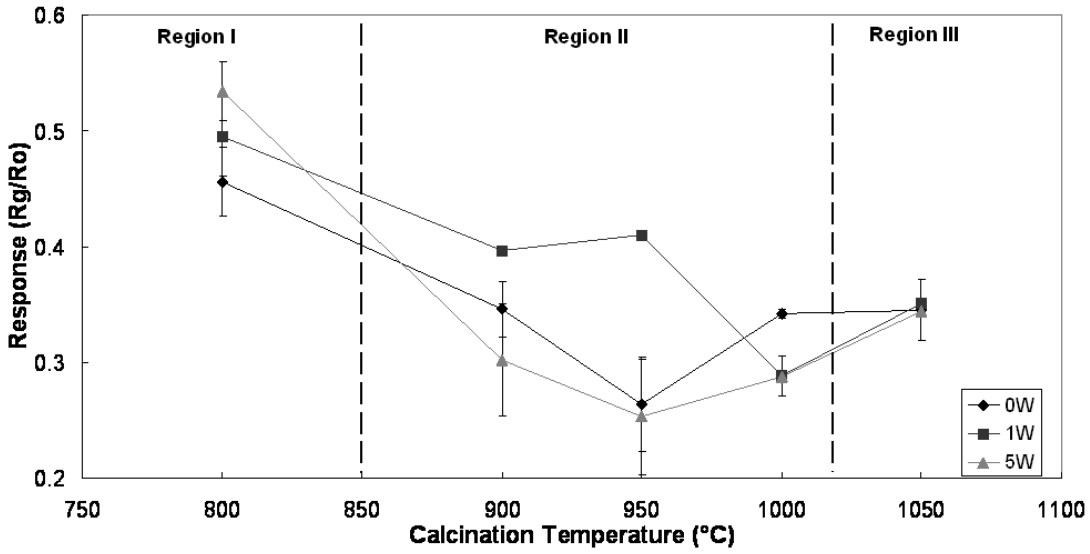

Figure 3.11. Response to 500ppm CO for pure and W-doped TiO_2 films calcined between 800 and 1050°C.

films calcined between 800 and 1050°C are shown in Figure 3.11. Response of the sensors is found to coorelate strongly with crystalline phases present in the sample. For this reason, the graph is divided into 3 regions according to low, medium, and high calcination temperatures.

In region I in Figure 3.11, which presents the calcination temperature below 850°C, all samples show poor gas response. According to XRD and DSC results, this temperature is not sufficient to completely crystallize the TiO_2 into anatase structure. There is a significant amount of amorphous phase present in the films which we have shown to inhibit the gas sensing mechanism. This significant amorphous content results in pure and W-doped films that display poor gas response.

Region II in Figure 3.11, which corresponds to calcination temperatures between 900 and 1000°C, shows the best gas response. In this temperature range crystallization to anatase phase is accomplished for 0W and 5W samples along with minimal phase transformation to rutile. However, in the case of 1W sample, the anatase crystallization is delayed at these temperatures. The influence of crystallization and phase transformation on gas response is clearly noticed for W-doped TiO_2 thick film samples. Response of 0W and 5W samples improves with increasing calcination temperature up to 950°C, while the 1W sample response improves more slowly with increasing calcination temperature. At 1000°C calcination temperature, the 1W sample catches up in the crystallization process and the gas response improves accordingly. However, at this temperature, the major fraction of the material is transformed to rutile phase for all the compositions, causing the gas response to degrade.

Region III in Figure 3.11 coresponds to calcination temperatures above 1000°C where all three compositions are fully transformed to rutile. Under these conditions, addition of tungsten has no effect on the TiO_2 phases present and therefore no effect on gas response. At these high

temperatures a significant reduction in surface area has occurred which, along with rutile phase formation, causes the degradation in gas response.

3.3 Pure TiO_2 Thin Films

Thin films of TiO_2 have previously been fabricated in our lab, however this is the first time films were created on a rough alumina substrate for gas sensing purposes. Therefore, much optimization of film processing parameters was necessary prior to performing a controlled study of the thin film material properties on sensing response.

DSC and TGA profiles for the precursor Ti-based metal-organic solution are shown in Figure 3.12. The endothermic peak at 110°C corresponding to a large weight loss is due to evaporation of excess solvent. The three exothermic peaks seen at 270, 390, and 500°C corresponding to small weight losses are due to calcination of the organic constituents in the

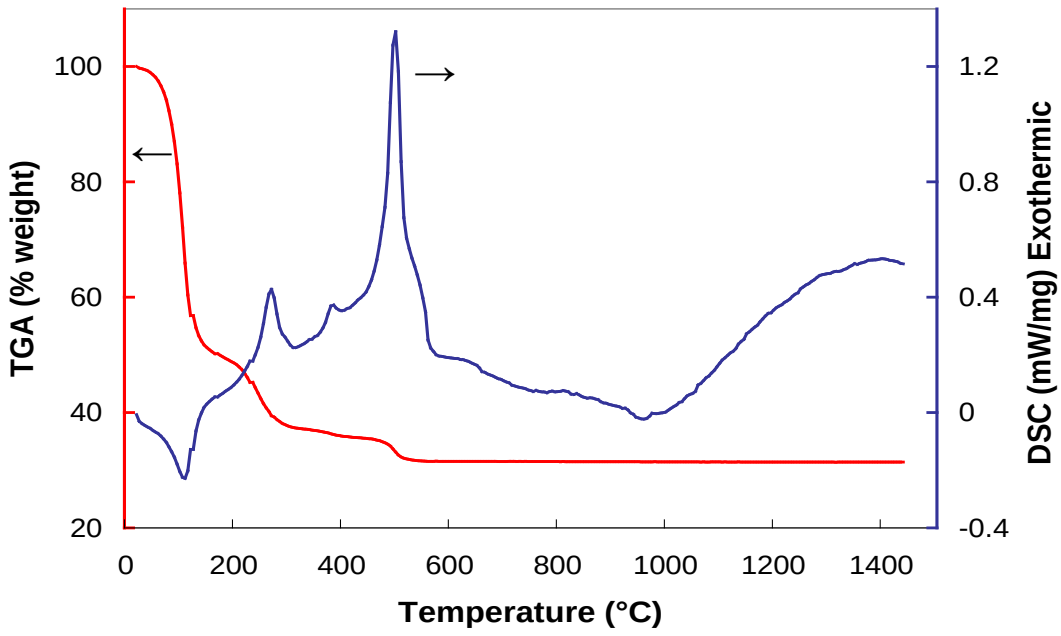

Figure 3.12. Thermogravimetric analysis and differential scanning calorimetry profiles for titanium isopropoxide in methoxyethanol precursor solution after refluxing at 120°C.

precursor. Above 550°C, no additional weigh loss is observed, indicating that calcination is complete; however, two exothermic shoulders at 650 and 850°C remain in the DSC profile. These shoulders are attributed to the crystallization of anatase TiO_2 and anatase-to-rutile transformation, respectively. Lastly, the large exothermic peak above 1000°C corresponds to grain growth, sintering, and densification in the TiO_2.

Thin films were deposited by spin coating the metal-organic sol onto the alumina substrates, followed by a calcination/crystallization heat treatment. The resulting films were not obvious by the naked eye, therefore in order to verify the presence of the films, Figure 3.13

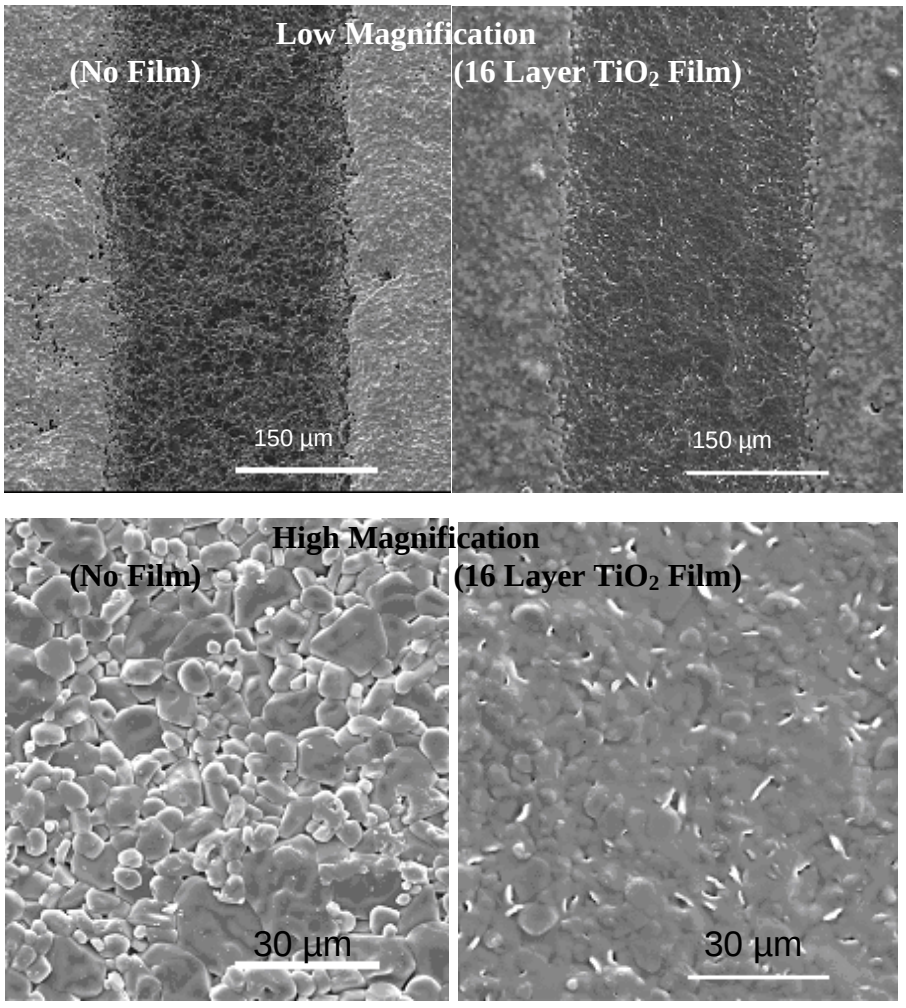

Figure 3.13 SEM images of the alumina substrate top surface with and without the presence of a thin 16 layer TiO_2 film calcined at 700°C.

shows low magnification SEM images of the top surface of the substrate with and without the film present. The presence of a 16 layer TiO_2 thin film on the substrate was observed by the blurring of the alumina grains; however, in order to characterize the structure of the film, higher magnification FE-SEM images were needed and will be discussed later.

We had previously found that the processing conditions used to create thin films via a sol-gel layer-by-layer spin coating method formed films approximately 70-80 nm per layer with a solution of metal ionic concentration of 0.5 molar [Myers '02, Akasheh '04]. In this work, TiO_2 thin films were created with 8, 16, and 20 layers to determine the optimal thickness for gas sensing. Baseline resistance and the carbon monoxide response for these films calcined at 700°C and operating at 600°C is shown in Figure 3.14.

From the plot of baseline resistance for thin films with 8, 16, and 20 layers, it is clear that the resistance, as well as the standard deviation between films, decreases with increasing number of layers. This suggests that 8 layers are not sufficient to form a uniform film across the substrate. This analysis is supported by the carbon monoxide gas response improving with increasing number of layers. From these results, it is concluded that 8 layers are insufficient in producing a complete and uniform film on the alumina substrate, however, by 16 layers, the gas response appears to be saturating. Increasing the number of layers decreases the surface-to-bulk ratio, as well as increases the chance for film cracking and spalling problems; therefore the number of layers should be kept to a minimum. From these two extremes, a total of 16 layers was chosen as the standard thickness for further studies.

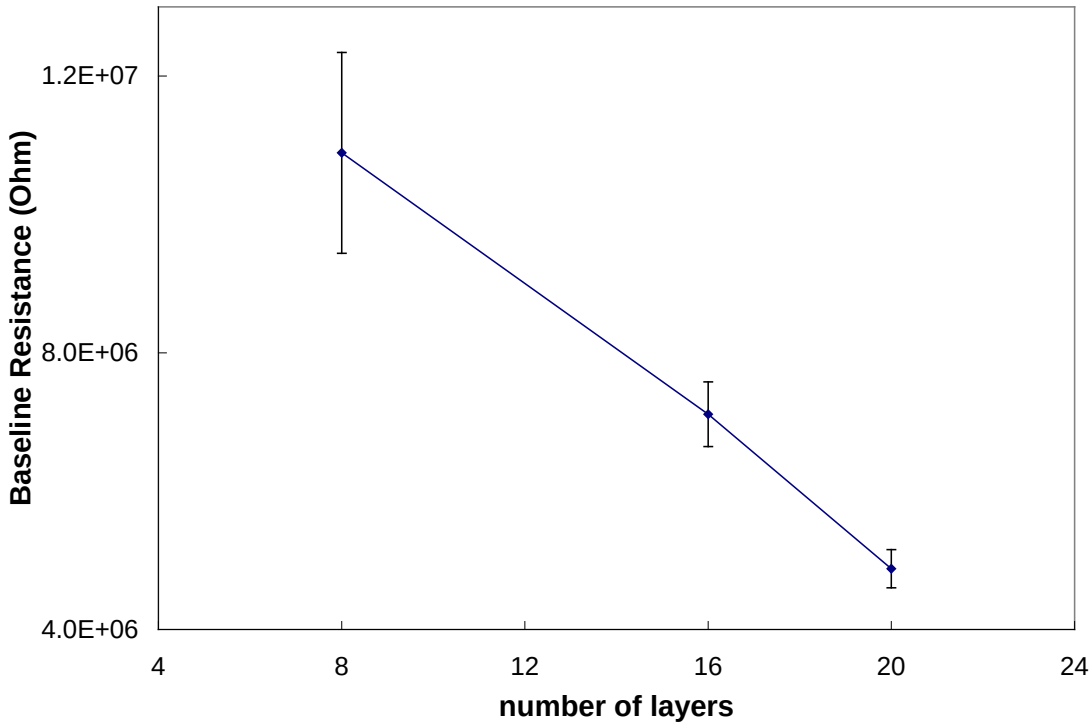

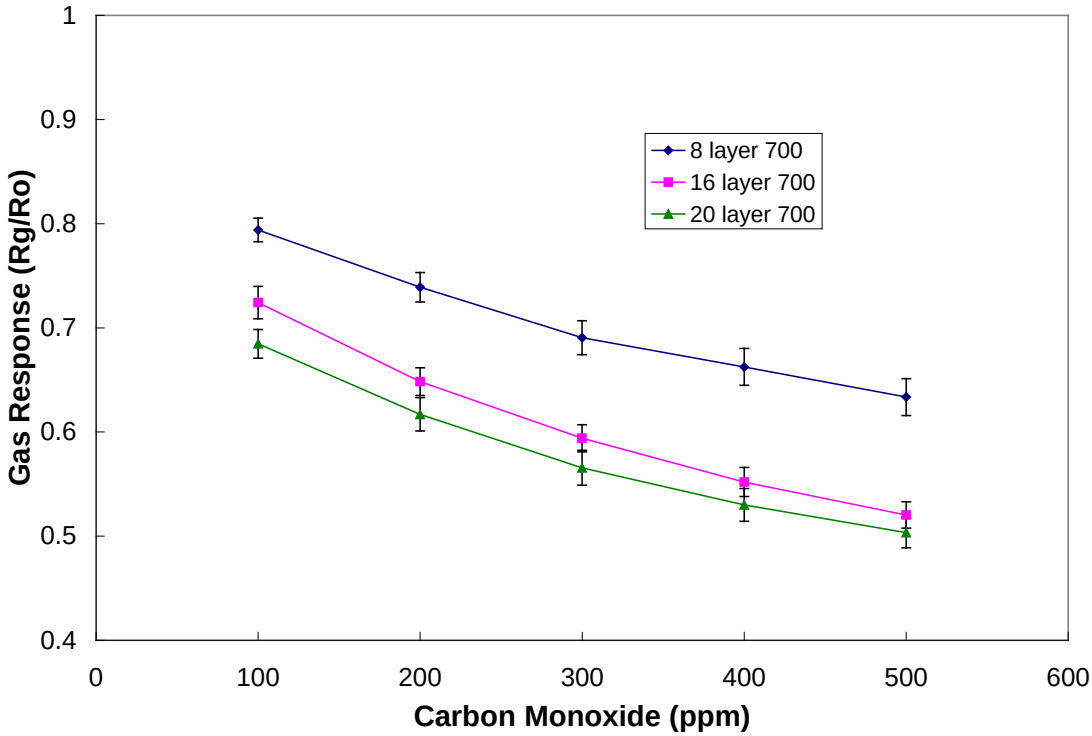

Figure 3.14. Baseline resistance and Carbon monoxide gas response for pure TiO_2 thin films created with 8, 16, and 20 layers operating at 600°C.

Figure 3.15 shows the effect of calcination time on the thin film gas response. It is clearly seen that an extended calcination time from 10 to 50 minutes degraded the gas response. It is hypothesized that the extended time lead to excessive grain growth and possibly film cracking or diffusion from the alumina substrate. For these reasons, 10 minutes was kept as the standard calcination time for further studies.

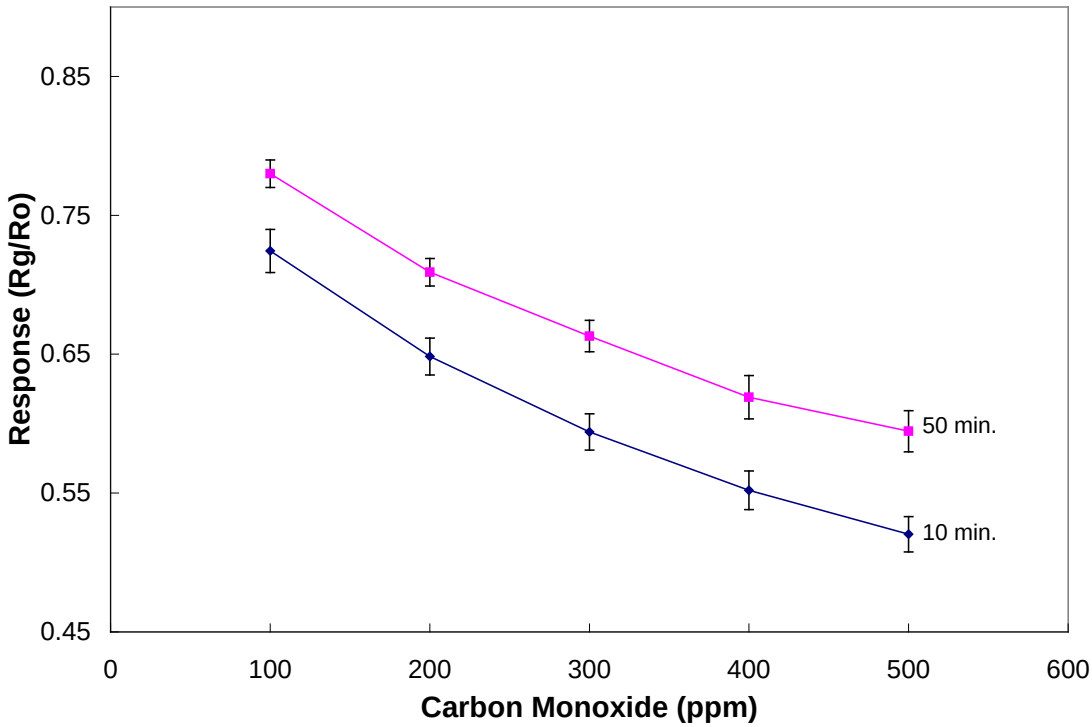

Figure 3.15. Effect of calcination time (10 minutes or 50 minutes) on the CO gas response for 16 layer TiO_2 thin films calcined at 700°C and operating at 600°C.

Figure 3.16 shows a comparison between synthesized thick and thin films both calcined at 700°C. Thin films showed a large improvement in CO gas response compared with thick TiO_2 films made from similar processing conditions. This improvement is attributed to the high surface area-to-volume ratio of thin films resulting in large reactivity to the target gas. This high gas sensitivity resulted in the remaining studies of this thesis, focusing on the material and sensing properties of thin films.

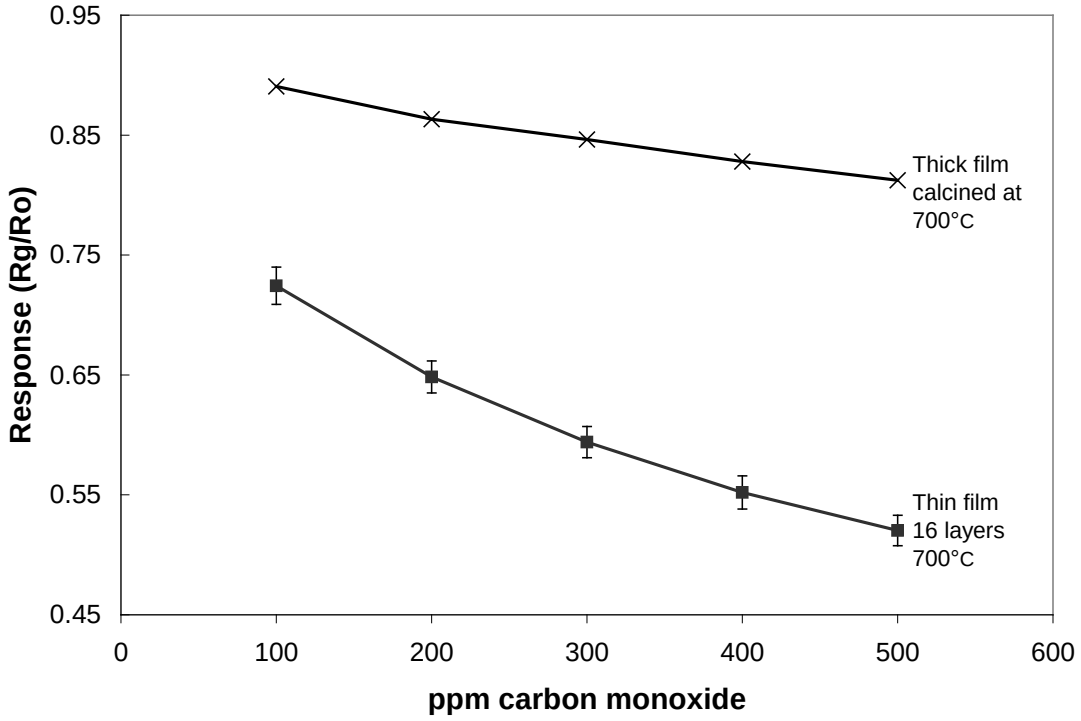

Figure 3.16. Comparison of CO gas response between synthesized thick and thin TiO_2 films both calcined at 700°C and operated at 600°C.

In order to measure the thickness of the thick and thin films, the substrates were mounted in epoxy resin, cross-sectioned, and polished. SEM images were then taken of the film cross-sections and used to quantify the thickness of the various films. Figure 3.17 shows the SEM images of the cross-sectioned thick and thin films. Due to the roughness of the alumina substrate, the thin film was also deposited on a smooth silicon wafer which gave a better picture of the film thickness. From these images, the thick film appears to be approximately 30 μm thick and the thin films are approximately 1 μm thick. This confirms that each sol-gel layer is creating a TiO_2 layer approximately 70 nm thick.

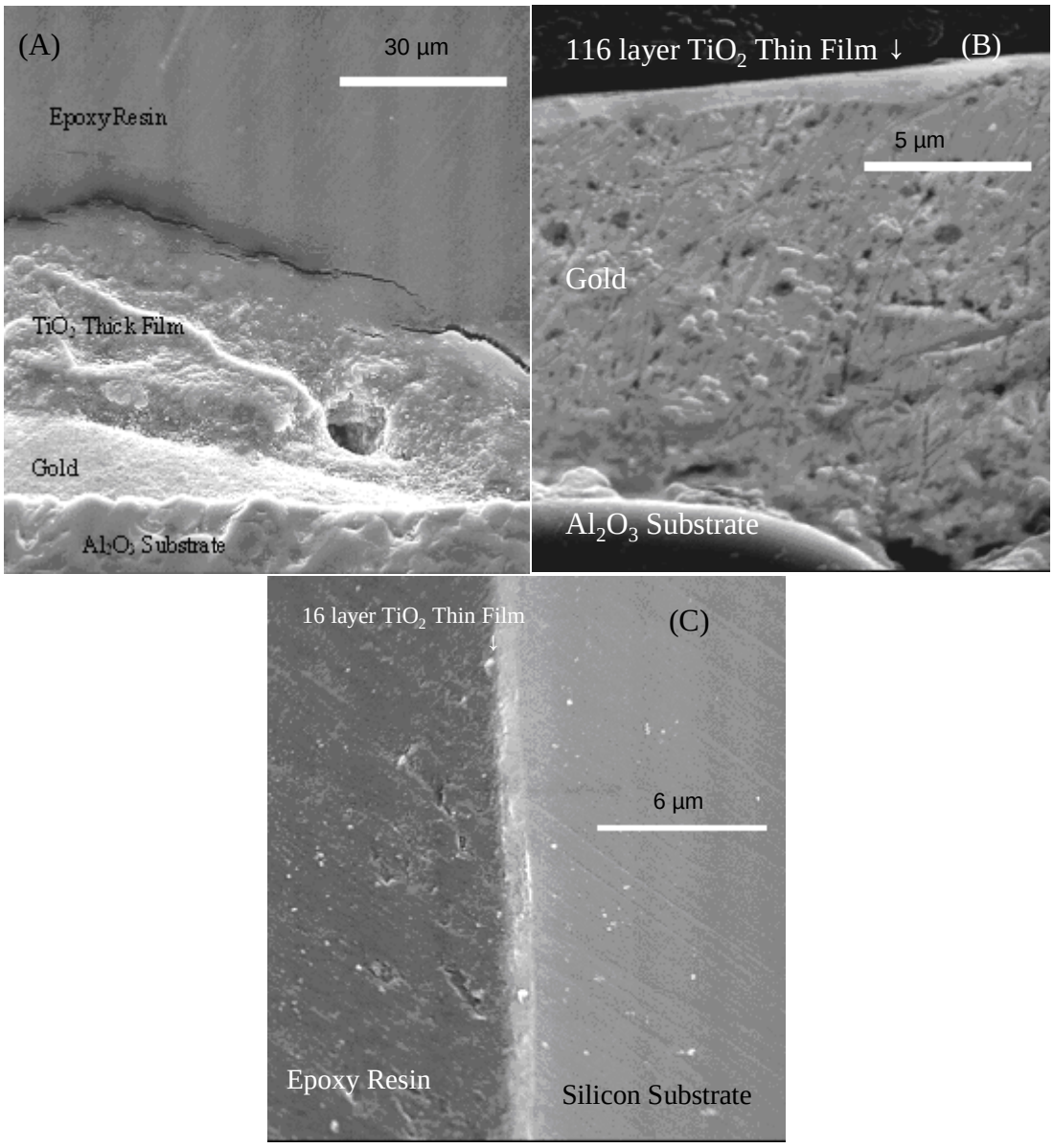

Figure 3.17. SEM images of the film cross-sections. (A) thick film on alumina substrate, (B) thin film on alumina substrate, and (C) thin film on silicon wafer.

3.4 Effect of TiO_2 Thin Film Crystallinity

XRD analysis was used to determine the crystalline phase present in the thin films. However, unlike the thick films, data could only be taken between the 2θ angles of 20 to 30° due to the dimensions of the films. XRD patterns for calcined TiO_2 thin films on alumina substrates

are shown in Figure 3.18. Anatase (JCPDS# 73-1764) is the only crystalline phase present for calcination temperatures between 600 and 800°C. The crystallite sizes for this temperature range, given in Table 3.3, are seen to increase with calcination temperature indicating that anatase crystallization and grain growth are taking place at these temperatures. After 900°C calcination, a significant amount of rutile (JCPDS# 87-0710) is detected in the TiO_2 thin films along with a dramatic increase in crystallite size.

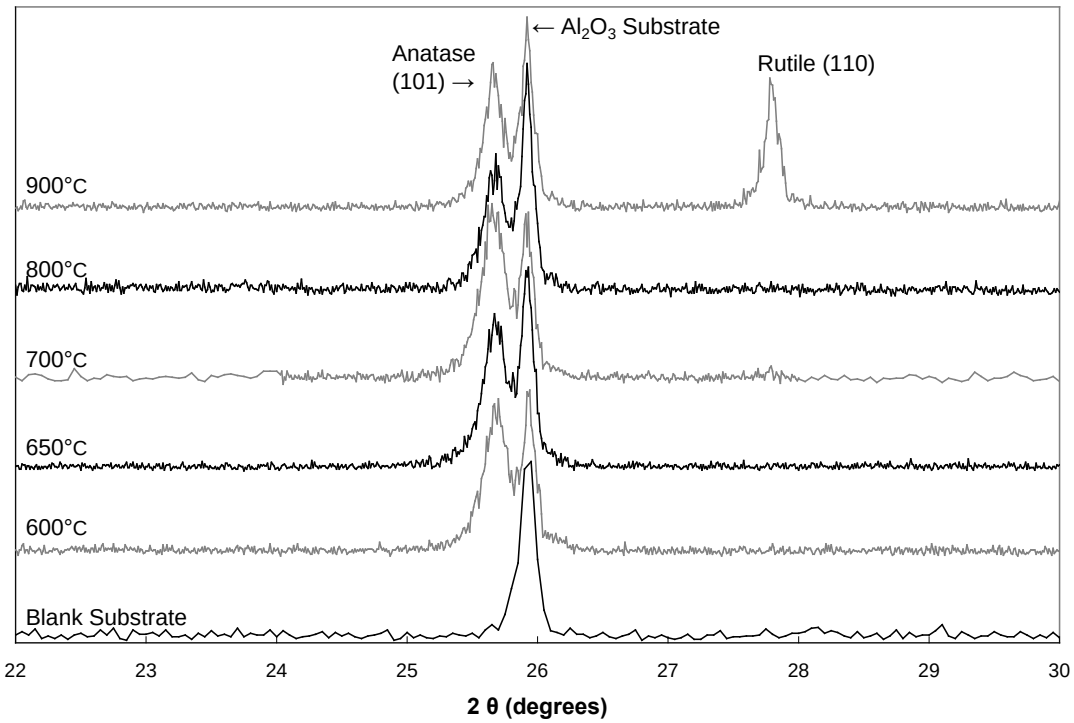

Figure 3.18. X-Ray diffraction patterns for 16 layer TiO_2 thin films on alumina substrates crystallized between 600 and 900°C.

Figure 3.19 shows the UV-VIS absorbance of pure TiO_2 thin films after calcination at 600, 800, and 900°C. The visible tail from each spectrum can be seen to be more prominent with increasing calcination temperature. This tail is thought to result from defect states in the band gap [Zhang '06]. This result is contrary to the expected result that increased crystallinity results in lower defect concentration, however, it is hypothesized here that the increase in crystallization

will lead to lower amounts of amorphous material on the surface of the particles. The improved crystallization will lead to more defined crystal structure and band gap properties, including defects which are not present in amorphous material.

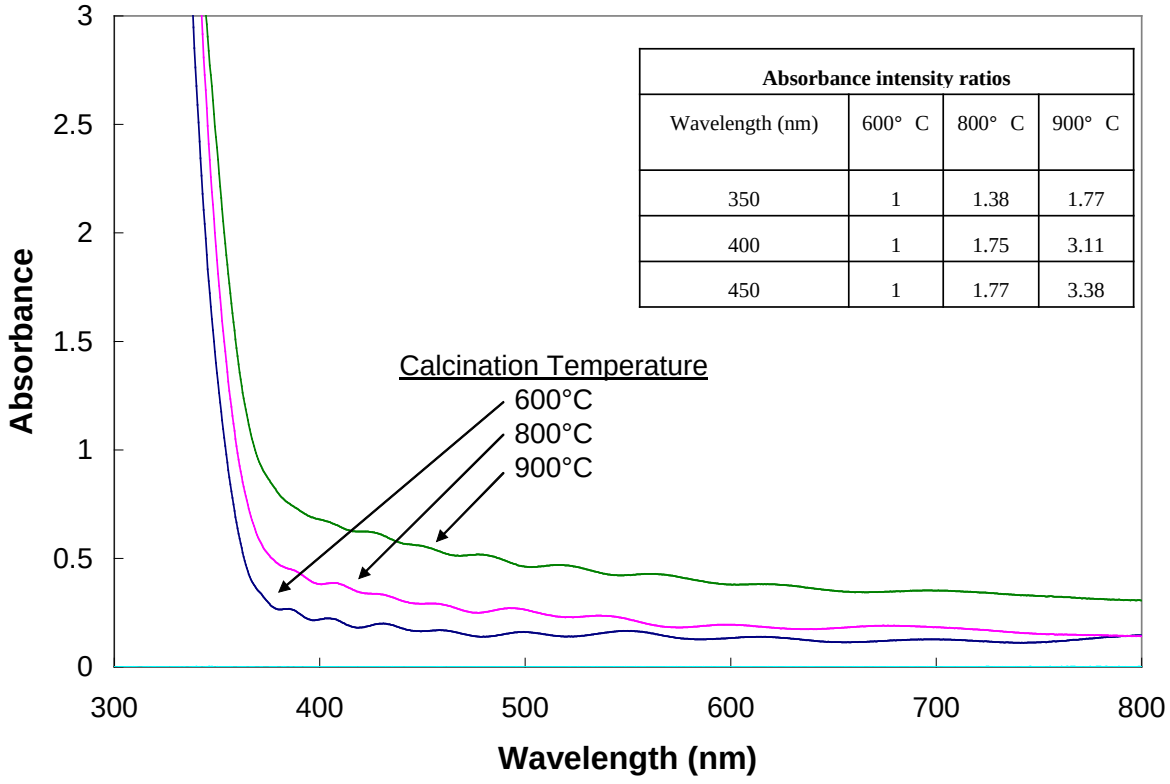

Absorbance intensity ratios			
Wavelength (nm)	600° C	800° C	900° C
350	1	1.38	1.77
400	1	1.75	3.11
450	1	1.77	3.38

Figure 3.19. UV-VIS absorbance of pure TiO_2 thin films calcined at 600, 800, and 900°C.

FE-SEM images of the film top surface are given in Figure 3.20 to show the TiO_2 grain size and microstructure after calcination between 600 and 900°C. Grain size is seen to increase with increasing temperature and is summarized in Table 3.3. During calcination between 600-800°C, grains are becoming more defined corresponding to the crystallization of anatase. After calcination at 900°C, grain boundaries are clearly visible and grains are larger, corresponding to the formation of rutile. This agrees with previous findings that anatase-to-rutile transformation is accompanied by significant grain growth [Ding '97, Ding '98]. All films do not contain any significant amount of porosity, although some cracking is visible due to the shrinkage during the

calcination and crystallization processes. These cracks, however, are only a layer or two deep and do not penetrate the entire film. Electrical properties confirm the fabrication of a continuous conducting film across the substrate.

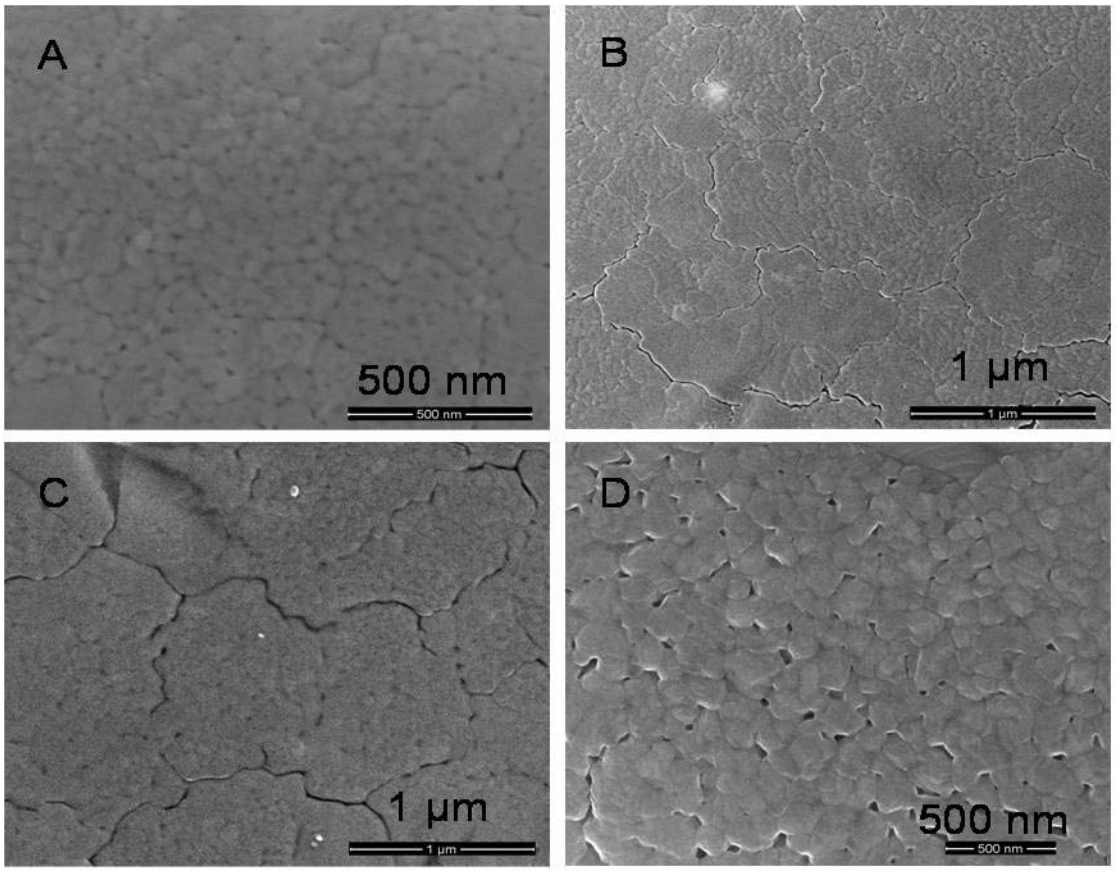

Figure 3.20. FE-SEM micrographs of the top surface of thin films calcined at (A) 600°C, (B) 700°C, (C) 800°C, and (D) 900°C.

Temperature-dependent resistances of the thin films were measured in the gas sensing apparatus. Figure 3.21 shows the resistance of the 700°C calcined film at operating temperatures ranging between 425 to 700°C in the baseline gas environment of 10%O_2. Arrhenius plots (Figure 3.21 inset) with linear fits were used to determine the activation energies for conduction in the TiO_2 thin films calcined at different temperatures, as summarized in Table 3.3. R^2 values for each linear trend line were greater than 0.99 suggesting good linear fits to the data. A steady increase in activation energy from 0.93 to 1.23 eV is noticed as film calcination temperature

increases from 600 to 800°C. These results agree with similar findings that activation energy increases with increased grain size [Demetry '99, Huber '05]. However, the 900°C calcined film shows a further increase in grain size but a decrease in activation energy. This result suggests that the formation of rutile is responsible for the reduction in activation energy. The smaller band gap of rutile (3.0 eV) compared with anatase (3.2 eV) may be responsible for this reduction in activation energy by allowing the vacancy donor sites to be located closer to the conduction band.

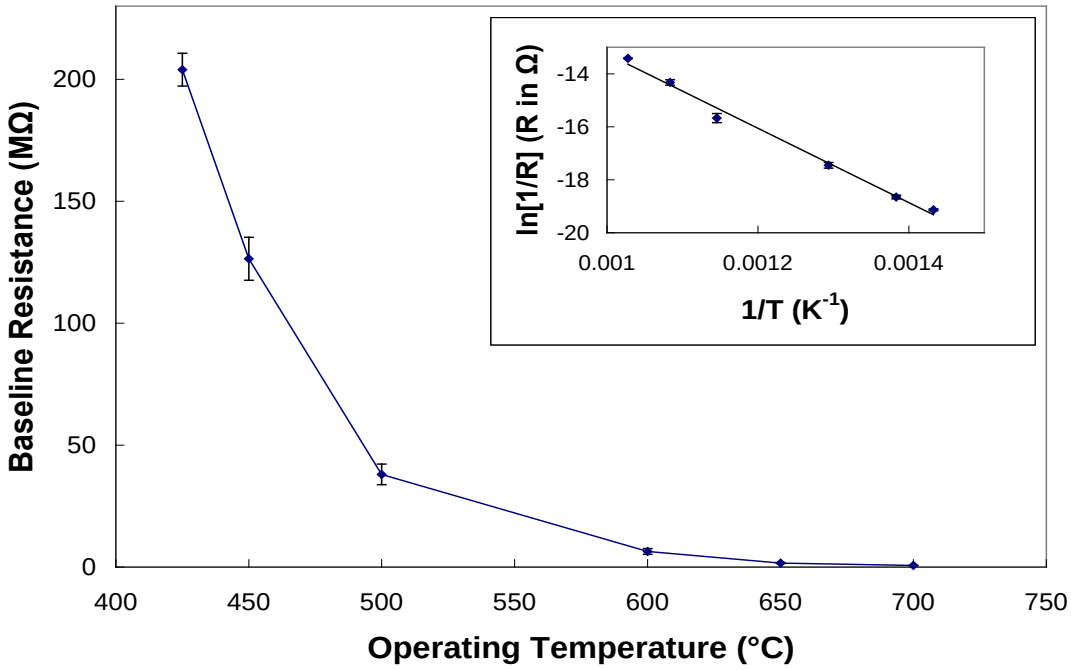

Figure 3.21. Resistance as a function of operating temperature in the background gas atmosphere of 10%O_2 balanced by N_2 for the 16 layer thin film calcined at 700°C. Inset is the Arrhenius plot of the natural log of the inverse resistance vs. inverse temperature and the slope is used to calculate activation energy.

Table 3.3. Crystallite size, particle size, crystalline phase, and activation energy for thin films calcined between 600 to 900°C.

Calcination Temperature (°C)	XRD Crystallite Size (nm)	Crystalline Phase	FE-SEM grain Size (nm)	Activation Energy E_A (eV)
600	28	Anatase	60	0.93
650	30	Anatase	75	1.16
700	30.9	Anatase	80	1.21
800	39.6	Anatase	130	1.23
900	51	Anatase + Rutile	150	1.16

An example of the dynamic sensing plot showing the change in sensor resistance for various O_2, CO, and CH_4 concentrations is shown in Figure 3.22 for the film calcined at 700°C and operated at 600°C. The film shows a stable baseline resistance signifying potential for long term operation at elevated temperatures. Response kinetics are fast, showing full recovery between target gas insertions.

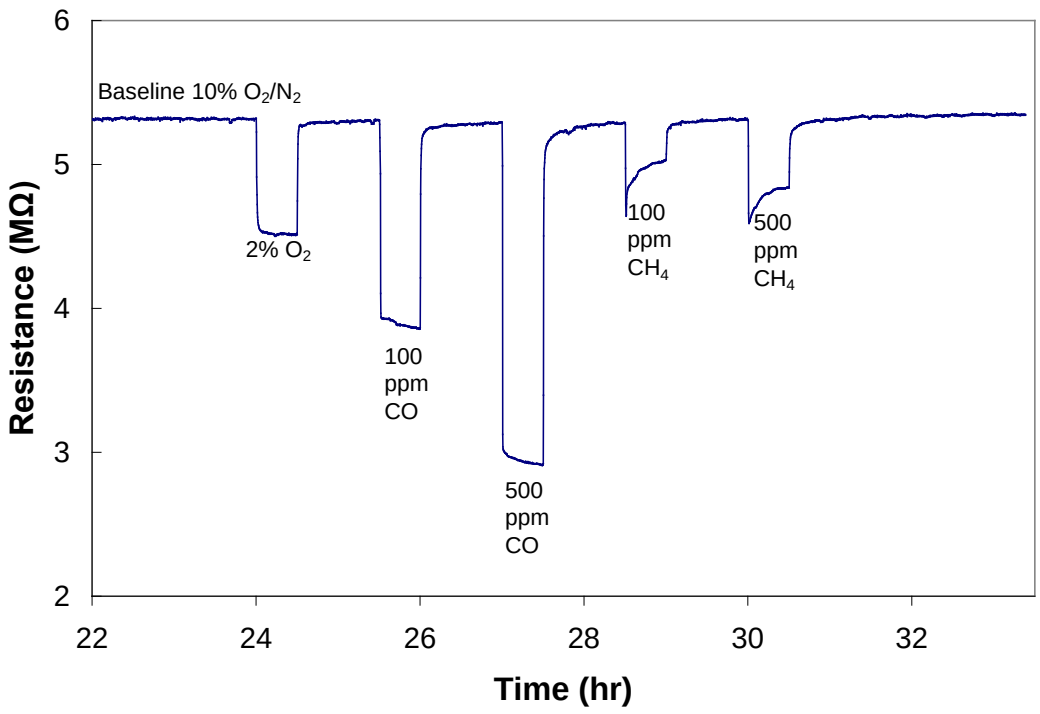

Figure 3.22. Oxygen, carbon monoxide, and methane kinetic sensing patterns for TiO_2 thin film calcined at 700°C and operated at 600°C.

Gas responses toward O_2, CO, and CH_4 are shown in Figure 3.23 for films calcined between 600 and 900°C and operated between 425 and 700°C. Three fundamental conclusions can be made from these results. First, all sensors showed degraded response to all target gasses when operated at 650 and 700°C. At this high temperature it is likely that the adsorbed oxygen ions are not stable on the TiO_2 surface and are desorbed without the reaction with a reducing

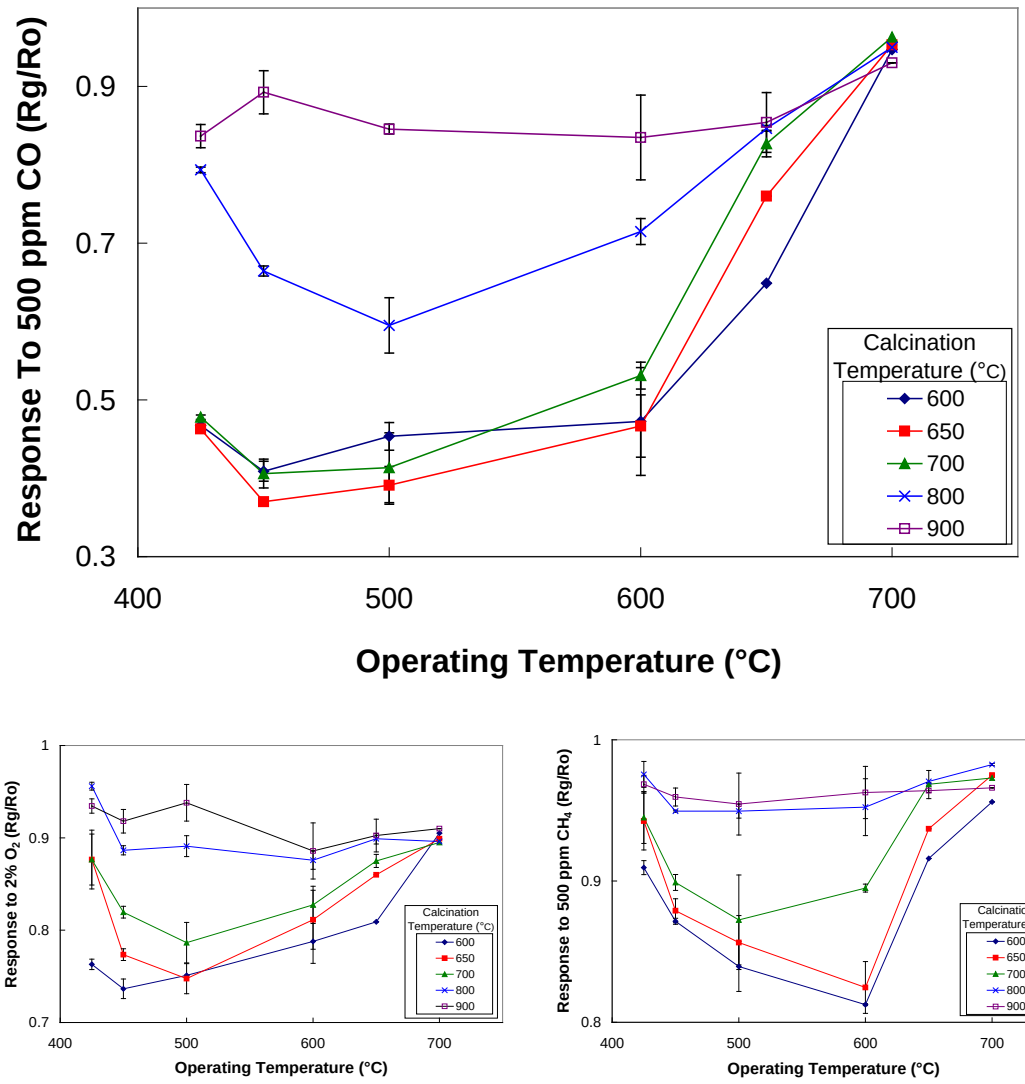

Figure 3.23. Thin film response towards 500 ppm carbon monoxide, 2 % oxygen, and 500 ppm methane as a function of calcination and operating temperatures. Background gas was constant 10 % oxygen balanced by nitrogen.

species. Lack of these adsorption/desorption reactions is responsible for the reduced gas response. Second, films calcined at lower temperatures (600-700°C) show a much better response to all target gasses compared with films calcined at high temperatures (800-900°C). This can be attributed to the smaller crystallite size providing more surface area for gas interaction in the films calcined at lower temperatures. Also, lower activation energies allow a higher concentration of electrons in the conduction band which take part in the sensing mechanism. Third, maximum CO response occurred at 450 to 500°C while the maximum CH_4 response is seen at 600°C. A similar trend has been observed for other metal-oxide sensors and is attributed to the higher energy required to decompose CH_4 before reaction is possible with the adsorbed oxygen [Kohl '01, Carotta '07].

In general, films show the high response to CO and the low response to CH_4 similar to previous findings for TiO_2 sensors [Savage '01]. Therefore, a quantitative analysis of the selectivity toward CO is defined here as the ratio of CO response to CH_4 response, as described earlier. CO selectivity is plotted in Figure 3.24 for all film calcination and operation temperatures. The film calcined at 900°C showed minimal CO selectivity due to the universally poor gas response. The films calcined between 600 and 800°C are most selective toward CO during operation at 425-500°C. Again, this is attributed to CH_4 requiring a higher temperature of 600°C to decompose and react with the adsorbed oxygen ions on the surface of the film. The film calcined at 650 and operated at 450°C showed the best selectivity toward CO. Selectivity of this film is attributed to the different thermal energies required to oxidize CO and CH_4. This film consistently showed the best material properties for gas sensors: high anatase crystallinity, small particle size, uniform film coverage and low activation energy.

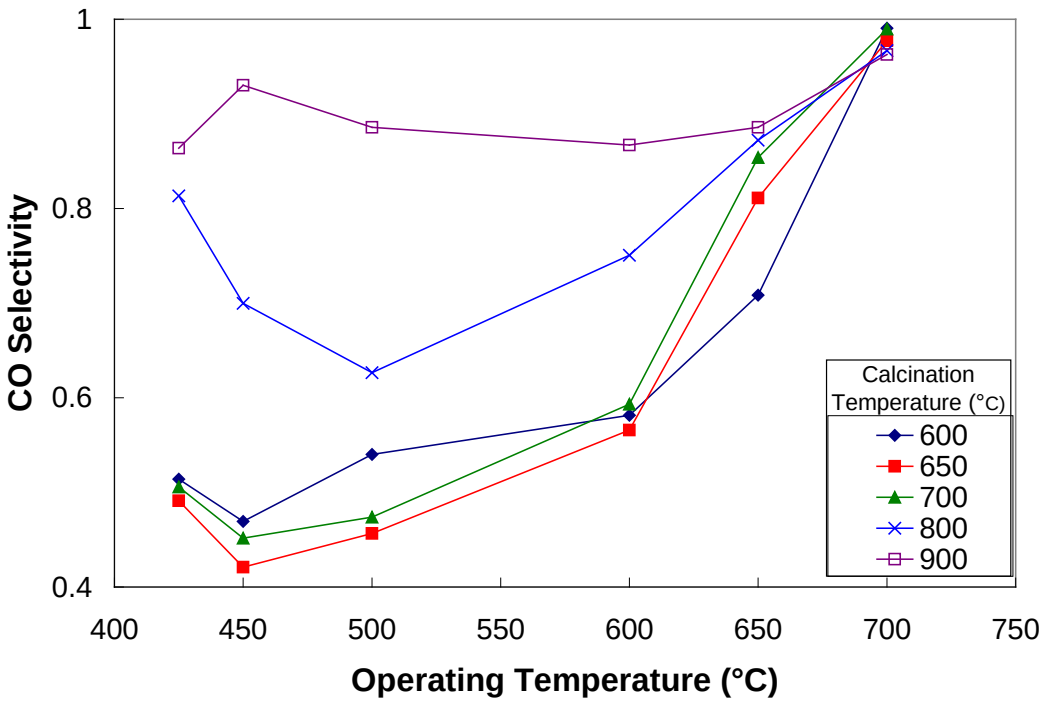

Figure 3.24. Thin film selectivity toward CO with respect to CH_4 for films calcined between 600 to 900°C and operated between 425 to 700°C. CO selectivity has been defined here as (CO response)/(CH4 response) for 500ppm of each target gas.

3.5 Effect of TiO_2 Thin Film Chemistry

XRD analysis on the W-doped TiO_2 thin films shows that below 900°C calcination, the crystalline phase of all films was anatase with no rutile formation. The concentration of tungsten did, however, influence the crystallite size, as summarized in Table 3.4. Addition of 2.5 and 5%W successfully hindered the anatase crystallite size compared with pure TiO_2 up to 800°C, however, with 10%W the crystallite size increased slightly. At 900°C calcination, rutile began to form in all samples, as shown in Figure 3.25. Again, addition of 2.5 and 5%W hindered the formation of rutile, while 10%W actually promoted rutile formation. These results of a low concentration of tungsten hindering crystallization and higher tungsten concentration promoting crystallization are similar to the findings described earlier for thick films.

Table 3.4. Crystallite size (nm) of pure and doped TiO_2 thin films calcined between 600 and 900°C measured from XRD

Calcination Temperature (°C)	Pure TiO_2	2.5% W	5% W	10%W	10% Ni
600	28	23	29	30	26
650	30	27	26	30	-
700	31	29	26	32	38
800	40	35	33	41	44
900	51	47	45	53	50

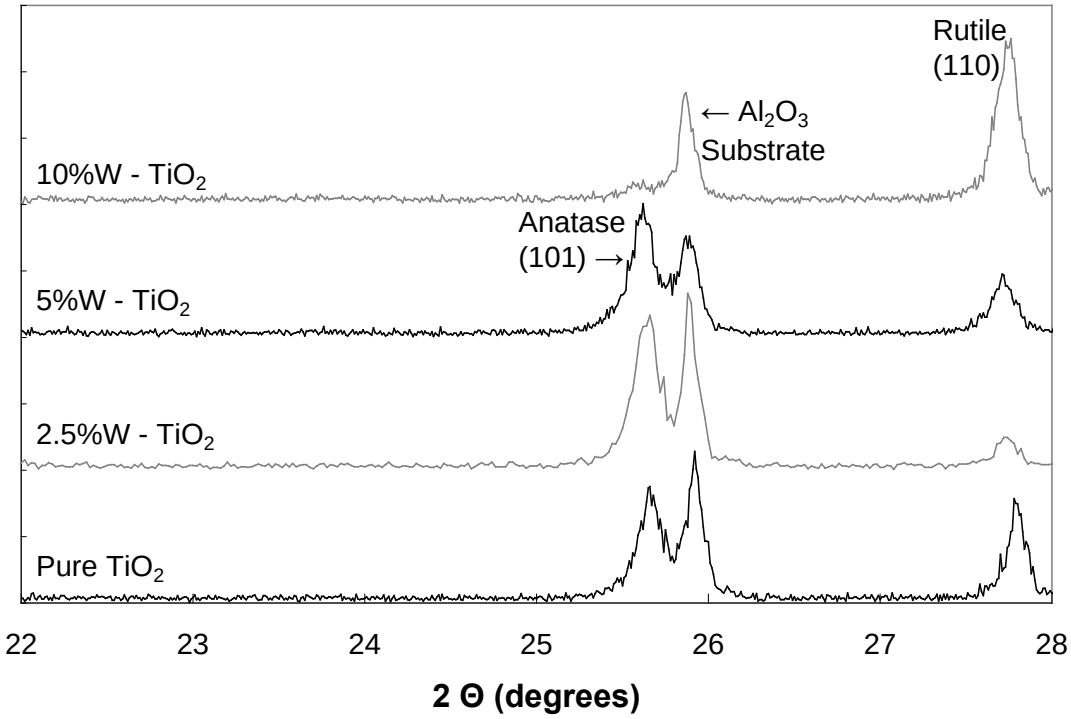

Figure 3.25. XRD patterns for pure and W-doped TiO_2 thin films calcined at 900°C.

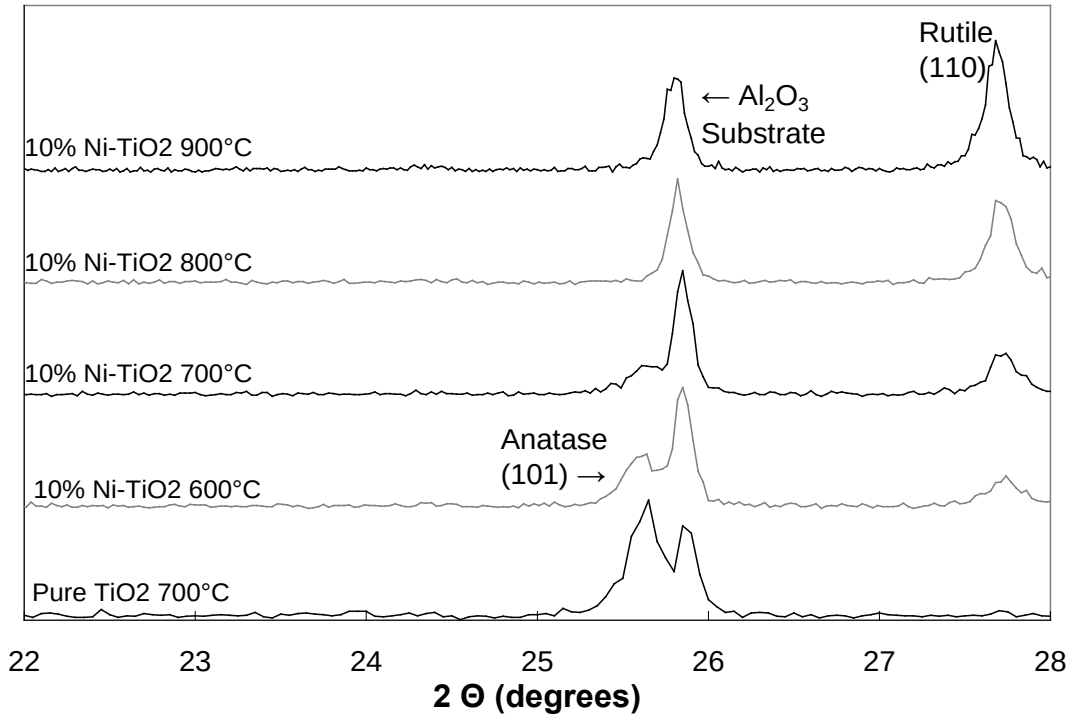

Figure 3.26. XRD patterns for 10%Ni-doped TiO_2 thin films calcined between 600 and 900°C.

Addition of 10%Ni showed to significantly promote the crystallization of rutile even at temperature as low as 600°C as shown in Figure 3.26, however the crystallite size appeared to be somewhat unaffected by the nickel as summarized in Table 3.4.

Figure 3.27 shows the top surface microstructure for pure, 10%W, and 10%Ni-doped TiO_2 thin films calcined between 600 and 900°C and Table 3.5 summarizes the grain sizes measured from these micrographs. Most films show low porosity with increasing grain size as calcination temperature increases. Pure and W-doped TiO_2 thin films have a fine grain size up to 800°C, then a large increase in grain size between 800 and 900°C is observed. This grain growth

Table 3.5. Grain size (nm) of pure, tungsten-, and nickel-doped TiO_2 after calcination between 600 and 900°C measured from FE-SEM micrographs.

Calcination Temperature (°C)	Pure TiO_2	10%W	10% Ni
600	60	40	-
700	80	45	80
800	110	120	200
900	200	300	250

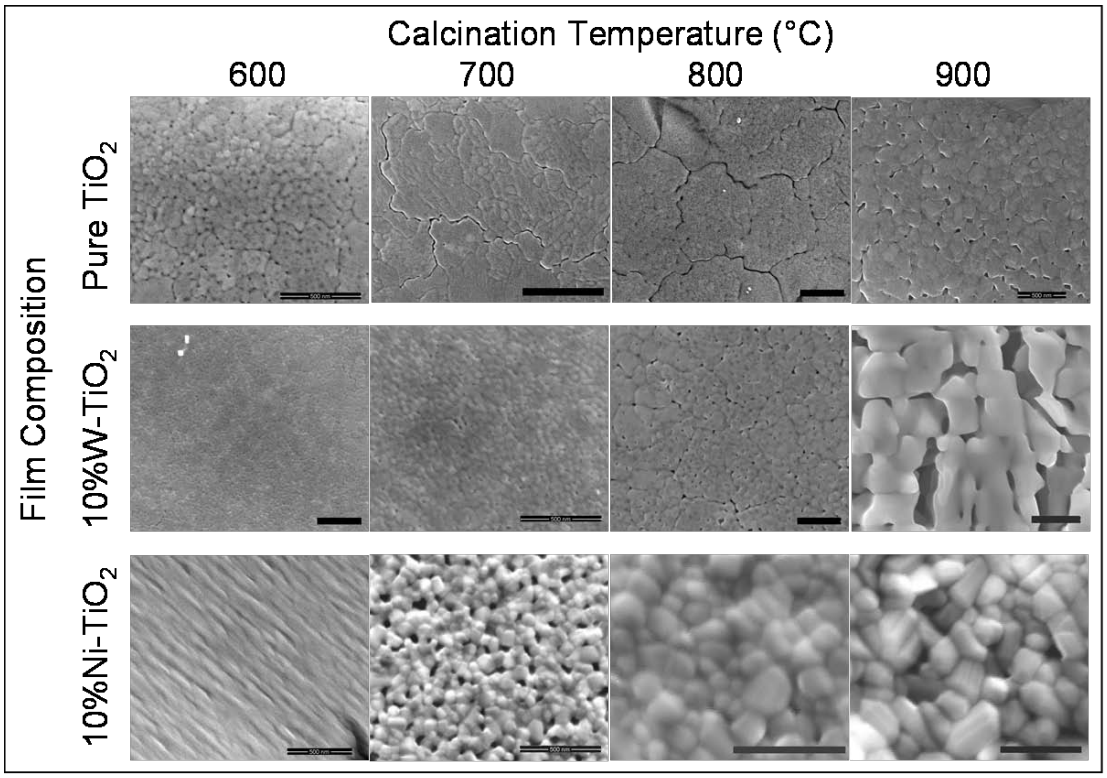

Figure 3.27. FE-SEM images of the top surfaces of thin films of pure TiO_2, 10%W-TiO_2, and 10%Ni-TiO_2 calcined at 600, 700, 800, and 900°C. All scale bars are 500nm.

is attributed to the anatase-to-rutile phase transformation at these temperatures. Ni-doped TiO_2 thin films, however, steadily increase in grain size as the temperature increases, which also correlates to a steady increase in rutile phase content in the samples.

Figure 3.28 shows the UV-VIS absorbance spectrum for pure, W-, and Ni-doped TiO_2 thin films. As discussed earlier, the visible tails can give some information about the defects in the electronic band gap. The addition of tungsten appears to have little effect on the band gap size, however, there is some absorbance all the way to 800 nm, indicating the presence of defects over a wide range of energy levels in the band gap. Nickel appears to lower the size of the effective band gap and create more defects between 400 and 500 nm, similar to results found by Hwang et al. [Hwang '06]. These results confirm the presence of defects in the crystal structure and electronic band gap; however, the exact type and energy levels need further investigation.

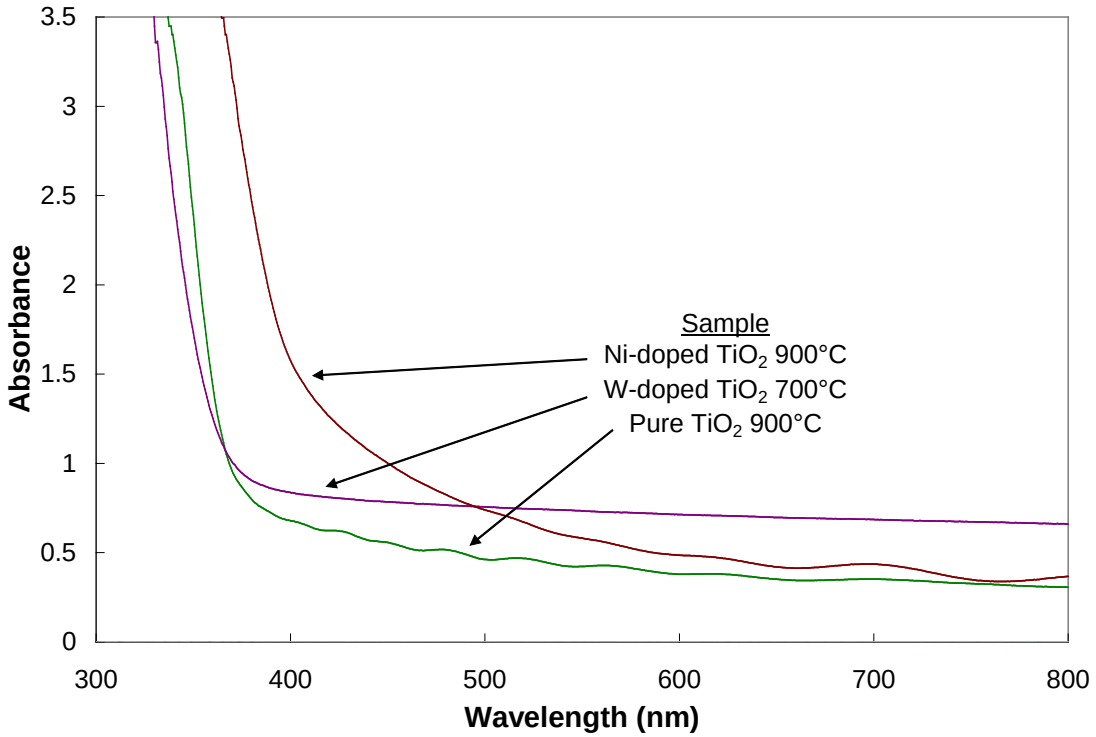

Figure 3.28. UV-VIS absorbance of pure, W-, and Ni-doped TiO_2 thin films.

Figure 3.29 shows the baseline resistance operating at 600°C for pure, W-, and Ni-doped TiO_2 thin films calcined between 600 and 900°C. Resistance of the pure TiO_2 thin films show strong dependence on calcination temperature. Calcination at 600°C is not sufficient to fully crystallize the material, resulting in low gas adsorption. A depletion layer is therefore not fully formed, leading to a lower film resistance. By 650°C, the pure TiO_2 film has reached sufficient crystallinity and the resistance reflects a fully formed depletion layer, however, upon further increase in calcination temperature the resistance decreases again. This decrease in resistance is attributed to grain growth, lowering the surface area and eventually the formation of rutile phase, decreasing the concentration of n-type oxygen vacancies.

The addition of tungsten or nickel significantly lowers the baseline resistance. This effect is attributed to the extrinsic defects increasing the number of charge carriers in the material. Addition of tungsten has a larger effect on the resistance than nickel. This is because tungsten

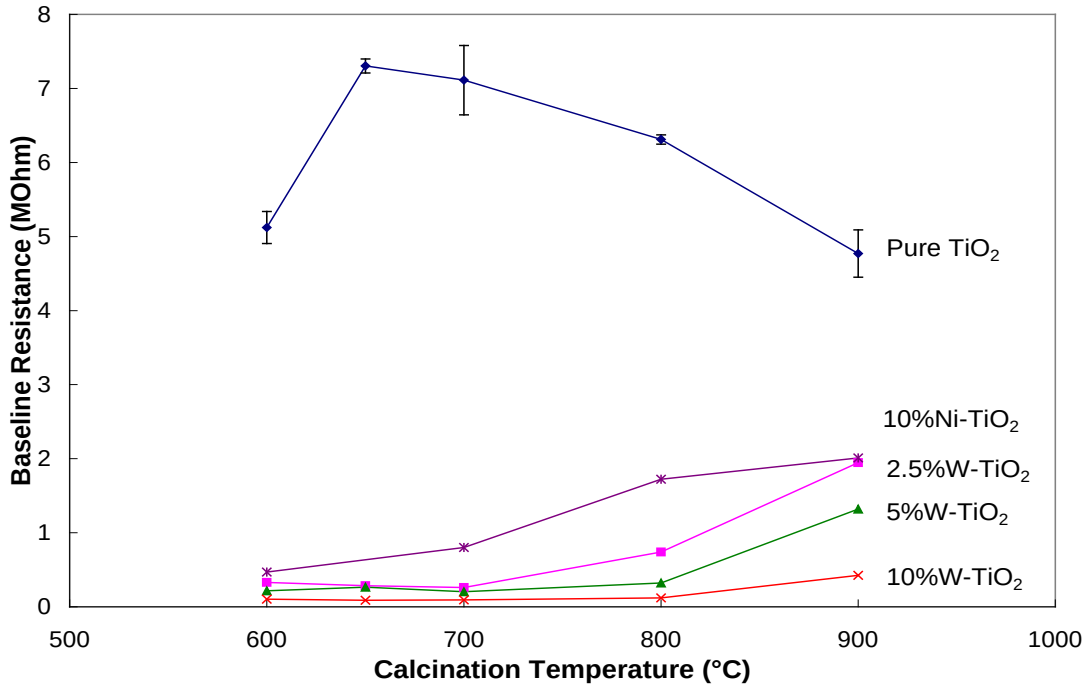

Figure 3.29. Baseline resistance for pure, W-, and Ni-doped TiO_2 thin films calcined between 600 and 900°C operating at 600°C

defects are n-type, which add to the intrinsic n-type behavior of pure TiO_2. Nickel defects are p-type, which may lead to some electron-hole annihilation, lowering the charge carrier concentration; however this effect is not dominant as seen by the reduction in resistance for Ni-doped TiO_2 films. It is also noticed that the resistance of doped films is more dependent on the dopant composition than the calcination temperature. This signifies that extrinsic defects are more dominant in controlling the conductivity of the material than the intrinsic defects under these conditions.

Figure 3.30 shows the gas response at 600°C to 500 ppm CO for pure, W-, and Ni-doped TiO_2 thin films calcined between 600 and 900°C. It is clearly noticed that the addition of tungsten improves the n-type gas response while addition of nickel converts the response to p-type. This is expected from the defect equations described in the previous chapter. Addition of

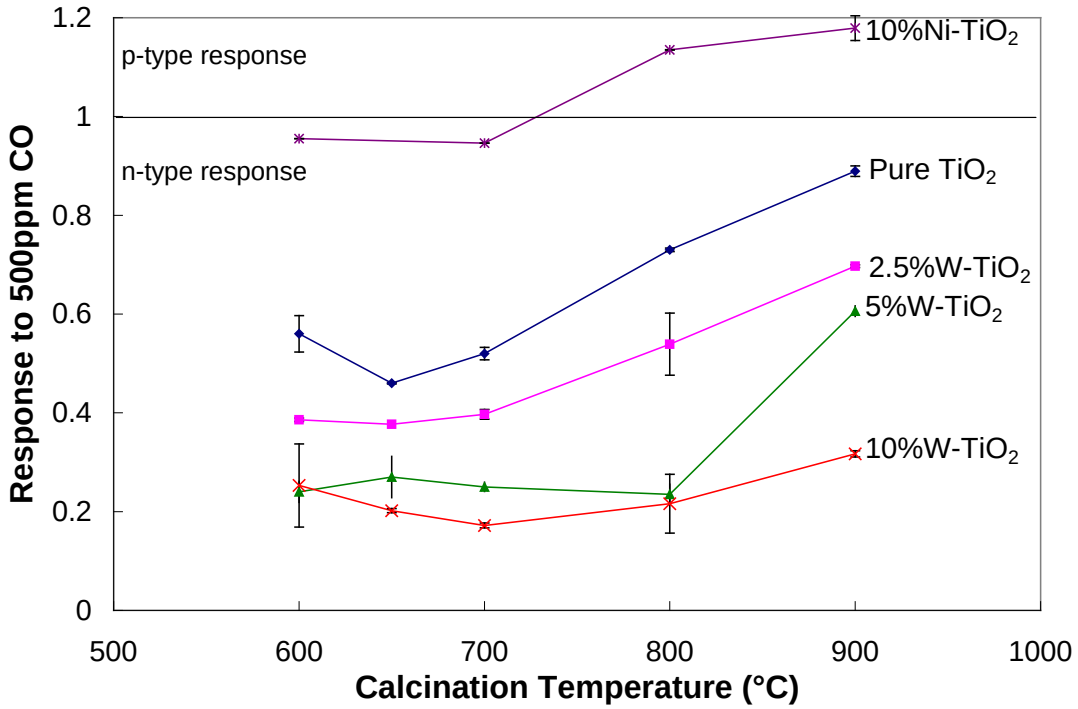

Figure 3.30. Gas response operating at 600°C to 500 ppm CO for pure, W-, and Ni-doped TiO2 thin films calcined between 600 and 900°C.

tungsten creates extra electrons available for conduction, confirmed by the resistance results. These electrons also play a role interacting with the target gas, improving the gas response of the films. The addition of nickel creates 'holes' which contribute to the p-type conduction in the films. Upon reaction with CO, electrons that were trapped in adsorbed oxygen bond are released back into the TiO_2 and can then recombine with the 'holes' annihilating charge carriers and increasing the resistance. This reaction describes the p-type response. It is interesting to note that the Ni-doped films require a higher calcination temperature to achieve a fully p-type response. This indicates that a higher degree of crystallization is required to achieve a sufficient concentration of 'holes'. It is possible that crystallization is necessary to incorporate the nickel atoms into the TiO_2 crystal structure, resulting in the formation of a 'hole'. Without this

crystallization, nickel atoms can appear randomly in an amorphous structure and not create 'holes' due to lack of crystal defect charge conservation.

Another interesting feature of Figure 3.30 is the profile of the W-doped films. Pure TiO_2 films have the best response at 650°C calcination and the response degrades with increasing calcination temperature. 2.5%W films have a good response up to 700°C and then response degrades at higher calcination temperatures. 5%W films show a good response up to 800°C calcination and degrade at 900°C, and finally 10%W films show an essentially good stable response for all calcination temperatures up to 900°C. The film with 10%W calcined at 900°C showed very large crystallites and grains, and also was nearly 100% rutile phase. These results indicate that the addition of tungsten is dominating the sensing response irrespective of the microstructure or crystalline phase.

Figure 3.31 shows the response to 500 ppm CH_4 for the same films previously discussed. In general, these TiO_2 thin films show a significantly lower response to CH_4 than CO. In a similar trend to CO response, however, the addition of tungsten improves the n-type response and nickel creates p-type response. The difference between the two target gas responses is the direct relation between tungsten concentration and CO response, whereas 2.5%W actually degrades the response to CH_4 compared with pure TiO_2 and 10%W improves the response to CH_4. These results indicate the tungsten concentration could be used to control the gas selectivity between CO and CH_4 in the prepared TiO_2 thin films.

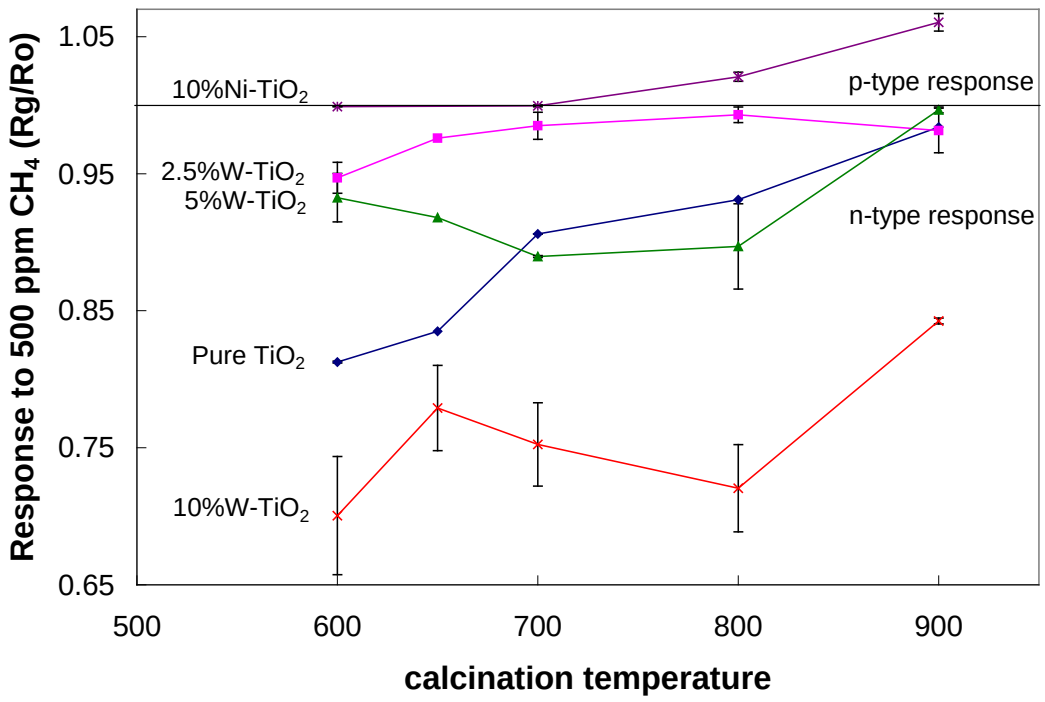

Figure 3.31. Gas response operating at 600°C to 500 ppm CH_4 for pure, W-, and Ni-doped TiO2 thin films calcined between 600 and 900°C.

From these results, three compositions and calcination temperatures were chosen for further studies on chemistry. Pure TiO_2 calcined at 700°C was chosen as the standard to which other films were to be compared. The calcination temperature of 700°C was chosen so that the film would remain stable up to an operating temperature of 700°C. 10%W-TiO_2 calcined at 700°C was chosen as the most n-type film produced, and finally 10%Ni-TiO_2 calcined at 900°C was chosen as the most p-type film produced. Figure 3.32 shows the dynamic response plots for these three films where the resistance has been normalized to the baseline resistance to show the relative n- and p-type responses.

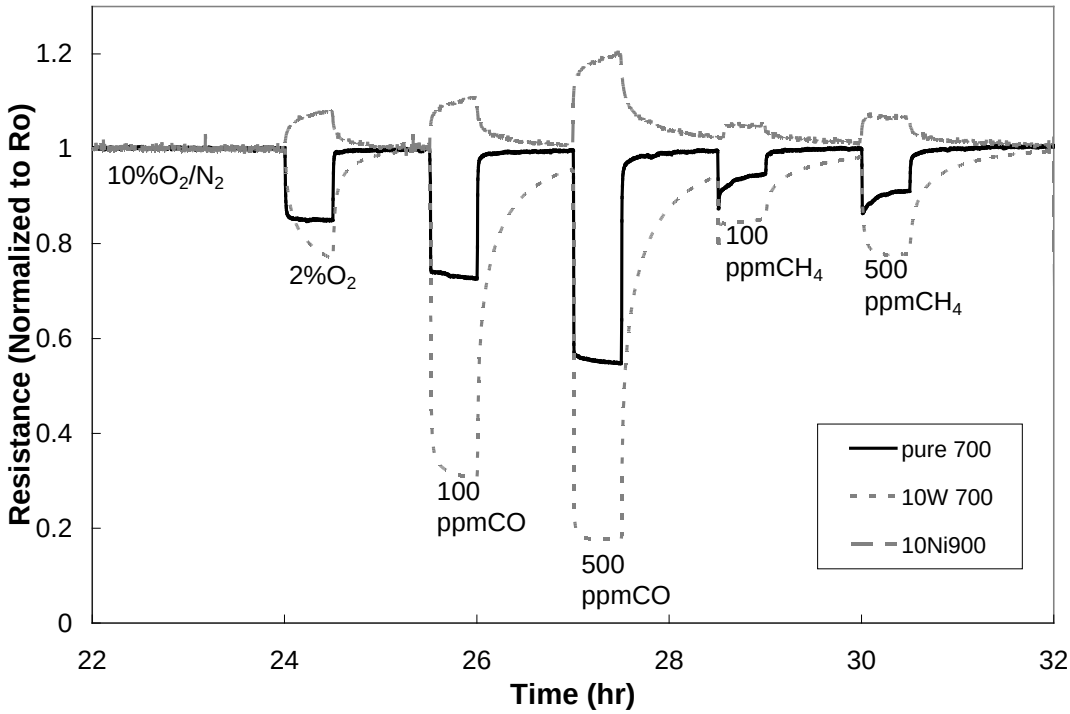

Figure 3.32. Dynamic gas response plots for thin films of pure TiO_2, W-doped n-type TiO_2, and Ni-doped p-type TiO_2. Operation temperature is 600°C.

To further understand the influence of chemistry on gas response of TiO_2 thin films, the operating temperature was controlled between 300 and 700°C. From this data, the activation energy for conduction was determined, as well as the temperature dependent gas response. Figure 3.33 shows the baseline resistance as a function of operating temperature for pure, W-, and Ni-doped TiO_2 thin films. The activation energies for conduction were calculated from the Arrhenius equation and are summarized in Table 3.6. It is evident that the incorporation of the dopant atoms is significantly influencing the resistance of the films by changing the activation energy for conduction. While pure TiO_2 films show activation energy of 1.22 eV, consistent with the presence of doubly ionized oxygen vacancy defect sites in the band gap, the addition of tungsten shows activation at 0.61eV. This indicates that tungsten substitution for titanium leads to an electron which is loosely bound to the defect site and only takes approximately 0.6eV to

excite into the conduction band. This result is consistent with previously reported findings [Komornicki '04]. Similarly, the substitution of a nickel atom for titanium results in a 'hole' that is approximately 1.1eV above the valence band.

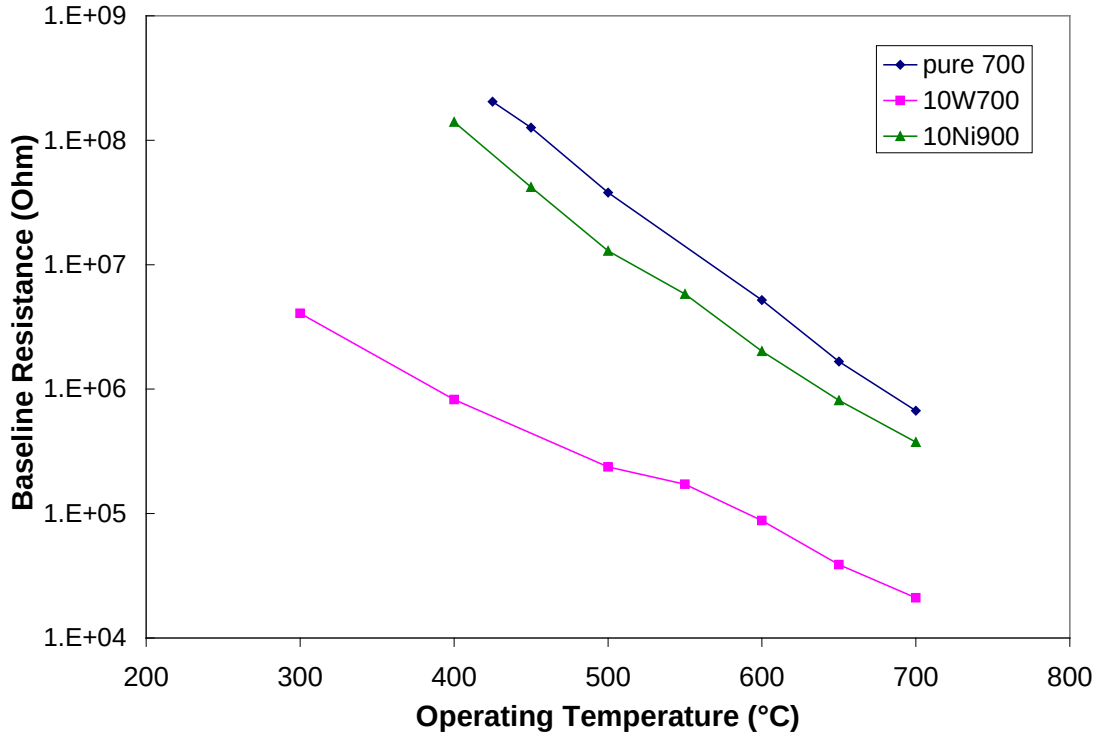

Figure 3.33. Baseline resistance for pure, W-, and Ni-doped thin films operating between 300 and 700°C.

Table 3.6. Calculated activation energies for pure, W-, and Ni-doped TiO2 thin films.

sample	E_a (eV)
pure TiO_2	1.22
10%W TiO_2	0.61
10%Ni TiO_2	1.11

Figure 3.34 shows the gas response to 500 ppm CO for pure, W-doped n-type, and Ni-doped p-type TiO_2 thin films operated between 300 and 700°C. Gas responses for all films at both low and high operating temperatures are degraded. At low operating temperatures the films' resistances are high, as there is not enough thermal energy to excite electrons into the conduction band which then participate in the sensing mechanism. Also, the gas-surface reactions are slow at low temperatures. At high temperatures near 700°C, adsorbed

oxygen is not stable on the surface, leading to a low depletion layer formation and low gas response. The addition of tungsten or nickel in TiO_2 thin films raises the optimum operating temperature compared with pure TiO_2. The extra available electrons produced by the tungsten defects sites may be responsible for creating a stronger bond for the surface adsorbed oxygen.

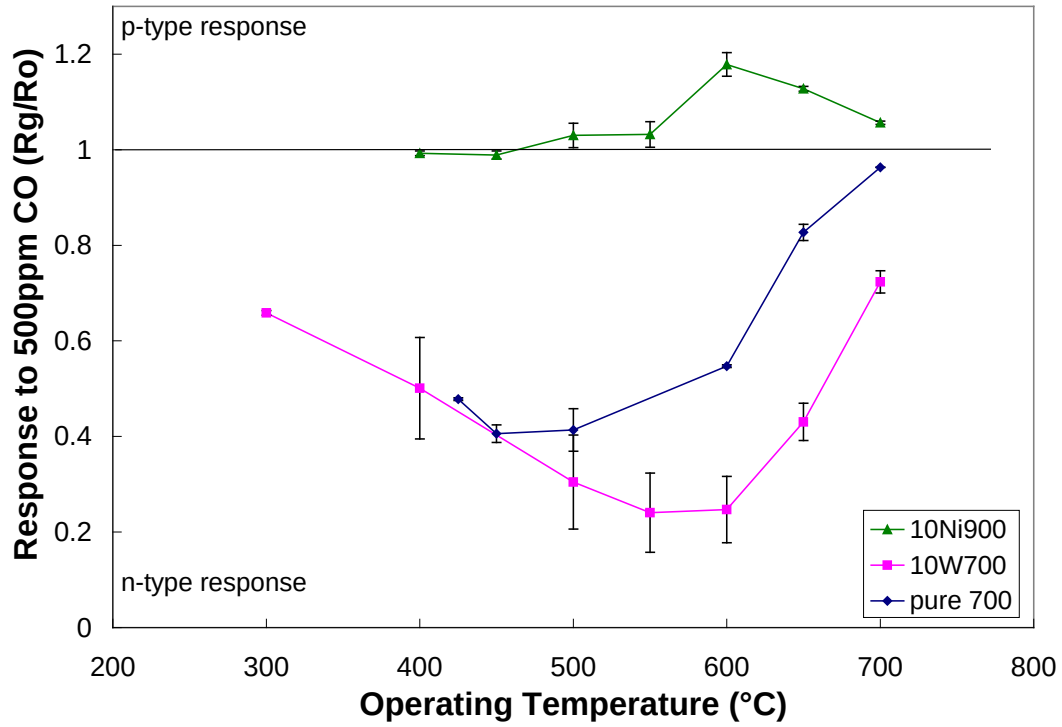

Figure 3.34. Gas response to 500 ppm CO for pure, W-, and Ni-doped TiO_2 thin films operating between 300 and 700°C.

Figure 3.35 shows the gas sensing response to 500 ppm CH_4 for the same films. The pure TiO_2 film shows a similar trend to the CO response, with CH_4 response maximizing at 500°C operation. The W-doped sample also seems to follow this trend with the exception of the 300°C operation data point. The main difference between the CO and CH_4 responses is that tungsten obviously improves the CO response while it does not significantly improve the CH_4 response. This trend is most noticeable during operation at 600°C where the application of these types of sensors is most useful.

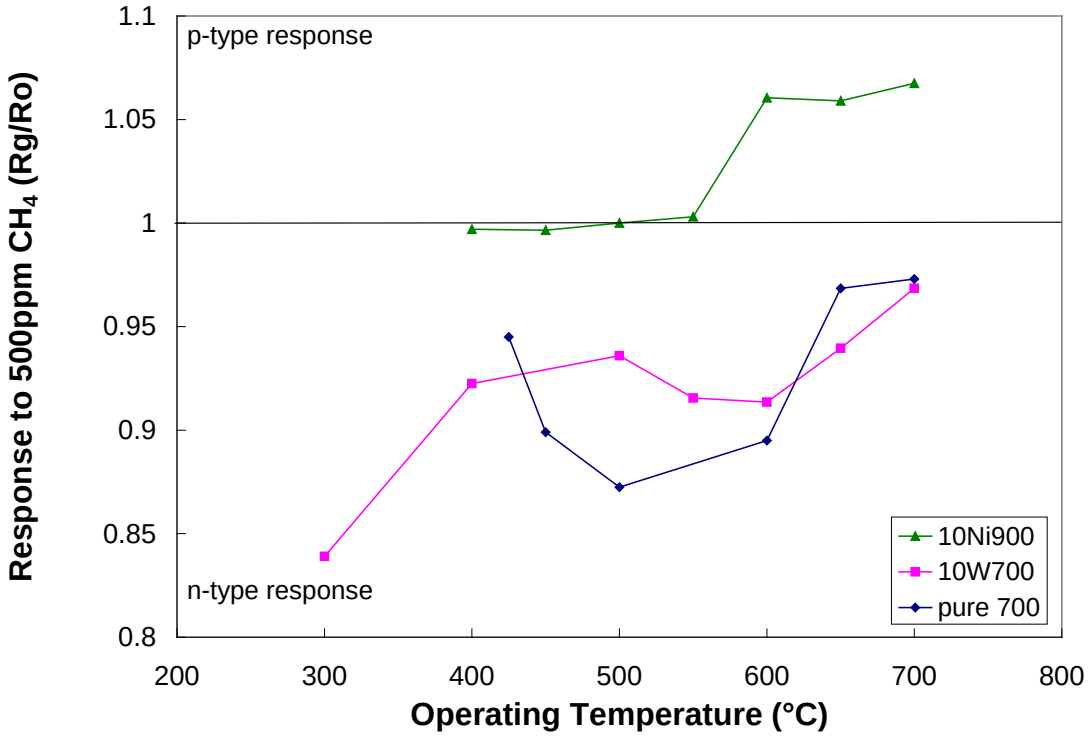

Figure 3.35. Gas response to 500 ppm CH_4 for pure, W-, and Ni-doped TiO_2 thin films operating between 300 and 700°C.

3.6 Bi-Layer n-p Composite TiO_2 Thin Films

In the previous section we have optimized several of the parameters for creating doped TiO_2-based thin films with both n- and p-type conduction and gas response. In order to characterize the effects of a bi-layer film composed of two layers, one n-type and one p-type, on sensing properties, we have fabricated several variations of composite films. Atomic diffusion from one layer to the other is a concern for these bi-layer films. Therefore, the sample composed of 8 layers of Ni-doped TiO_2 calcined at 900°C followed by 8 layers of W-doped TiO_2 calcined at 700°C was cross-sectioned and scanned with an FE-SEM equipped with a "Gensis EDAX" energy-dispersive spectrometer (EDS). Line scans from the substrate through the bottom layer

of the film to the top layer were performed and analyzed for titanium, oxygen, tungsten, and nickel content.

The FE-SEM images and results from the EDS lines scan are shown in Figure 3.36. The FE-SEM image shows the cross-section of the film with the silicon substrate on the left side, the film in the middle, and the epoxy resin on the right side of the image. Therefore the left edge of the film is the bottom where it meets the substrate, and the right edge is the top surface. The line through the image is the EDS line scan, and the graph below has the same dimensional x-axis as the image. Titanium and oxygen EDS peaks were more intense than the nickel and tungsten, therefore the y-axis of the chart is normalized to the maximum intensity for each element so that the profiles could be viewed. Titanium and oxygen show very nice profiles with very little concentration in the substrate and resin, and significant concentration in the film. The spatial resolution for this EDAX system is said to be approximately 1 μm, however, from these two elements (Ti and O) we can see that the resolution is better than 500 nm estimated from the profiles near the edges of the film. Tungsten and nickel both gave very weak signals in the EDS scan; however, some qualitative analysis of ionic concentrations can be made. Nickel concentration is maximum near the bottom of the film, which is expected since the bottom half 8 layers were deposited with Ni-doped sol. The concentration decreases across the entire width of the film, indicating a significant amount of Ni diffusion from the bottom to the top of the film has taken place during crystallization. Tungsten concentration is nearly constant through the substrate and bottom half of the film, then increases quickly for the top half. This results indicates that very little diffusion of tungsten atoms has taken place during crystallization. Due to the low resolution of the instrument, poor focus on the image, and weak signal from Ni and W, these results must be taken lightly, however; we can conclusively state that nickel concentration

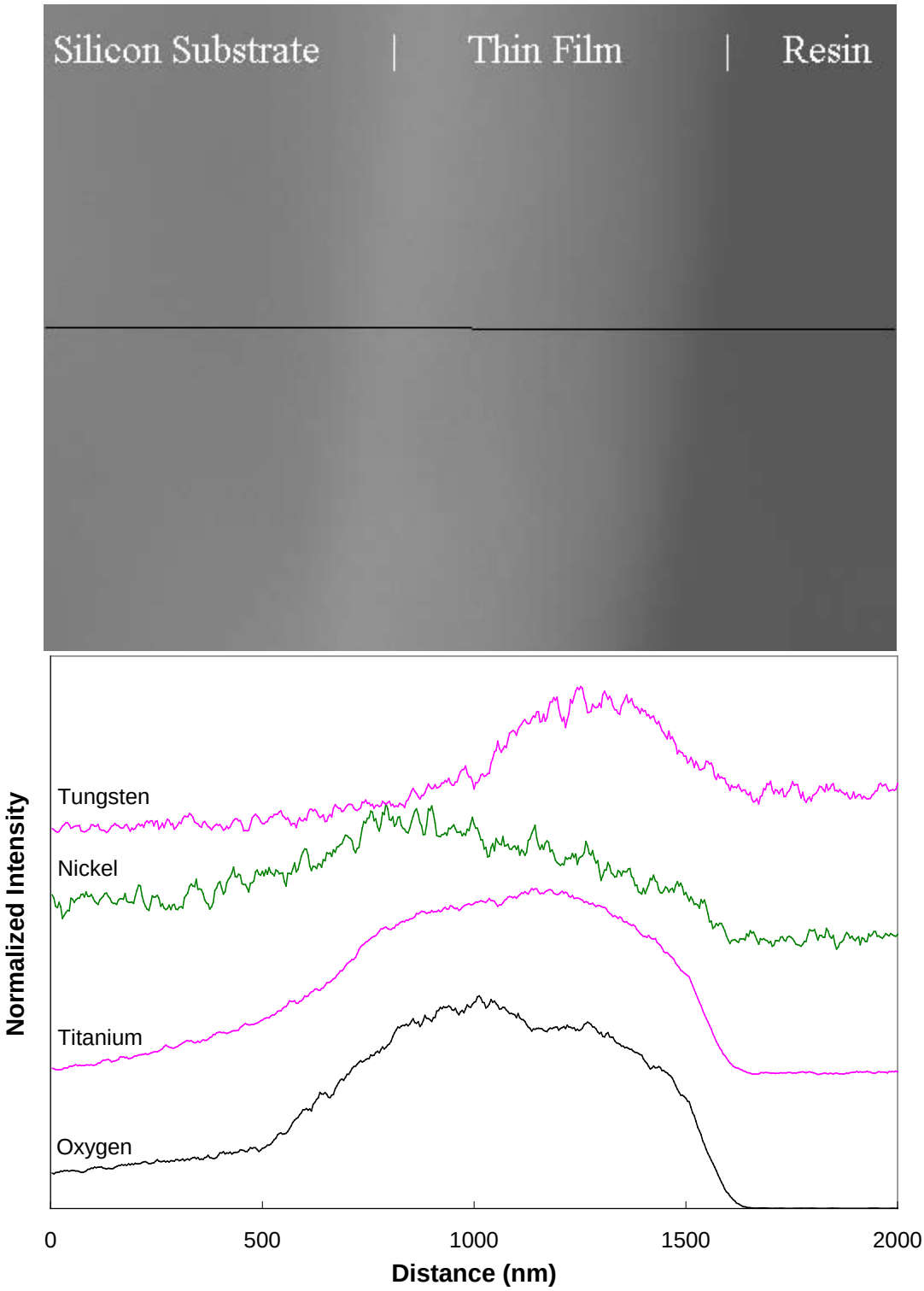

Figure 3.36. FE-SEM image and EDS line scan through the cross-section of the thin bi-layer film composed of 8 layers of Ni-doped TiO2 calcined at 900°C followed by 8 layers of W-doped TiO2 calcined at 700°C.

is higher near the bottom of the film, and tungsten concentration is higher near the top of the film.

Figure 3.37 shows the baseline resistances of the bi-layer thin films while operating between 300 and 700°C. Pure TiO_2 gave the highest resistances due to lack of extrinsic defects and the Ni-doped film only lowered the resistance slightly. The complete W-doped films gave the lowest resistance due to the most n-type defects. All the bi-layer film resistances fell between the two single-doped films. This indicates that the total resistance of a bi-layer film is related the sum of the two layers, however a more significant result comes from noticing the order of the layers. Resistance of the film with tungsten on bottom and nickel on top is very near the complete nickel-doped film. The reverse of this film with nickel on bottom and tungsten on

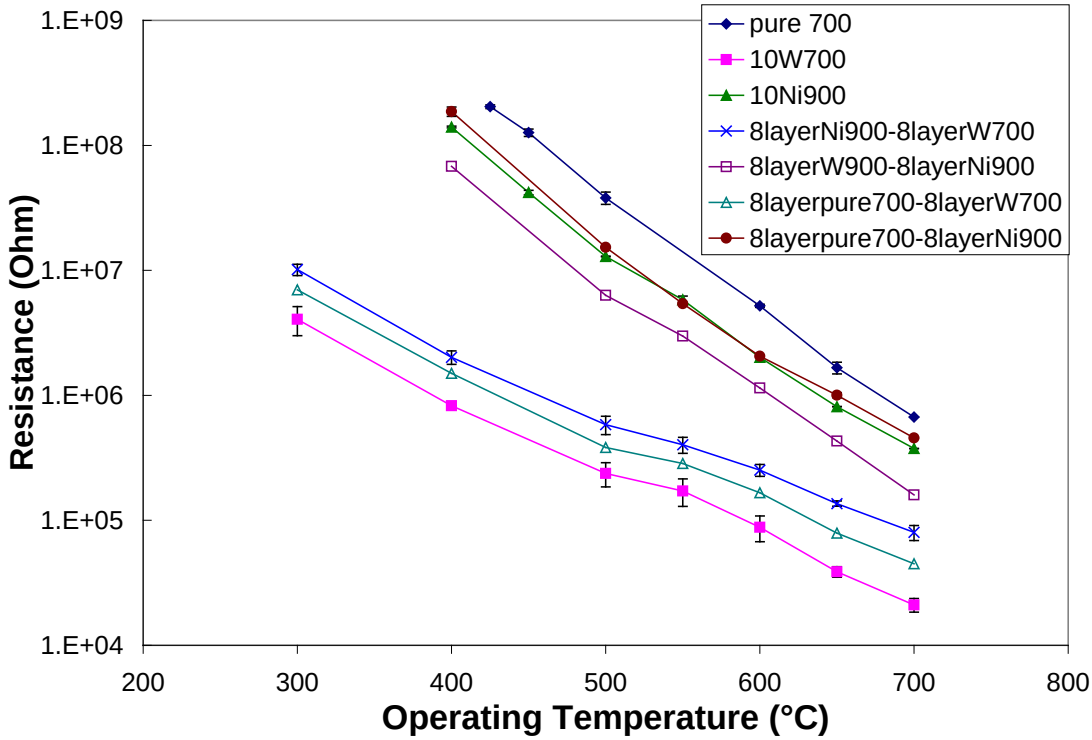

Figure 3.37. Baseline resistance for bi-layer n-p composite TiO_2-based thin films operating between 300 and 700°C.

top is very near the complete tungsten-doped film. This indicates that the top layer of the bi-layer films influences the resistance more significantly than the bottom layer.

Figure 3.38 shows the CO gas response for thin films composed of half Ni-doped and half W-doped TiO_2. The film with Ni-doped TiO_2 on bottom and W-doped TiO_2 on top shows the closest response to the complete W-doped TiO_2 film. The film with W-doped TiO_2 on bottom and Ni-doped TiO_2 on top shows a degraded n-type response. This result indicates that the order of Ni-doped and W-doped TiO_2 layers plays an important role in the gas response. Similar to the baseline resistance, the top layer of a bi-layer film appears to influence the gas response more significantly than the bottom layer. This indicates that the gas is reacting mostly with the outermost layer as it diffuses into the film. Less gas is reacting with the bottom layer most likely due to less volume of reactive gas reaching this layer. These results could be used in future studies to design highly advanced sensing films.

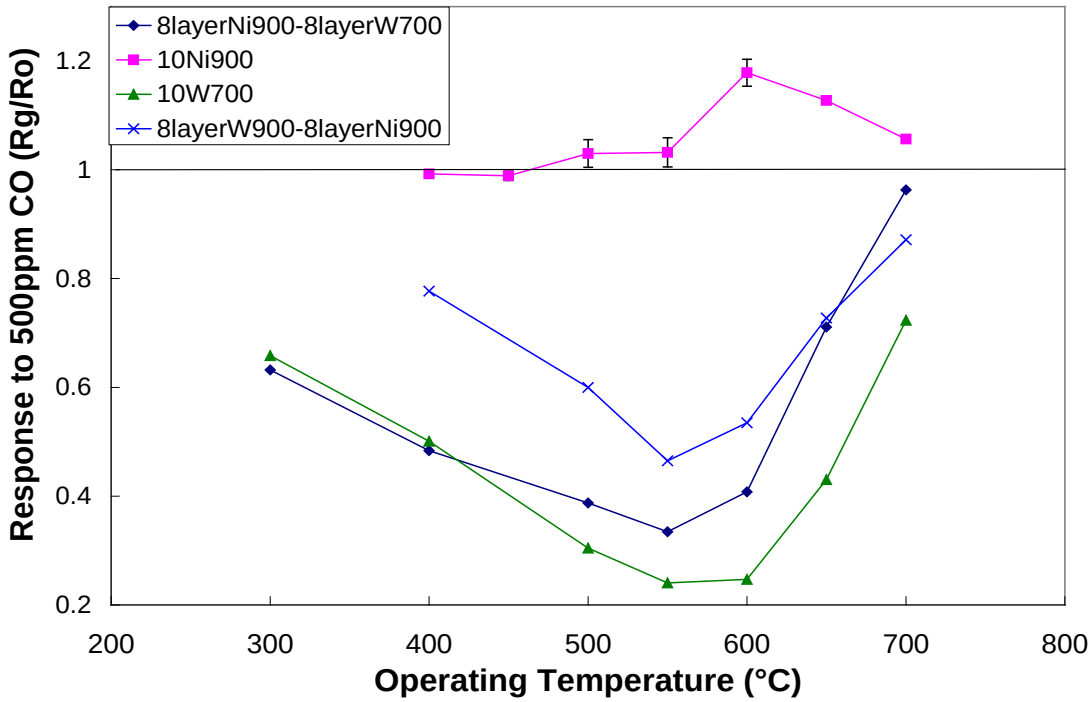

Figure 3.38. CO gas sensing response for Ni-W-doped TiO_2 bi-layer thing films. Shows the effect of location of the Ni and W layers on CO response.

Figure 3.39 shows the influence of the bottom layer composition of the bi-layer thin films on gas response by exchanging the bottom layer from Ni-doped TiO_2 to pure TiO_2 and

maintaining the top layer as W-doped TiO_2. At higher operating temperatures, the film with pure TiO_2 on bottom performs better. This is expected because pure TiO_2 is a weak n-type conductor and Ni-doped TiO_2 is a weak p-type conductor. At high operating temperatures the p-type conduction cancels out some of the n-type conduction of the top W-doped TiO_2 layer degrading the response; however, the pure TiO_2 only degrades the response slightly.

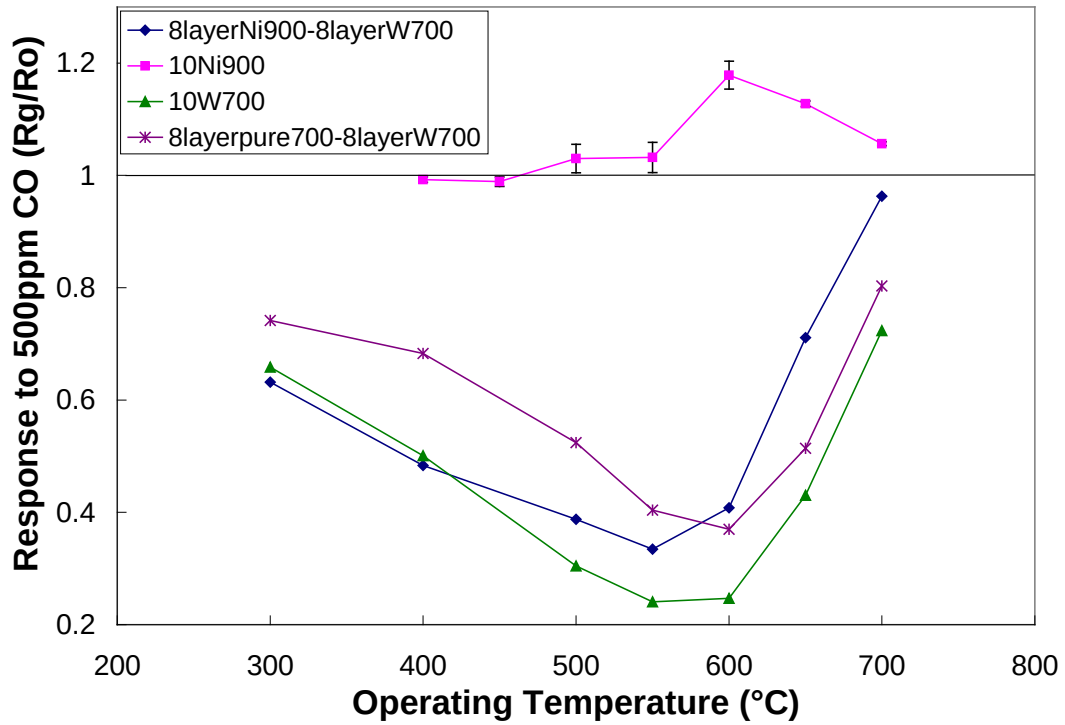

Figure 3.39. CO gas response for bi-layer films with W-doped TiO_2 on the top layer, and either Ni-doped TiO_2 or pure TiO_2 on the bottom layer.

An interesting feature of Figure 3.39 is the response at lower operating temperatures. It is noticed that at lower temperatures the film with Ni-doped TiO_2 on bottom responds better than the film with pure TiO_2 on bottom and even slightly better than the complete W-doped TiO_2 film. The n-p composite film, at these lower temperatures, may be providing some effect of a p-n junction as hypothesized in the introduction. High operating temperatures lead to large diffusion of charge carriers across the junction and annihilation, and thus the films behave as if they are

composed of a single film with uniform charge concentration. However, at lower temperatures, there is less diffusion of charge across the junction and therefore a small depletion region exists between two layers of opposite charge, which can contribute to gas response.

Figure 3.40 again shows the influence of the bottom layer composition of the bi-layer thin films on gas response by exchanging the bottom layer from W-doped TiO_2 to pure TiO_2 and maintaining the top layer as Ni-doped TiO_2. It can be seen here that the bottom layer is much more influential on the sensing response when the top layer is Ni-doped compared with the W-doped top layer. When the bottom layer is a strong n-type (W-doped) then the film behaves as an n-type sensor, however, when the bottom layer is a weak n-type (pure TiO_2) the film shows good p-type response. This indicates that the charge carrier concentration of the semiconductor bi-layers can significantly influence the sensing behavior.

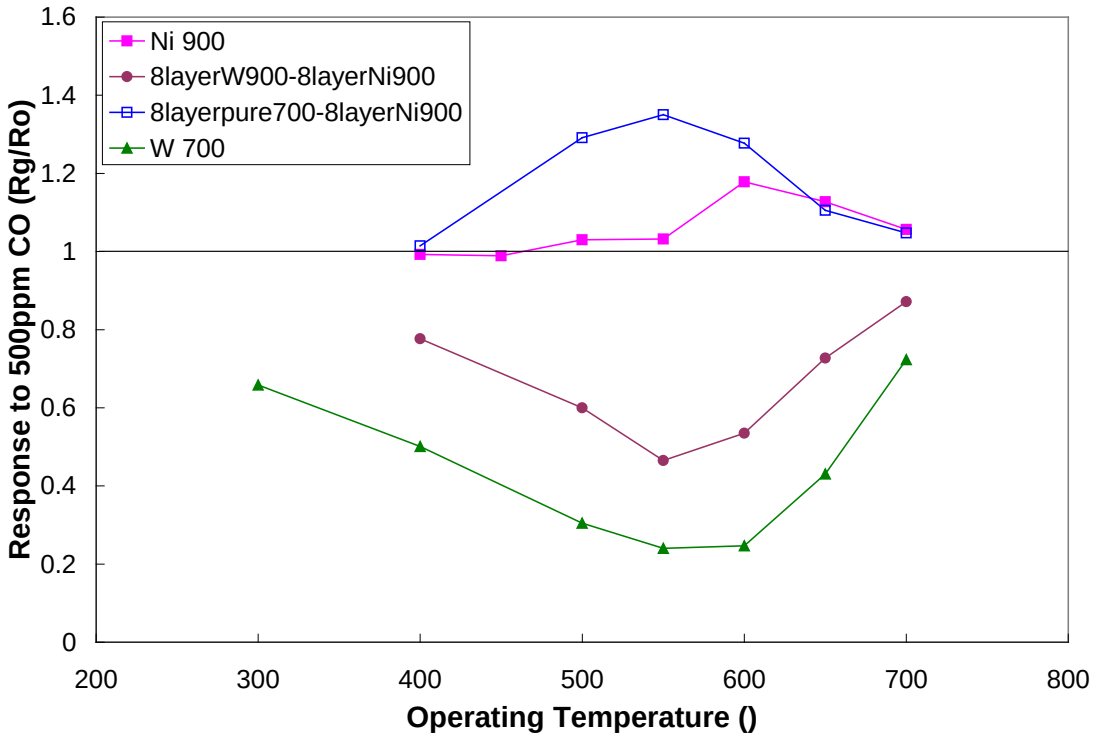

Figure 3.40. CO gas response for bi-layer films with Ni-doped TiO_2 on the top layer, and either W-doped TiO_2 or pure TiO_2 on the bottom layer.

CHAPTER FOUR

DISCUSSION

4.1 TiO_2 Thick Film Crystallinity

The gas sensitivity of MOS sensors such as SnO_2 and TiO_2 toward gasses other than oxygen has been found to be primarily a surface sensitive mechanism, as described in Chapter 1. Because oxygen ion adsorbtion sites on the surface are a major controlling factor for sensitivity, controlling the number of these sites is of significant interest. Two ways to increase the amount of oxygen adsorbed on the MOS surface are to either increase the surface area by decreasing the particle size, or increase the density of sites on the surface.

Much effort has been devoted to understand the effects of increasing surface area, decreasing particle size, smaller neck formation, and particle morphology on the sensing characteristics of TiO_2 and other MOS sensors [Li ’99, Rothschild ’04, Xu ’91, Wang ’95, Kim ’06, Mor ‘06]. It is the general consensus from theoretical and experimental research on metal-oxide gas sensor materials, such as SnO_2 and TiO_2, that reduction in particle size plays a significant role in enhancing sensitivity to reducing gasses. In fact, when the crystallite size is below about 80 nm, it has been shown that sensitivity is directly proportional to 1/D, where D is the crystallite diameter. Increase in surface area allows more oxygen to adsorb and desorb while reacting with reducing target gasses.

Aside from increasing the surface area as stated above, increasing the concentration of sites on the surface is another method for improving sensitivity which has received far fewer studies. The stoichiometry and defects on the MOS surface control the adsorption site density. Annealing the MOS can improve the gas adsorption by improving crystallinity, making the

surface defects more distinct and reactive with the target gas. This process, however, will also lead to grain growth and a reduction in surface area, and therefore optimization of the processing conditions is necessary.

It has recently been shown that higher annealing and sintering temperatures for metal-oxide thick film sensors can improve the gas sensing response via altering the gas adsorption kinetics and concentration of adsorption sites [Ruiz ’03, More ’03, Koziej ‘07]. These elevated temperatures lead to more necking between particles and reduced surface area which are two factors known to hinder sensing response. Necking between particles can lead to a conduction path that is not dependent on the depletion layer. Resistance between particles with a neck between them is not influenced by the gas composition and this causes reduced gas sensitivity. Reduced surface area hinders the sensing properties by limiting the amount of surface-gas reactions that take place. It is recognized that optimizing such processing parameters for each sensing material is necessary to achieve a compromise between high surface area and efficient gas interaction to maximize gas response [Korotcenkov ’05, Ahn ‘04]. An improved understanding of which material properties are being strongly affected by the heat treatment temperatures will provide insight into the sensing mechanism and knowledge of which properties can be engineered to enhance sensitivity.

In order to understand the role of TiO_2 crystallinity in thick film gas sensors, we chose to synthesize our own TiO_2 nano-powder via the citrate-nitrate method, which allowed us to control the crystallinity of the powder with the calcination temperature. An in-depth analysis using the characterization techniques XRD, BET, and TEM, provided conclusive evidence that higher calcination temperature increased particle and crystallite sizes of pure anatase TiO_2 powders. For every 100°C increase in calcination temperature, the surface area was reduced by approximately

half, which agrees with similar results that have been reported [Chen '03]. Based on the popular idea that gas response is strongly dependent on surface area, this would suggest that the sensitivity would get worse as the calcination temperature increased. However, sensing results displayed in Figure 3.8 conclusively show that increased heat treatement temperatures, both calcination and sintering, from 700 to 800°C improve the sensitivity of TiO_2 towards CO. As stated previously, this paradox has been reported and attributed to improved gas adsorption/desorption efficiency from the materials surface, however, few results are given that focus on which material properties could be causing this improvement.

The DSC results in Figure 3.6 provide some insight into the changes occuring in the material during heat treatment. First, obtaining pure anatase TiO_2 powders with high crystallinity, small grain size, and no rutile phase is difficult due to the formation of rutile while anatase is still crystallizing [Chen '03]. This occurance is displayed by the overlaping nature of the two exothermic crystallization peaks of anatase and rutile in the DSC plot. Combining this result together with the fact that no rutile had begun to form, we can conclude that anatase was still crystallizing at temperatures below 900°C and thus some amorphous material was present in the sample. Second, from a thermodynamic view of crystallization, anatase first nucleates on the surfaces of amorphous particles with an activation energy of 147kJ/mol and is then followed by three simaltaneous processes [Zhang '02]: (1) crystallization of amorphous particles onto the surface of anatase crystals at 78kJ/mol, (2) recrystallization of a smaller anatase crystal onto a larger crystal also at 78kJ/mol, and (3) anatase coarsening at 69kJ/mol. The similarity in the activation energies for these processes suggests that they will overlap each other in the temperature range and occur simultaneously during crystallization, suggesting amorphous material could still be present during the coarsening stage of crystallization.

To qualitatively asses the amount of amorphous material present, the area under the anatase peak was measured as a function of calcination temperature. As shown in Figure 3.6, the DSC plot for TiO_2 calcined at 700°C resulted in an anatase crystallization peak area of 11.2μV/mg. The measured area, as well as the visual size, of this peak decreased with increasing calcination temperature down to 1.5μV/mg for powders calcined at 900°C. These values suggest a significant portion of the crystallization processes mentioned above occurred at temperatures greater than 700°C in our TiO_2 powder.

During the sintering process of forming thick films, further changes in the particle size and crystallinity are possible, however, these changes will be minimal if the sintering temperature is kept at or lower than the calcination temperature. As seen in Figure 3.7, the final particle size is similar whether the highest temperature was reached during the calcination or sintering processes. However, calcination and sintering both at high temperature resulted in the largest particles due to the extended time at this temperature. The consequence of sintering, which is considered most influencial on sensing response, is the formation of necks between nanoparticles. It has been shown that neck size should be minimized whenever possible to maximize sensor response [Wang ’95], because necks provide a conduction path that is not dependent on the surface depletion layer of the particles as shown in Figure 4.1. From the FE-SEM micrographs in Figure 3.7, it can be concluded that higher sintering temperatures increase grain size with a slight increase in neck formation. Both of these microstructure changes are known to negatively effect sensing. However, results in Figure 3.8 show that an increase in sintering temperature from 700 to 800°C clearly enhanced the response to CO. This result again suggests that some other material property was responsible for the improvement in sensing response.

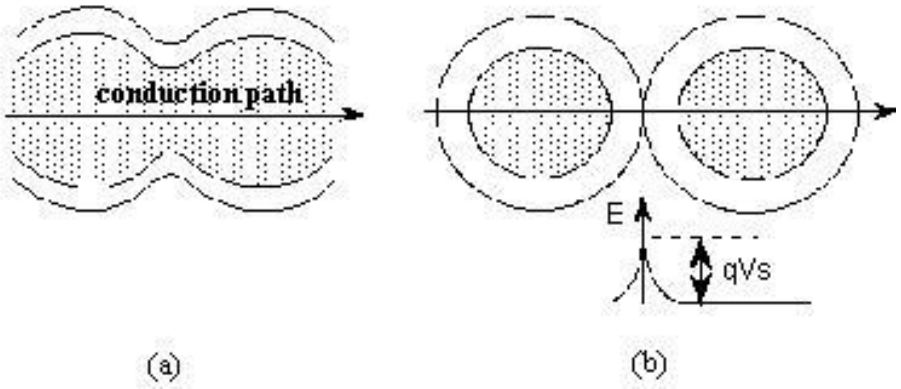

Figure 4.1. Diagram showing the conduction path through TiO_2 particles which (a) have necks formed between them, and (b) have a depletion layer forming a conduction barrier between particles. Figure taken from: Sheikh A Akbar and Prabir K. Dutta, "Ceramic Sensors for Industrial Applications," NSF Center for Industrial Sensors and Measurements (CISM).

Focusing on the effects of heat treatment temperatures on particle size, crystallite size, surface area, and film microstructure, it can be seen that increasing either the calcination and/or sintering temperatures negatively influenced many of the critical material properties associated with high gas sensitivity. By eliminating these properties as reasons for the measured improved response with increased heat treatment temperatures, it is clear that there must be another critical material property associated with the gas sensing mechanism. Thus, it is hypothesized here that crystallinity, i.e. the amount of crystalline anatase in a TiO_2 powder containing both crystalline and amorphous material, influences adsorption and desorption of oxygen on the surface of the TiO_2.

Taking into account the popular scheme for the solid state nucleation processes [Stojanovic '00], nucleation can either occur at a point on the surface or in the volume of the particle. In either scenario, until crystallization is complete, it is likely that any amorphous material present will be located near the surface of the particle. Given that the sensing mechanism of TiO_2 is dominated by surface reactions, the reactivity of this amorphous content

will play an influencial role in the response of the sensing element. It has been suggeseted the surface energy of amorphous phase TiO_2 will be less than that of crystalline anatase [Zhang '02, Hoang '08, Barnard '04]. It is speculated that lower surface energy will cause fewer oxygen ions to adsorb on the surface of the TiO_2 particles, thus resulting in a lower response to reducing gasses.

Our results show that disorder in the crystalline structure of nano TiO_2 particles can degrade sensor response even when the surface area is high. It is also evident that processing history has little effect on influence of crystallinity i.e., the amorphous to crystalline transformation can be done during the calcination stage or during sintering and in both cases response towards CO is improved. Moreover, for CO sensing of TiO_2 nanoparticles, crystallization was a more dominant factor in the early stages, i.e., up to 800 ^{o}C. However, once the TiO_2 nano-particles were sufficiently crystallized, surface area began to dominate the sensing behavior.

4.2 Pure TiO_2 Thin Films

Thin films composed of pure TiO_2 were fabricated via the spin coating of sol-gel from isopropoxide starting reagents. Analysis from both DSC and XRD results conclusively agree that anatase is crystallizing between the temperatures of 600 to 800°C, and the anatase-to-rutile transformation is taking place between 800 and 1000°C. Our films show high anatase thermal stability compared with other thin films which show rutile formation at lower processing temperatures [Epifani '08, Wenbin '08, Mohammadi '08, Gao '08]. These results indicate the potential for these films to show good sensing properties at higher operating temperatures.

Results from both UV-VIS and activation energy suggest that with increasing calcination temperature, it is possible that deeper and more defined defects are created in the electronic band gap, as depicted in Figure 4.2. With increasing calcination temperature, the activation energy (E_A) increases in the anatase phase but rutile formation at 900°C causes a small decrease. Also with increasing calcination temperature the material absorbs to higher visible wavelengths, indicating deeper defects. Therefore the overall trend is to achieve defects which are closer to the Fermi energy with increasing calcination temperature caused by a higher order in the crystal structure and a closer resemblance to defects of single crystal TiO_2. The crystal structure will also affect the size of the band gap (E_g). For instance, rutile has a smaller band gap than anatase therefore the band gap of the film calcined at 900°C will most likely be smaller than that of the films calcined at lower temperatures. From these experiments we have not directly measured the band gap and suffice it to say that they may change with crystallization. We have shown, however, that the depths of the donor sites are dependent on the crystallinity.

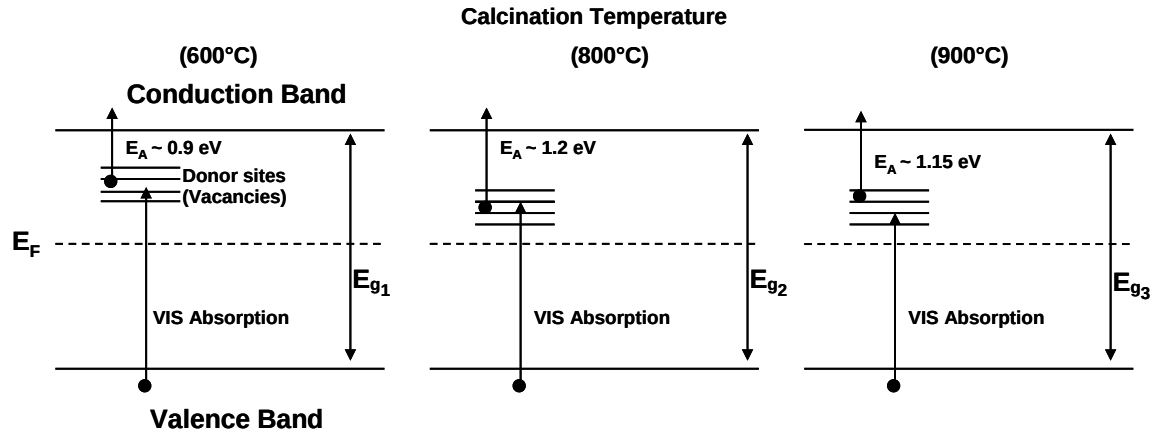

Figure 4.2. Hypothesized band structure change with increasing calcination temperature. $E_{g1} \neq E_{g2} \neq E_{g3}$

It is the author's hypothesis that point defects in a highly crystalline lattice are more defined resulting in distinct donor levels in the band gap. As the lattice becomes less defined and

more amorphous, the electronic band structure is less defined leading to donor sites which are closer to the conduction band. This explanation is consistent with the thick film results that higher crystallinity leads to better sensing due to formation of more defined defects.

Similar to the results of thick films, increased crystallization temperature of thin films induced more grain and particle growth, lower surface area, and phase change all which would lead to reduced the gas response, however defect formation improved with higher calcination temperatures which could improve gas response. Just like thick films, these competing factors lead to an optimum calcination temperature for maximum gas response, however for pure TiO_2 thin films that optimum temperature is 650°C compared with 800°C for thick films. This lower optimum temperature for thin films is attributed to the lower energy required for crystallization of the films. There is less material to crystallize in thin films compared with thick films, and the heat has less distance to travel during crystallization, therefore thin films reach a higher degree of crystallization in less time and at lower temperatures.

Even though thin films crystallized at lower temperatures, they displayed stable behavior at high temperatures and high sensitivity toward carbon monoxide. Selectivity toward CO with respect to CH_4 was found to be dependent on operating temperature, indicating that different thermal energies are required for reaction with the two gasses. These films show promise for stable operation of thin film sensing elements at high operating temperatures and the potential for selectivity toward CO.

4.3 TiO_2 Thin Film Chemistry

Chemical modification of TiO_2 via the addition of select dopants appears to be a promising technique to improve the sensing dependent material properties. Depending on the

ionic radius, valence, and chemistry, dopants (Nb^{5+}, La^{3+}, Cu^{2+}, W^{6+}, and Ni^{2+}) have shown to stabilize the highly sensitive anatase phase, reduce particle and grain growth, influence the charge carrier type and concentration, as well as change the surface reactivity [Savage '01, Anukunprasert '05, Sberveglieri '00, Garzella '03, Wisitsoraat '09]. Correlating the influence of each dopant on the material properties and the sensing performance of TiO_2 will improve the scientific understanding of the sensing mechanism and lead toward improving the sensing properties.

W^{6+} and Ni^{2+} dopants were chosen in this work for several reasons. Each oxide is already known to be applicable as a high temperature gas sensing material [Hotovy '01, Azad '06]. These ions are also similar in size to Ti^{4+} and have been shown to form substitutional defects in the TiO_2 lattice [Wisitsoraat '09, Komornicki '04]. Where these ions differ in character and provide interesting contrast for study is in their valence charge. Substitution of W^{6+} or Ni^{2+} in the place of Ti^{4+} causes the formation of excess electron (e^-) or hole ($h^{\cdot}$) charge carriers, respectively, as shown in equations 4 and 5 in the introduction. Incorporation of these substitutional defects resulted in an increase in the traditional n-type conductivity for the case of W^{6+}, and an increase in p-type carriers for the case of Ni^{2+} substitution. Manipulating the conductivity of the material had a direct impact on the sensing behavior; however doping can cause a change in phase and microstructure which may have also affected the sensing behavior. This work focused on studying the different effects of W^{6+} and Ni^{2+} doping in TiO_2 on the material properties which affect the gas sensing response.

The addition of tungsten in TiO_2 thin films had similar effect on the crystal phase and grain sizes as we observed in thick films made from powder processing. A small amount of tungsten reduced the crystallinity and grain size, while a large concentration of tungsten

promoted crystallization and grain growth. From the thick film results we attributed this phenomenon to the solubility limit of tungsten in the TiO_2 lattice. A small amount of tungsten is able to dissolve in the TiO_2 lattice, however, with increasing concentration, WO_3 peaks were visible in the thick film XRD pattern. This secondary phase may be responsible for promoting crystallization. Thin film XRD patterns did not show any WO_3 peaks in the higher tungsten concentration films, which is most likely due to the weak diffraction signal caused by the dimension of the films. This influence of tungsten on the TiO_2 phase slightly affected the sensing properties as shown by the thick film sensing results. However, from the thin film results, it could be seen than the influence of tungsten on TiO_2 phase had minimal affect on the sensing properties compared with the affect of tungsten on electronic defects in TiO_2.

Baseline resistance decreased with increasing tungsten concentration for both thick and thin films and is attributed to the n-type substitutional defects. This trend is more clear and significant in the thin films for two reasons. First, thin film processing is more reproducible and will create films with lower porosity. Therefore the resistance of the film is more dependent on the film electronic properties rather than the film geometry and microstructure, such as the case in the thick films. Second, thin films were doped during crystallization whereas tungsten was added to thick films after the TiO_2 crystal structure was already formed (solid state diffusion). This likely resulted in a higher concentration of tungsten defects in the TiO_2 lattice of the thin films as the TiO_2 crystallized around the tungsten atoms rather than relying on the slow diffusion of tungsten into the lattice.

The major difference between W-doped TiO_2 thick and thin films was noticed in the gas sensing mechanism. In the thick films, tungsten concentration controlled the crystal phase, which in turn controlled the gas sensing properties. Tungsten concentration had no direct effect

on the gas sensing properties of thick films. In the case of W-doped thin films, we have found that tungsten concentration directly enhanced the gas sensing properties by creating electronic defects in the material. These electronic defects dominate any affect due to grain size, crystallinity, microstructure, or phase. The addition of tungsten allowed high gas response even when films were calcined at 900°C causing the formation of large rutile grains. This result further suggests that tungsten was incorporated into the TiO_2 crystal lattice better in the thin films compared with the thick films.

From our pure TiO_2 thin film results we can see that an increase in calcination temperature leads to increase in grain size, reduction in surface area, particle necking, and eventually phase change from anatase to rutile. These material property changes led to an overall reduction in gas response for pure TiO_2 thin films calcined at higher temperatures. We observed a similar trend in the material properties of the W-doped thin films, however, these changes did not lead to a reduction in the gas response. In fact, the 10%W thin film calcined at 900°C showed a large increase in particle size, significant necking between particles, and a complete phase transformation to rutile, and still showed high gas response. We attribute this difference in material property dependence between pure and W-doped thin films on the difference between intrinsic and extrinsic defects. As described earlier, the n-type gas response of TiO_2 is explained on the basis of oxygen vacancy formation:

$$2\mathrm{TiO}_2 \longrightarrow \mathrm{V_O}^{\bullet\bullet} + 2Ti_{Ti}^{x} + 3O_O^{x} + 2e^{-} + \frac{1}{2}O_2(g) \qquad (12)$$

Oxygen from the atmosphere adsorbs on the oxygen vacancy in the lattice and traps the electron. However, as was discussed earlier, the concentration of these lattice oxygen vacancies on the surface of the TiO_2 changes with the crystallinity, phase, and particle size of the material limiting

the gas reactivity as the calcination temperature increases. Addition of W^{6+} ions into the TiO_2 lattice creates similar defects to oxygen vacancies:

$$TiO_2 \xrightarrow{W} W_{Ti^{4+}}^{6+\bullet\bullet} + 2O_O^X + 2e^- \quad (13)$$

Equations (12) and (13) both produce positive pinned defects (oxygen vacancies or W substitution) associated with mobile negative defects (electrons). We found that the W-doped TiO_2 thin film gas response was not negatively affected by higher calcination temperatures. This result suggests that the extrinsic defects described in Equation (13) are not dependent on crystallinity, particle size, or material phase and were more dominant on the sensing mechanism than the intrinsic defects described in Equation (12).

W-doped thin films which were calcined at high temperatures (900°C) should show more long term stability during operation at high temperatures because they have already achieve a high degree of crystallinity and there is less driving force for annealing. Therefore, tungsten could be used to benefit the stability of the thin films while at the same time improving the gas response.

Addition of nickel in TiO_2 thin films had minimal influence on the grain and crystallite sizes, however a significant impact on the phase stability was noticed. Pure TiO_2 thin films did not start to form rutile until above 800°C while Ni-doped TiO_2 thin films started to form rutile below 600°C and the anatase-to-rutile phase transformation was complete by 800°C. There are several plausible reasons why the addition of nickel would promote the anatase-to-rutile transformation. First, even though no nickel oxide (NiO) phase was observed by XRD, it is possible a trace amount of this secondary phase could be present in the sample catalyzing rutile formation. Second, evidence from our data suggests that the addition of nickel creates 'hole' defects in the crystal structure which are more stable in the rutile phase. Finally, the addition of

nickel can also promote the formation of oxygen vacancies through charge compensation, shown in Equation (14):

$$TiO_2 \xrightarrow{Ni} Ni_{Ti^{4+}}^{2+\,''} + V_O^{\bullet\bullet} + O_O^X \qquad (14)$$

These vacancies are thought to improve the mass transport during heat treatments allowing an easier phase transformation [Reidy '06, Rath '09]. However, the exact mechanism by which the addition of nickel promotes rutile formation is still under debate [Lim '05, Gole '08, Li '09].

Addition of nickel also appears to lower the size of the band gap, as illustrated by the UV-VIS absorbance. This is possibly due to the 'hole' defects created by nickel substitution, however it is more likely caused by complete anatase-to-rutile transformation, where rutile has a smaller band gap than anatase. From the baseline resistance measurements, we can assume, however, that a significant concentration of 'hole' defects is present in the Ni-doped samples.

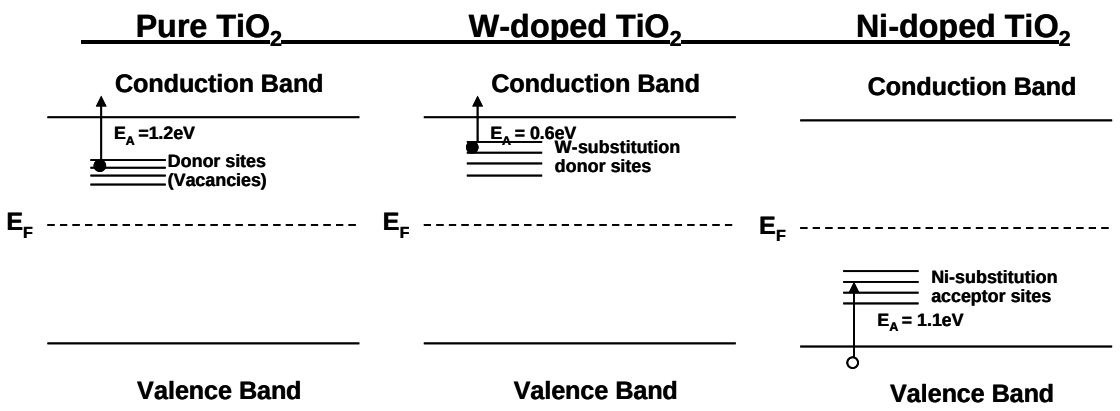

Figure 4.3. Band diagram for pure, W-doped, and Ni-doped TiO_2 thin films. Diagram shows the activation energy for electrons to move into the conduction band from defect sites for n-type pure and W-doped TiO_2, and holes to move from the valence band into the defect sites for p-type Ni-doped TiO_2.

Similar to tungsten, however, the most dramatic consequence of nickel doping in TiO_2 was noticed in the gas sensing mechanism. With high film calcination and operating temperatures, a very clear but unusual p-type gas response was noticed for Ni-doped TiO_2 thin films toward both CO and CH_4. This p-type response is unusual because TiO_2 is commonly

oxygen deficient, leading to n-type response. We attribute the need for high calcination temperature to successful incorporation of Ni atoms into the lattice and a complete anatase-to-rutile phase transformation resulting in p-type defects. The need for higher operating temperature is likely due to thermal energy required to excite electrons from the valence band to the acceptor sites and produce p-type conduction. Similar to the conclusions made for W-doped TiO_2, it is clear that under these conditions the extrinsic acceptor sites caused by Ni substitution is the dominant defect compared with the intrinsic donor sites.

Extrinsic defects caused by the incorporation of both tungsten and nickel have sensitized the rutile phase of TiO_2, creating the possibility to fabricate sensitive rutile-based gas sensors which are more stable than anatase sensors during high temperature operation. The extrinsic defects are also located at different energies in the TiO_2 band gap which may lead to variations in the bond strengths of adsorbed species and eventually to controlling the sensor selectivity.

4.4 Composite n-p TiO_2 Gas Sensors

In the previous sections we have shown that chemistry of TiO_2 thin films plays a more significant role in the gas sensing mechanism than crystallinity, and clearly produced TiO_2-based sensors with either n-type or p-type conduction and gas response. For an extension of this work we have fabricated bi-layer thin film p-n homojunctions of n-type W-TiO_2 and p-type Ni-TiO_2 to study the influence of these junctions on sensing performance.

In order to create a p-n junction with a depletion layer, it is necessary to have a p-type material in electrical contact with an n-type material. From the baseline resistance data we have shown that the two layers of our bi-layer films are in electrical contact because the electrodes are on the bottom layer and the resistance resembles the top layer. This indicates that electrical

conduction is occurring through the bottom layer into the top layer. However, a major concern with our bi-layer films is atomic diffusion during heat treatment. If the tungsten and nickel atoms diffuse across the junction, the defects will cancel and no longer form a distinct junction between p-type and n-type TiO_2. From EDAX analysis it is clear that the atomic concentration of tungsten is higher on the top half of the film and the nickel concentration is higher near the bottom half. Therefore, we can conclude that gradients of tungsten and nickel concentrations are occurring throughout the thicknesses of the bi-layer film, however the exact quantitative gradients and distance of ionic diffusion during crystallization are undetermined.

The baseline resistances of the bi-layer films offer some insight on the influence of layer compositions on electronic properties of the films. First, all films show lower resistance than the pure TiO_2 thin film. This signifies that the presence of a single p-n junction depletion region is not significantly increasing the film resistance. Instead, it is more likely that conduction is occurring through both layers; electrons through the n-type layer and 'holes' in the opposite direction through the p-type layer. This is a similar idea to the percolation paths proposed by Savage et al. [Savage '01]. It is possible that with a multilayer film containing multiple junctions, film resistance would be more dependent on the junctions. It is interesting to note, however, that the overall resistance of the bi-layer films most closely resembles the resistance of the top layer material composition. This signifies that, independent of layer composition, more conduction is occurring through the top layer compared with the bottom layer. One explanation for this result could be that the bottom layer is filling in the crevasses and pores of the rough alumina substrate and does not actually create a complete film. Then, the top layer has a smooth surface on which to be deposited and form as a complete conducting film and control the overall resistance. This hypothesis is supported by the results from Figure 3.14 (resistance vs. number of sol-gel layers).

Thinner films, such as the 8 layer, had much higher resistances that the fully formed 16 layer films, signifying that 8 layers was not sufficient to for a complete film.

Results from the gas response of bi-layer thin films show similar trends of the location and composition of layers as the resistance, i.e. the top layer controls the gas response more significantly than the bottom layer. This result can also be explained by the bottom layer filling the pores of the substrate and the top layer forming the complete uniform film. However, in addition to this effect, gas penetration into the film also gives an explanation. The geometry of the films is such that the electrodes are on the bottom and the gas exposure is on the top surface, therefore the gas first comes in contact with the outermost layer of the film and must penetrate any pores or cracks in the film before it comes in contact with the bottom layer. It is our hypothesis that the majority of the reactive carbon monoxide reacts with the adsorbed oxygen on the outer most layer when it first come into contact with the film. From the SEM images of the top surface of our thin films, we can see that the porosity is relatively low, therefore allowing minimal gas penetration into the film. Less gas is available to react with the bottom layer and, by the time it reaches this point, the majority has already reacted to form CO_2 and can no longer react with the adsorbed oxygen. This process leads to the top layer controlling the gas response of our bi-layer thin films. This result could be used to further enhance the design of future sensors.

It is evident from our bi-layer thin films that a clear p-n junction with a depletion region is most likely not forming between the two layers. This can be the result of two phenomena: ionic diffusion and charge mobility. Ionic diffusion of tungsten and nickel across the junction during the crystallization step could lead to a region with both dopants present. Lack of a sharp p-n junction would result in no depletion layer formation. These sensors are also operated at

high temperatures; therefore, even if a sharp p-n junction is present, the mobile charge carriers could have sufficient energy to traverse completely across the junction. It is possible that reduced processing and operating temperatures could lead to the formation of a sharp p-n junction and improve the TiO_2 thin film sensing characteristics; however this work has been left for future research.

In addition to possible diffusion and charge mobility forming an undefined junction, the design of our films is not applicable to measuring the voltage across the p-n junction. As shown in Figure 4.4, a standard p-n junction is useful in controlling current across the junction from p-type to n-type. However, due to film fabrication methods and electrode geometry in this study, the current bi-layer thin film design does not measure the junction voltage. Rather it measures the combined resistance of the two materials. It is left as a future work to redesign either the electrode configuration (such as top and bottom electrodes) or the film fabrication (such as patterning) to create a sensor which operates based on the voltage across the p-n junction.

Finally, this work has barely scratched the surface of potential research in n-p composite sensors. We have shown that an elemental concentration gradient is achievable in thin films even after crystallization heat treatments. Based on the present findings, it is quite clear that use of these materials in a successful design could result in fruitful advancements in the sensor properties.

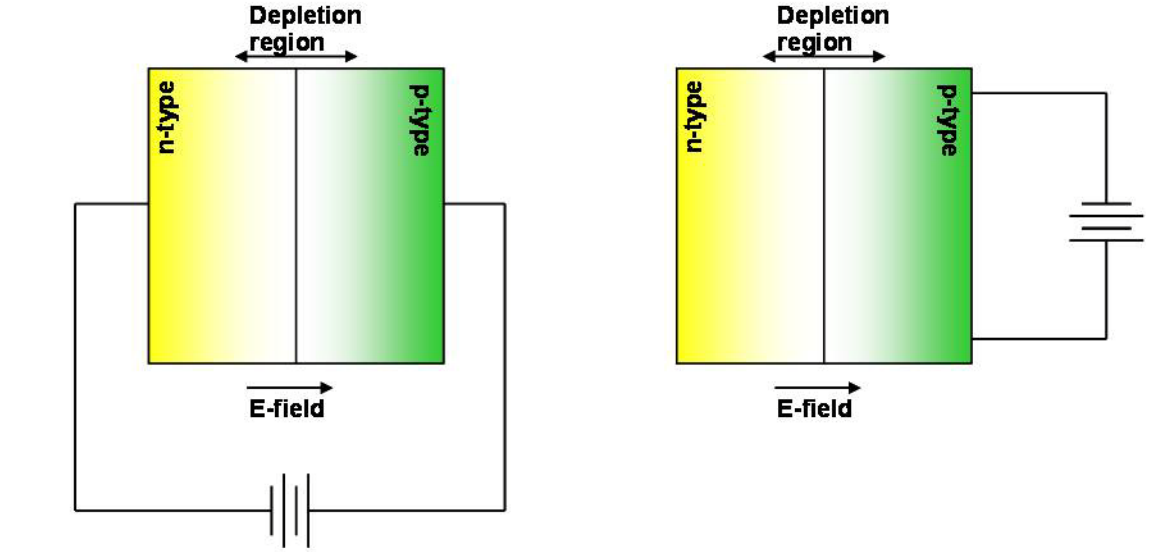

Figure 4.4. Diagram of a p-n junction used with a standard forward bias and design used in the current bi-layer thin films of this work.

4.5. Summary

The objective of this research was to study the influence of crystallinity and chemistry of TiO_2 films on their gas sensing properties such as **sensitivity**, **selectivity**, and **high temperature stability** in order to gain scientific understanding of the sensing mechanism and functionality of the films. Some of the general conclusions from this research are:

- Both thick particulate (30 µm) and thin sol-gel (1µm) TiO_2-based films created on an electroded alumina substrate showed **stable** and reproducible gas sensing response at high operating temperatures (600°C).

Thick Film Conclusions

- Optimization between a high degree of crystallinity and minimal grain growth produced the best gas response operating at 600°C for both types of films; however, thin films crystallized at lower temperatures (650°C) than thick films (800°C).

- Addition of up to 5 wt.% WO_3 in TiO_2 thick films had minimal effect on the electronic and sensing properties but did influence the crystallization behavior and grain sizes to some degree. 1 wt.% WO_3 hindered crystallization and grain growth, while 5 wt.% WO_3 promoted the anatase-to-rutile phase transformation and increased grain growth.
- Chemistry of thick films did not have any direct impact on the gas **sensitivity**. Rather, chemistry influenced the crystallinity which in turn controlled the gas response.

Thin Film Conclusions

- All TiO_2 thin films were more **selective** toward CO than CH_4.
- Addition of 2.5 and 5 at.% tungsten in TiO_2 thin films hindered crystallization and grain growth while 10 at.% tungsten promoted both. Addition of tungsten promoted a significant increased the n-type conduction and decreased film resistance by up to 30 times. N-type gas **sensitivity** was improved by nearly two times with tungsten addition.
- 10 at.% W-doped TiO_2 thin films showed a high sensitivity to CO even after calcination at 900°C indicating significant potential for **long term stability** during high temperature operation.
- Addition of nickel in TiO_2 thin films strongly promoted the anatase-to-rutile phase transformation and changed the material to show predominantly **p-type conduction** and gas response.
- Addition of both tungsten and nickel increase the optimal **operating temperature** for CO gas response from 450°C for pure TiO_2 to 600°C for doped TiO_2 thin films.
- Tungsten doping created donor sites approximately 0.6 eV below the conduction band while nickel doping created acceptor sites approximately 1.1 eV above the valence band.

These **extrinsic defects** in the electronic band gap of TiO_2 had a more significant impact on the electrical and gas sensing properties than did microstructure or crystallinity.

- Formation of p-n composite bi-layer thin films was unsuccessful in enhancing the gas response; however, the order of the layers provided evidence that the majority of the gas-surface reaction took place on the **outer layer** of the film.
- The current work gave only a brief first look at the influence of p-n junctions on gas sensing properties. Further research, including an improved electrode design, is necessary to fully understand the influence of p-n junctions on gas sensing behavior of TiO_2 thin films.

From these results it can be concluded that addition of tungsten and nickel in TiO_2 thin film sensors can be used to tailor the electrical properties and gas response toward CO; a result that can have direct impact towards improving sensitivity, selectivity, and stability of high operating temperature gas sensors.

References

1. Ahn J., Kim J., Park J., Huh M., “Microstructure and gas-sensing properties of thick film sensor using nanophase SnO2 powder,” Sens. Act. B Chem., 99 (2004) 18-24.

2. Akasheh F., Myers T., Fraser J., Bose S., Bandyopadhyay A., "Development of piezoelectric micromachined ultrasonic transducer," Sens. Act. A, 111 (2004) 275-287.

3. Akbar S., Dutta P., Lee C., “High-temperature ceramic gas sensors: A review,” Int. J. Appl. Ceram. Technol. 3 (2006) 302-311.

4. Alessandri I., Comini E., Bontempi E., Faglia G., Depero L., Sberveglieri G., “Cr-inserted TiO_2 thin films for chemical gas sensors,” Sens. Act. B Chem., 128 (2007) 312-319.

5. Al-Homoudi, Rimai L., Baird R., Naik R., Auner G., Newaz G., “Anatase TiO2 thin film based CO gas sensor,” Mater. Res. Soc. Symp. Proc., 888 (2006) V03-08.1.

6. Anukunprasert T., Saiwan C., Traversa E., The development of gas sensors for carbon monoxide monitoring using nanostructure of Nb-TiO2,” Sci Technol. Adv. Mater., 6 (2005) 359-363.

7. Aygun S., Cann D., “Response kinetics of doped CuO/ZnO heterocontacts,” J. Phys. Chem. B 109 (2005) 7878-7882.

8. Aygun S., Cann D., “Hydrogen sensitivity of doped CuO/ZnO heterocontact sensors,” Sens. Act. B Chem., 106 (2005) 837-842.

9. Azad A., Hammoud M., “Fine-tuning of ceramic-based chemical sensors via novel microstructural modification I: low level CO sensing by tungsten oxide, WO3,” Sens. Act. B Chem., 119 (2006) 384-391.

10. Bandyopadhyay A., Aswath P., Porter W., Cavin O., “The low temperature hexagonal to orthorhombic transformation in Si_3N_4 reinforced BAS matrix composites,” J. Mater. Res., 10 (1995) 1256-1263.

11. Banno S., Imanaka N., Adachi G., “Selective nitrogen sensors based on nickel copper oxide mixed with rare earths,” Sens. Act. B Chem., 24 (1995) 619-622.

12. Barnard A., Zapol P., “Effects of particle morphology and surface hydrogenation on the phase stability of TiO2,” Phys. Rev. B, 70 (2004) 235403-235416.

13. Barsoum M., “Fundamentals of Ceramics,” Institute of Physics Publishing, Philadelphia (2003) pp. 80-84.

14. Birkefeld L., Azad A., Akbar S., “Carbon monoxide and hydrogen detection by anatase modification of Titanium dioxide,” J. American Ceramic Society, 75 (1992) 2961-2968.

15. Bogdanov P., Ivanovskaya M., Comini E., Faglia G., Sberveglieri G., “Effect of nickel ions on sensitivity of In2O3 thin film sensors to NO2,” Sens. Act. B Chem., 57 (1999) 153-158.

16. Brilis N., Foukaraki C., Bourithis E., Tsamakis D., Giannoudakos A., Kompitsas M., Xenidou T., Boudouvis A., “Thin Solid Films 515 (2007) 8484-8489.

17. Brinzari V., Korotcenkov G., Golocanov V., “Factors influencing the gas sensing characteristics of tin dioxide films deposited by spray pyrolysis: understanding and possibilities of control,” Thin Solid Films 391 (2001) 167-175.

18. Carotta M., Gherardi S., Malagu C., Nagliati M., Vendemiati B., Martinelli G., Sacerdoti M., Lesci I., “Comparison between titania thick films obtained through sol-gel and hydrothermal synthetic processes,” Thin Solid Films, 515 (2007) 8339-8344.

19. Chaudhari G., Bende A., Bodade A., Patil S., Sapkal V., “Structural and gas sensing properties of nanocrystalline TiO2:WO3-based hydrogen sensors,” Sens. Act. B Chem., 115 (2006) 297-302.

20. Chen Y., Lee C., Yeng M., Chiu H., “The effect of calcination temperature on the crystallinity of TiO2 nanopowders,” J. Cryst. Growth 247 (2003) 363-370.

21. Choi Y., “Synthesis and characterization of titanium dioxide based nanostructured ceramics for gas sensor” Masters Thesis at Washington State University (2004).

22. Choi Y., Seeley Z., Bandyopadhyay A., Bose S., Akbar S., “Aluminum-doped TiO_2 nano-powders for gas sensors,” Sens. Act. B Chem., 124 (2007) 111-117.

23. Comini E., Sberveglieri G., Guidi V., “Ti-W-O sputtered thin films as n- or p-type gas sensors,” Sens. Act. B Chem., 70 (2000) 108-114.

24. Cullity B., Weymouth J., “Elements of X-ray diffraction,” 2nd Ed., Addison-Welsey, (1978) pp. 284-285.

25. Dandeneau C., Jeon Y., Shelton C., Plant T., Cann D., Gibbons B., “Thin film chemical sensors based on p-CuO/nZnO heterocontacts,” Thin Solid Films 517 (2009) 4448-4454.

26. Demetry C., Shi X., “Grain size-dependent electrical properties of rutile (TiO2),” Solid State ionics 118 (1999) 271-279.

27. Ding X., Liu X., “Grain growth enhanced by anatase-to-rutile transformation in gel-derived nanocrystalline titania powders,” J. Alloys and Compounds, 248 (1997) 143-145.

28. Ding X., Liu X., “Correlation between anatase-to-rutile transformation and grain growth in nanocrystalline titania powders,” J. Mater. Res., 13 (1998) 2556-2559.

29. Dutta P., Ginwalla A., Hogg B., Patton B., Chwieroth B., Liang Z., Gouma P., Mills M., Akbar S., "Interaction of carbon monoxide with anatase surfaces at high temperatures: optimization of a carbon monoxide sensor," J. Phys. Chem. B, 103 (1999) 4412-4422.

30. Dutta P., Frank M., Hunter G., George M., "Reactively sputtered titania films as high temperature carbon monoxide sensors," Sens. Act. B Chem., 106 (2005) 810-815.

31. Epifani M., Helwig A., Arbiol J., Diaz R., Francisco L., Siciliano P., Mueller G., Morante J., "TiO2 thin films from titanium butoxide: synthesis, Pt addition, structural stability, microelectronic processing and gas-sensing properties," Sens. Act. B Chem., 130 (2008) 599-608.

32. Ferroni M., Carotta M., Guidi V., Martinelli G., Ronconi F., Richard O., Van Dyck D., Van Landuyt J., "Structural characterization of Nb-TiO2 nanosized thick-films for gas sensing application," Sens. Act. B Chem., 68 (2000) 140-145.

33. Gaggiotti G., Galdikas A., Kaciulis S., Mattogno G., Setkus A., Surface chemistry of tin oxide based gas sensors," J. Appl. Phys., 76 (1994) 4467-4471.

34. Galatsis K., Li Y., Wldarski W., Comini E., Faglia G., Sberveglieri G., "Semiconductor MoO3-TiO2 thin film gas sensors," Sens. Act. B Chem., 77 (2001) 472-477.

35. Gao S., Xian A., Cao L., Xie R., Shang J., "Influence of calcination temperature on potoresponse of TiO2 film under nitrogen and oxygen in room temperature," Sens. Act. B Chem., 134 (2008) 718-726.

36. Garzella C., Bontempi E., Depero L., Vomiero A., Della Mea G., Sberveglieri G., "Novel selective ethanol sensors: W/TiO2 thin films by sol-gel spin coating," Sens. Act. B Chem., 93 (2003) 495-502.

37. Gole J., Prokes S., Glembocki O., "Efficient room-temperature conversion of anatase to rutile TiO2 induced by high-spin ion doping," J. Phys. Chem. C, 112 (2008) 1782-1788.

38. Gopel W., Dieter Schierbaum K., "SnO_2 sensors: current status and future prospects," Sens. Act. B Chem., 26-27 (1995) 1-12.

39. Hansen J., Nazarenko L., Ruedy R., Sato M., Willis J., Del Genio A., Koch D., Lacis A., Lo K., Menon S., Novakov T., Perlwitz J., Russell G., Schmidt G., Tausnev N., "Earth's energy imbalance: confirmation and implications," Science 308 (2005) 1431-1435.

40. Hansen J., Sato M., Ruedy R., Lo K., Lea D., Medina-Elizade M., "Global temperature change," Proc. Nat. Acad. Sci., 103 (2006) 14288-14293.

41. Hazra S., Basu S., "Hydrogen sensitivity of ZnO p-n homojunctions," Sens. Act. B Chem., 117 (2006) 177-182.

42. Hitchman M., Tian F., “Studies of TiO2 thin films prepared by chemical vapour deposition for photocatalytic and photoelectrocatalytic degredation of 4-chlorophenol,” J. Electroanalytical Chem., 538 (2002) 165-172.

43. Hoang V., “The glass transition and thermodynamics of liquid and amorphous TiO2 nanoparticles,” Nanotechnology 19 (2008) 105706-105718.

44. Hotovy I., Huran J., Siciliano P., Capone S., Spiess L., Rehacek V., “The influences of preparation parameters on NiO thin film properties for gas-sensing application,” Sens. Act. B Chem., 78 (2001) 126-132.

45. Hu Y., Tsai H., Huang C., “Phase transformation of precipitated TiO2 nanoparticles,” Mater. Sci. Eng. A, 344 (2003) 209-214.

46. Huber B., Brodyanski A., Scheib M., Orendorz A., Ziegler C., Gnaser H., “nanocrystalline anatase TiO2 thin films: preparation and crystallite size-dependent properties,” Thin Solid Films 472 (2005) 114-124.

47. Hunter G., Neudeck P., Liu C., Ward B., Wu Q., Dutta P., “Development of chemical sensors arrays for harsh environments and aerospace applications,” Proc. IEEE Sensors (2002) 1126-1133.

48. Huusko J., Lantto V., Torvela H., “TiO2 thick-film gas sensors and their suitability for NOx monitoring,” Sens. Act. B Chem., 16 (1993) 245-248.

49. Hwang K., Jeong J., Ahn J., Kim B., “Hydrophilic/hydrophobic conversion of Ni-doped TiO2 thin films on glas substrates,” Ceramics International 32 (2006) 935-937.

50. Katti V., Debnath A., Muthe K., Manmeet M., Dua A., Gadkari S., Gupta S., Sahni V., “Mechanism of drifts in H2S sensing properties of SnO2:CuO composite thin film sensors prepared by thermal evaporation,” Sens. Act. B Chem., 96 (2003) 245-252.

51. Kim I., Rothschild A., Lee B., Kim D., Jo S., Tuller H., “Ultrasensitive chemiresistors based on electrospun TiO2 nanofibers,” Nano Lett. 6 (2006) 2009-2013.

52. Knauth P., Tuller H., “Electrical and defect thermodynamic properties of nanocrystalline titanium dioxide,” J. Appl. Phys., 85 (1999) 897-902.

53. Knorr F., Mercado C., McHale J., “Trap-state distributions and carrier transport in pure and mixed-phase TiO2: Influence of contacting solvent and interphasial electron transfer,” J. Phys. Chem., C 112 (2008) 12786-12794.

54. Kofstad P., “Nonstoichiometry, diffusion, and electrical conductivity in binary metal oxides,” Wiley-Interscience (1972) pp. 137-152.

55. Kohl D., “Function and applications of gas sensors,” J. Phys. D: Appl. Phys., 34 (2001) R125-R149.

56. Komornicki S., Radecka M., Sobas P., “Structural, electrical and optical properties of TiO2-WO3 polycrystalline ceramics,” Mater. Res. Bull., 39 (2004) 2007-2017.

57. Korotcenkov G., “Gas response control through structural and chemical modification of metal oxide films: state of the art and approaches,” Sens. Act. B Chem., 107 (2005) 209-232.

58. Korotcenkov G., “Practical aspects in design of one-electrode semiconductor gas sensors: status report,” Sens. Act. B Chem., 121 (2007) 664-678.

59. Koziej D., Thomas K., Barsan N., Thibault-Starzyk F., Weimar U., “Influence of annealing temperature on the CO sensing mechanism for tin dioxide based-Operando studies,” Catal. Today 126 (2007) 211-218.

60. Li G., Zhang X., Kawi S., “Relationships between sensitivity, catalytic activity, and surface areas of SnO2 gas sensors,” Sens. Actuators, B, Chem. 60 (1999) 64-67.

61. Li S., Jena P., “Origin of the anatase to rutile conversion of metal-doped TiO2,” Phys. Rev. B, 79 (2009) 201204.

62. Li Y., Wlodarski W., Galatsis K., Moslih S., Cole J., Russo S., Rockelmann N., “Gas sensing properties of p-type semiconducting Cr-doped TiO2 thin films,” Sens. Act. B Chem., 83 (2002) 160-163.

63. Lim Y., Jeong J., An J., Jeon Y., Jeon K., Hwang K., Kim B., “Nickel-doped titanium oxide films prepared by chemical solution deposition,” J. Ceram. Proc. Res. 6 (2005) 302-304.

64. Linsebigler A., Lu G., Yates J., “Photocatalysis on TiO2 surfaces: principles, mechanisms, and selected results,” Chem. Rev., 95 (1995) 735-758.

65. Luyo C., Ionescu R., Reyes L., Topalian Z., Estrada W., Llobet E., Granquist C., Heszler P., “Gas sensing response of NiO nanoparticles films made by reactive gas deposition,” Sens. Act. B Chem., 138 (2009) 14-20.

66. Mandelis A., “Physics, chemistry, and technology of solid state gas sensor devices,” Wiley-Interscience (1993) pp. 47-56.

67. Mardare D., Iftimie N., Luca D., “TiO2 thin films as sensing gas materials,” J. Non-Crystalline Solids 354 (2008) 4396-4400.

68. Meixner H., Lampe U., “Metal oxide sensors,” Sens. Act. B Chem., 33 (1996) 198-202.

69. Menetrey M., Markovits A., Minot C., Reactivity of a reduced metal oxide surface: hydrogen, water and carbon monoxide adsorption on oxygen defective rutile TiO2 (110),” Surface Science 524 (2003) 49-62.

70. Mo S., Ching W., Electronic and optical properties of three phases of titanium dioxide: Rutile, anatase, and brookite," Physical Rev. B, 51 (1995) 13023-13032.

71. Mochinaga R., Yamasaki T., Arakawa T., "The gas-sensing of SmCoOx/MOx (M=Fe,Zn,In,Sn) having a heterojunction," Sens. Act. B Chem., 52 (1998) 96-99.

72. Mohammadi M., Fray D., "Semiconductor TiO2-Ga2O3 thin film gas sensors derived from particulate sol-gel route," Acta Materialia 55 (2007) 4455-4466.

73. Mohammadi M., Fray D., Ghorbani M., "Comparison of single and binary oxide sol-gel gas sensors based on titania," Solid State Sciences, 10 (2008) 884-893.

74. Moos R., "A brief overview on automotive exhaust gas sensors based on electroceramics," Int. J. Appl. Ceram. Technol., 2 (2005) 401-413.

75. Mor G., Oomman V., Paulouse M., Ong K., Grimes C., "Fabrication of hydrogen sensors with transparent titanium oxide nanotube-array thin films as sensing elements," Thin Solid Films 496 (2006) 42-48.

76. More P., Khollam Y., Deshpande S., Date S., Karekar R., Aiyer R., "Effect of variation of sintering temperature on gas sensing characteristics of SnO2:Cu(Cu=9wt.%) system," Mater. Lett. 58 (2003) 205-210.

77. Myers T., Banerjee P., Bose S., Bandyopadhyay A., "Layered PZT and PLZT Ceramic Thin Films," J. Mater. Res., 17 (2002) 2379-86.

78. Nakamura Y., Ando A., Tsurutani T., Okada O., Miyayama M., Muomoto K., Yanagida H., "Gas sensitivity of CuO/ZnO Hetero-contact," Chem. Lett., (1986) 413-416.

79. Nakamura Y., Yoshioka H., Miyayama M., Yanagida H., Tsurutani T., Nakamura Y., "Selective CO gas sensing mechanism with CuO/ZnO heterocontact," J. Electrochem. Soc. 137 (1990) 940-943.

80. Nakamura Y., Zhuang H., Kishimoto A., Okada O., Yanagida H., "Enhanced CO and CO2 gas sensitivity of the CuO/ZnO heterocontact made by quenched CuO ceramics," J. Electrochem. Soc. 145 (1998) 631-638.

81. Nowotny M., Sheppard L., Bak T., Nowotny J., "Defect chemistry of titanium dioxide. Application of defect engineering in processing of TiO-based photocatalysts," J. Phys. Chem. C, 112 (2008) 5275-5300.

82. Park C., Akbar S., "Ceramics for chemical sensing," J. Mater. Sci., 38 (2003) 4611-4637.

83. Pechini A., "Method of preparing lead and alkaline earth titanates and niobates and coating method using the same to form a capacitor," US patent #3,330,697 (1967).

84. Rahmstrof S., Casenave A., Church J., Hansen J., Keeling R., Parker D., Somerville R., "Recent climate observations compared to projections," Science 316 (2007) 709.

85. Ramis G., Busca G., Cristiani C., Lietti L., Forzatti P., Bregani F., “Characterization of tungsta-titania catalysts,” Langmuir 8 (1992) 1744-1749.

86. Rath C., Mohanty P., Pandey A., Mishra N., “Oxygen vacancy induced structural phase transformation in TiO2 nanoparticles,” J. Physics D: Appl Phys., 42 (2009) 205101-205107.

87. Raupach M., Marland G., Ciais P., Le Quere C., Canadell J., Klepper G., Field C., “Global and regional drivers of accelerating CO_2 emissions,” Proc. Nat. Acad. Sci., 104 (2007) 10288-10293.

88. Reidy D., Holmes J., Morris M., “The critical size mechanism for the anatase to rutile transformation in TiO2 and doped-TiO2,” J. Europ. Ceram. Soc. 26 (2006) 1527-1534.

89. Rothschild R., Komen Y., “The effect of grain size on the sensitivity of nanocrystalline metal-oxide gas sensors,” J. Appl Phys., 95 (2004) 6374-6380.

90. Ruiz A., Sakai G., Cornet A., Shimanoe K., Morante J., Yamazoe N., “Cr-doped TiO2 gas sensor for exhaust NO2 monitoring,” Sens. Act. B Chem., 93 (2003) 509-518.

91. Ruiz A., Dezanneau G., Arbiol J., Cornet A., Morante J., “Study of the influence of Nb content and sintering temperature on TiO2 sensing films,” Thin Solid Films 436 (2003) 90-94.

92. Ruiz A., Cornet A., Morante J., “Study of La and Cu influence on the growth inhibition and phase transformation of nano-TiO2 used for gas sensors,” Sens. Act. B Chem., 100 (2004) 256-260.

93. Ruiz A., Cornet A., Shimanoe K., Morante J., Yamazoe N., “Effects of various additives on the gas sensing performance of TiO2 nanocrystals obtained from hydrothermal treatments,” Sens. Act. B Chem., 108 (2005) 34-40.

94. Sadek A., Partridge J., McCulloch D., Li Y., Yu X., Wlodarski W., Kalantar-zadeh K., “Nanoporous TiO2 thin film based conductometric H2 sensor,” Thin Solid Films (2009) doi:10.1016/j.tsf.2009.02.151.

95. Sahm T., Gurlo A., Barsan N., Weimar U., “Basics of oxygen and SnO2 interaction; work function change and conductivity measurements,” Sens. Act. B Chem., 118 (2006) 78-83.

96. Savage N., Akbar S., Dutta P., “Titanium dioxide based high temperature carbon monoxide selective sensor,” Sens. Act. B Chem., 72 (2001) 239-248.

97. Savage N., Chwieroth B., Ginwalla A., Patton B., Akbar S., Dutta P., “Composite n-p semiconducting titanium dioxides as gas sensors,” Sens. Act. B Chem., 79 (2001) 17-27.

98. Sberveglieri G., Comini E., Faglia G., Atashbar M., Wlodarski W., “Titanium dioxide thin films prepared for alcohol microsensor applications,” Sens. Act. B Chem., 66 (2000) 139-141.

99. Sclafani A., Palmisano L., Schiavello M., “Influence of the preparation methods of TiO2 on the photocatalytic degredation of phenol in aqueous dispersion,” J. Phys. Chem., 94 (1990) 829-832.

100. Seeley Z., Choi Y., Bose S., “Citrate-nitrate synthesis of nano-structured titanium dioxide ceramics for gas sensors,” Sens Act. B Chem., 140 (2009) 98-103.

101. Seeley Z., Bandyopadhyay A., Bose S., Influence of crystallinity on CO gas sensing for TiO2 films,” Mater. Sci. Eng. B, 164 (2009) 38-43.

102. Seiyama T., Kato A., Fujiishi K., Nagatani M., “A new detector for gaseous components using semiconductor thin films,” Anal. Chem., 34 (1962) 1502.

103. Serrini P., Briois V., Horrillo M., Traverse A., Manes L., “Chemical composition and crystalline structure of SnO2 thin films used as gas sensors,” Thin Solid Films, 304 (1997) 113-122.

104. Sharma S., Singh D., Saini K., Kant C., Sharma V., Jain S., Sharma C., “Sol-gel super-hydrophilic nickel doped TiO2 films as active photo-catalyst,” Applied Catalysis A General 314 (2006) 40-46.

105. Siciliano T., Tepore A., Micocci G., Serra A., Manno D., Filippo E., “WO3 gas sensors prepared by thermal oxidation of tungsten,” Sens. Act. B Chem., 133 (2008) 321-326.

106. Stamataki M., Tsamakis D., Brilis N., Fasaki I., Giannoudakos A., Kompitsas M., “Hydrogen gas sensors based on PLD grown NiO thin film structures,” Phys. Stat. Sol. A 205 (2008) 2064-2068.

107. Stankova M., Vilanova X., Llobet E., Calderer J., Bittencourt C., Pireaux J., Correig X., “Influence of the annealing and operating temperatures on the gas sensing properties of rf sputtered WO3 thin-film sensors,” Sens. Act. B Chem., 105 (2005) 271-277.

108. Stetter J., “A surface chemical view of gas detection” J. Colloid Interface Sci., 65 (1978) 432-443.

109. Stojanovic B., Marinkovic Z., Brankovic G., Fidancevska E., “Evaluation of kinetic data for crystallization of TiO2 prepared by hydrolysis method,” J. Therm. Anal. Calorim. 60 (2000) 595-604.

110. Taguchi N., Japan Patent 45-38200 (1962).

111. Teleki A., Bjelobrk N., Pratsinis S., “Flame-made Nb- and Cu-doped TiO_2 sensors for CO and ethanol,” Sens. Act. B Chem., 130 (2008) 449-457.

112. Traversa E., Miyayama M., Yanagida," Gas sensitivity of ZnO/La2CuO4 heterocontacts," Sens. Act. B Chem., 17 (1994) 257-261.

113. Trimboli J., Mottern M., Verweij H., Dutta P., "Interaction of water with titania: implications for high-temperature gas sensing," J. Phys. Chem., 110 (2006) 5647-5654.

114. Trinchi A., Li Y., Wlodarski W., Kaciulis S., Pandolfi L., Viticoli S., Comini E., Sberveglieri G., "Investigation of sol-gel prepared CeO2-TiO2 thin films for oxygen gas sensing," Sens. Act. B Chem., 95 (2003) 145-150.

115. Vlachos D., Papadopoulos C., Avaritsiotis J., Dependence of sensitivity of SnOx thin-film gas sensors on vacancy defects," J. Appl Phys., 80 (1996) 6050-6054.

116. Wang X., Yee S., Carey W., "Transition between neck-controlled and grain-boundary-controlled sensitivity of metal-oxide gas sensors," Sens. Act. B Chem., 25 (1995) 454-457.

117. Wenbin X., Shurong D., Demiao W., Gaochao R., "Investigation of microstructure evolution in Pt-doped TiO2 thin films deposited by rf magnetron sputtering," Physica B, 403 (2008) 2698-2701.

118. Wisitoraat A., Tuantranont A., Comini E., Sberveglieri G., Wlodarski W., "Gas sensing properties of TiO_2-WO_3 and TiO_2-MO_3 based thin film prepared by ion-assisted E-beam evaporation," IEEE Sensors, 1184-1187 (2005).

119. Wisitsoraat A., Tuantranont A., Comini E., Sberveglieri G., Wlodarski W., "Characterization of n-type and p-type semiconductor gas sensors based on NiO_x doped TiO_2 thin films," Thin Solid Films 517 (2009) 2775-2780.

120. Xie H., Zhang Q., Xi T., Wang J., Liu Y., "Thermal analysis on nanosized TiO_2 prepared by hydrolysis," Thermochimica Acta 381 (2002) 45-48.

121. Xu C., Tamaki J., Miura N., Yamazoe N., "Grain size effects on gas sensitivity of porous SnO2-based elements," Sens. Actuators, B, Chem. 3 (1991) 147-155.

122. Yamada Y., Seno Y., Masuoka Y., Nakamura T., Yamashita, "NO2 sensing characteristics of Nb doped TiO2 thin films and their electronic properties," Sens. Act. B Chem., 66 (2000) 164-166.

123. Yamazoe N., "New approaches for improving semiconductor gas sensors," Sens. Act. B Chem., 5 (1991) 7-19.

124. Yamazoe N., "Towards innovations of gas sensor technology," Sens. Act. B Chem., 108 (2005) 2-14.

125. Yamazoe N., Fuchigami J., Kishikawa M., Seiyama T., "Interactions of tin oxide surface with O2, H2O AND H2," Surf. Sci., 86 (1979) 335.

126. Yang H., Zhang D., Wang L., “Synthesis and characterization of tungsten oxide-doped titania nanocrystallites,” Mater. Lett., 57 (2002) 674-678.

127. Yang J., Lai Y., Chen J., “Effect of heat treatment on the properties of non-stoichiometric p-type nickel oxide films deposited by reactive sputtering,” Thin Solid Films 488 (2005) 242-246.

128. Yoganarasimhan S., Rao C., “Mechanism of crystal structure transformations: Part 3. Factors affecting the anatase-rutile transformation,” Trans. Faraday Soc. 58 (1962) 1579-1586.

129. Zakrzewska K., Radecka M., Rekas M., Effect of Nb, Cr, Sn additions on gas sensing properties of TiO2 thin films,” Thin Solid Films 310 (1997) 161-166.

130. Zakrzewska K., “Gas sensing mechanism of TiO_2-based thin films,” Vacuum 74 (2004) 335-338.

131. Zhang D., Downing J., Knorr F., McHale J., “Room-temperature preparation of nanocrystalline TiO2 films and the influence of surface properties on dye-sensitized solar energy conversion,” J. Phys. Chem. B 110 (2006) 21890-21898.

132. Zhang H., Banfield J., “Kinetics of crystallization and crystal growth of nanocrystalline anatase in nanometer-sized amorphous titania,” Chem. Mater. 14 (2002) 4145-4154.

APPENDIX

APPENDIX A

Future Research

This work outlined a small portion of the potential research available using the techniques described. Provided continued interest and funding in this area, several other interesting studies are suggested:

1. **Optimization of sol concentration.** All sols used in the described research were 0.5 molar metal ion concentration. This concentration was chosen because we had previously found it to produce quality films of PZT on silicon wafers. It is entirely possible, however, that a higher concentration of metal ions in the sol would create thicker films in fewer layers, minimizing the possibility for film cracking to occur.
2. **Film porosity.** Films created here were not measured for porosity; however, in the micrograph images they appear to be relatively dense. High density films do not allow gas to penetrate, limiting the surface-gas reactions to the surface layer of the film. By creating porosity in the film, gas penetration would be possible, leading to surface reactions taking place throughout the entire film. One method to accomplish this would be templating porosity with a temporary polymer. I tried briefly to put a layer of polystyrene nanospheres on the substrate prior to spinning the film. This may have produced porosity, but it also cracked the film terribly. Optimization of the fabrication procedure is needed.
3. **Other dopants of interest.** In the present research, I have shown how influential a small concentration of dopant ions can be on the crystallinity and electronic properties of TiO_2. This is a very promising method to improve the sensing performance of a thin film. Other dopants that show similar size to titanium which could be interesting to study include Cr, Fe, Ga, Ir, Mn, Mo, Nb, Pt, Re, Ru, Ta, Tc, and V.
4. **Long term stability.** Evaluation of the long term stability (weeks and months) is still needed for thin film sensors operating at high temperatures.
5. **Composite p-n sensors.** Further investigation of sensors utilizing p-n junctions may be of interest. Sensor designs where current flows one direction across the junction may provide heightened sensitivity. This may be possible using MEMS fabrication techniques.